SU-SEL-69-061

Nonducted VLF Propagation In the Magnetosphere

by

Fernando Walter

October 1969

TECHNICAL REPORT NO. 3418-1

Prepared under
National Aeronautics and Space Administration
Contract NAS 5-3093 and Grant NsG-020-008
National Science Foundation, Office of Antarctic Programs
Grants NSF GA-1151 and GA-1485
Office of Naval Research
Contract ONR-N00014-67-A-0112, 0012

RADIOSCIENCE LABORATORY

STANFORD ELECTRONICS LABORATORIES

STANFORD UNIVERSITY · STANFORD, CALIFORNIA

SU-SEL-69-061

NONDUCTED VLF PROPAGATION IN THE MAGNETOSPHERE

by

Fernando Walter

October 1969

Technical Report No. 3418-1

Prepared under
National Aeronautics and Space Administration
Contract NAS 5-3093 and Grant NsG-020-008
National Science Foundation, Office of Antarctic Programs
Grants NSF GA-1151 and GA-1485
Office of Naval Research
Contract ONR-N00014-67-A-0112,0012

Radioscience Laboratory
Stanford University Stanford, California

ABSTRACT

Evidence for nonducted VLF propagation between conjugate hemispheres has been found in records from the broadband VLF receivers aboard the polar satellites OGO 2 (419-1521 km) and OGO 4 (412-908 km). The nonducted signals described here are received in the ionosphere between 47° and 56° invariant latitude. They have never been observed on the ground and include natural whistlers and fixed-frequency signals (10.2-12.5 kHz) from the U. S. Navy Omega transmitters. In a frequency-time spectrogram, these nonducted whistlers appear as rising tones with a lower cutoff frequency in the approximate range of 5 to 8 kHz. They have been named "walking trace" (WT) whistlers, since a rapid increase in travel time as a function of satellite latitude causes successive examples of the rising trace to "walk through" other whistlers having equal dispersions and produced by the same sequence of lightning sources. A train of WT whistlers exhibits a nearly constant lower cutoff frequency which is equal to the maximum value of the lower hybrid resonance (LHR) frequency above the satellite, and an upper cutoff frequency that decreases with increasing satellite latitude. Reflected waves following a WT whistler can also be received if the LHR frequency below the satellite reaches values greater than those above it. Observed spectral shapes of such whistlers resemble a fish hook. Fixed-frequency Omega signals observed by OGO 4 in the hemisphere conjugate to the transmitter frequently have characteristics similar to those of the WT whistlers. The Omega signals exhibit two features that are not apparent in the natural whistlers: an enhancement of signal strength and a Doppler shift that increases with latitude and may reach hundreds of Hertz.

The main characteristics of the above phenomena are explained by tracing nonducted rays between conjugate hemispheres in a model magnetosphere. An equatorial electron density profile is derived from the WT whistlers.

TABLE OF CONTENTS

TABLE OF CONTENTS (cont.)

TABLE OF CONTENTS (cont.)

LIST OF TABLES

LIST OF FIGURES

LIST OF FIGURES (cont.)

LIST OF FIGURES (cont.)

ACKNOWLEDGMENTS

The author wishes to thank Professor R. A. Helliwell, Dr. R. L. Smith, and Dr. J. J. Angerami for enlightening discussions and for their patience and guidance; Mr. J. Katsufrakis for calling attention to interesting data; and Dr. D. L. Carpenter for helpful criticism of Chapters 2 and 3.

The research was supported in part by the National Aeronautics and Space Administration under contract NAS 5-3093 and grant NsG-020-008; in part by the National Science Foundation, Office of Antarctic Programs under grants NSF GA-1151 and GA-1485; in part by the National Science Foundation, Office of Computer Sciences under grant NSF GP-948, and in part by the Office of Naval Research under contract ONR-N00014-67-A-0112, 0012. The research was carried out under a graduate student research assistantship awarded by Stanford University and a scholarship awarded by C.N.A.E. - Brazil.

I. INTRODUCTION

A. BACKGROUND OF THE PROBLEM

A lightning flash produces very low frequency (VLF) waves that may propagate through the magnetosphere. When received on the ground or by a spacecraft in the magnetosphere, these waves show a dispersive characteristic, resulting in a sound like a whistle heard when the signals are reproduced by means of an audio amplifier. For this reason they have been called "whistlers" (see Helliwell [1965] for more details). In order to explain the properties of whistlers observed on the ground, Smith [1960] developed a theory of trapping of whistler energy along a tube of force by an enhancement of ionization. These ducted whistlers have been used to study properties of the electron distribution in the magnetosphere (see Helliwell [1965]).

VLF receivers on satellites have revealed a complete new class of whistler phenomena. A cross section of the magnetosphere containing a geomagnetic meridian is shown in Figure 1. The positions of four receivers, one on the ground and three in the magnetosphere, are indicated by the symbols R_1, R_2, R_3 and R_4. Waves produced by a lightning flash can only reach R_2, R_3 and R_4 through the magnetosphere. The receiver on the ground, R_1, may receive signals propagating through the magnetosphere and also through the earth-ionosphere wave guide.

A lightning flash may produce a frequency versus time record such as the one sketched in Figure 2a, when received by R_1. The whistler indicated by an 0 is the one reaching R_1 through the earth-ionosphere wave guide. This component shows almost no dispersion. However, the component propgating through the magnetosphere, indicated by 1, presents time delays

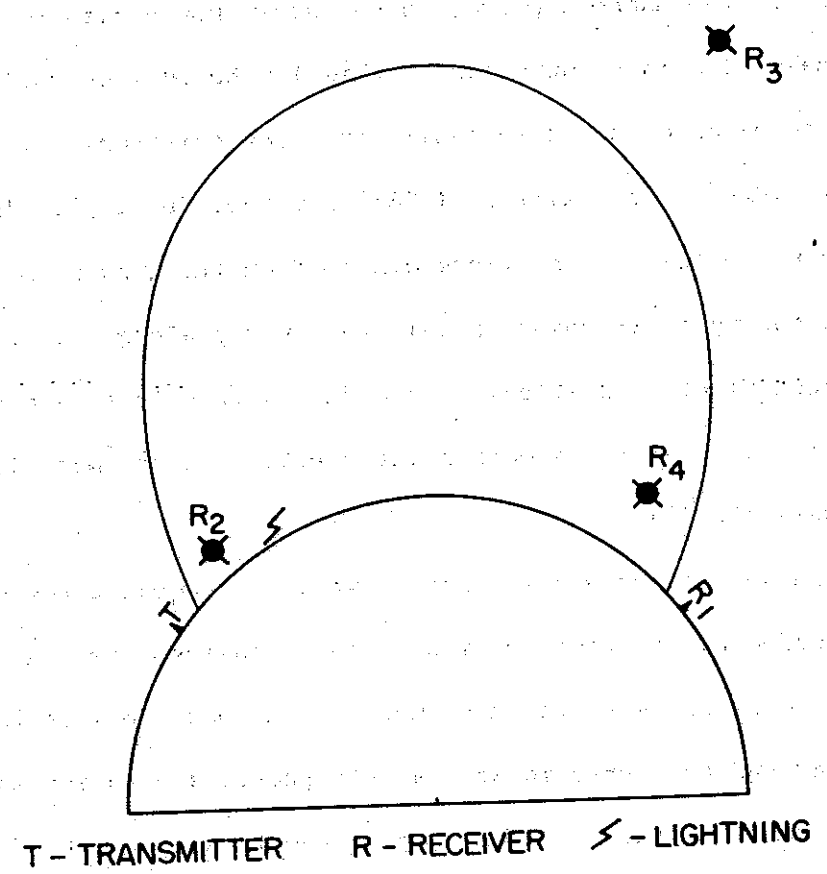

Figure 1. Cross section containing a geomagnetic meridian plane, a VLF transmitter (T) and a lightning flash (⚡) are shown. A ground VLF receiver is indicated by R_1. Two receivers, R_2 and R_4, are located in polar, low altitude satellites. A receiver in a high altitude satellite is represented by R_3. For reference the thin line shows the line of force at $L = 2.5$.

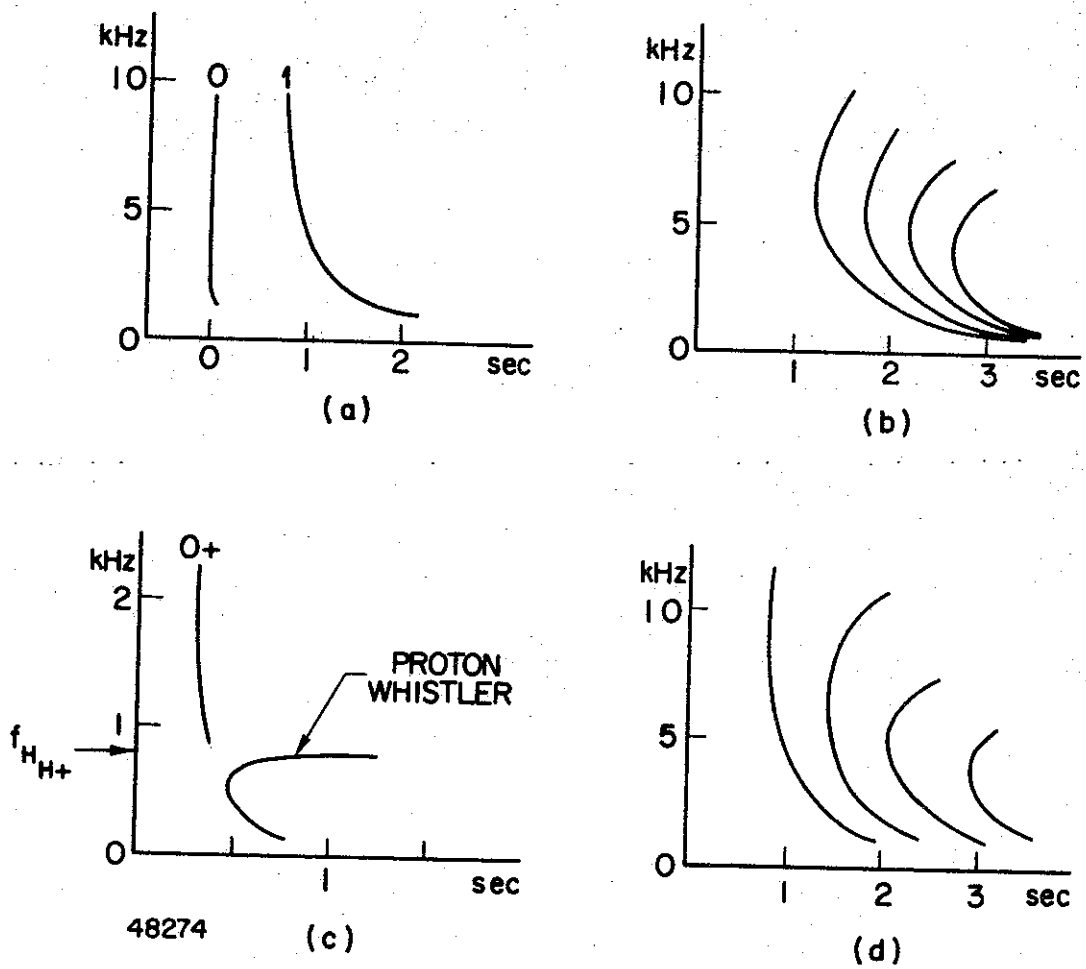

Figure 2. Frequency versus time spectrograms: (a) and (b) are sketches of spectrograms received by ground stations; (c) is a typical spectrogram of a proton whistler received by R_2; (d) shows one type of whistler received by R_3.

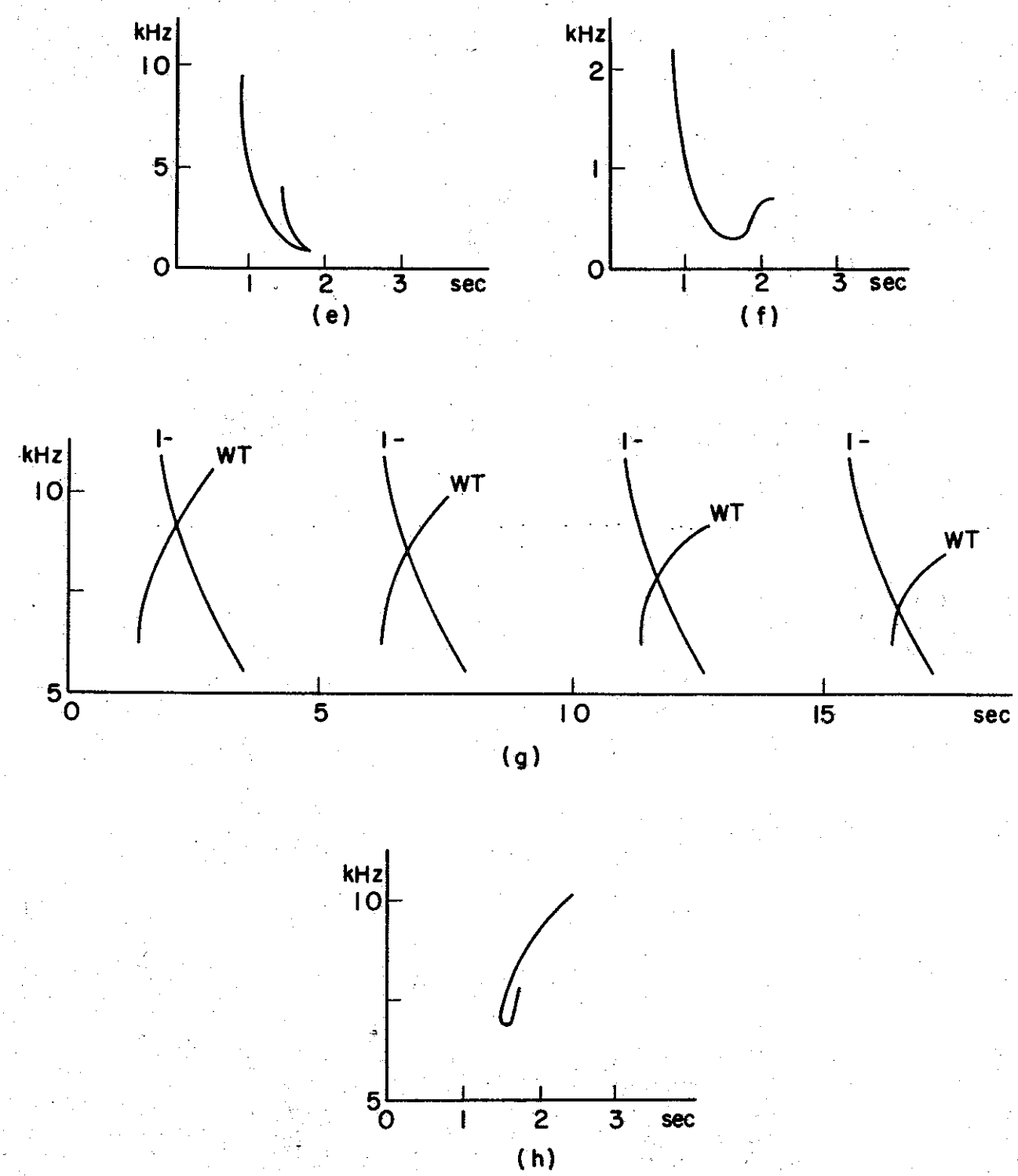

Figure 2. Frequency versus time spectrograms: (e) shows one type of whistler received by R_3; (f), (g) and (h) show types of whistlers recorded by R_4.

that are a function of frequency. Sometimes trains of whistlers are seen, with components presenting 'nose' characteristics (see Helliwell [1965]). This case is illustrated in Figure 2b.

Whistlers received by R_2 may produce a spectrogram as shown in Figure 2c. The component indicated by 0^+ reaches the satellite through propagation in the so-called electron whistler mode and the other in the proton whistler mode [Gurnett et al., 1965]. The proton whistlers show an asymptotic behavior at the proton gyrofrequency at the satellite. They are not observed on ground records and to understand their behavior it is necessary to consider the movement of protons in the derivation of the phase refractive index.

Another kind of whistler that is observed by a receiver at R_3 and named magnetospherically reflected (MR) whistler [Smith and Angerami, 1968] is illustrated in Figure 2d. The waves that produce these whistlers are reflected in the magnetosphere and move back and forth across the magnetic equator. Another kind of whistler that may be observed by R_3, is shown in Figure 2e. This is the Nu whistler, which is also a consequence of reflection in the magnetosphere [Smith and Angerami, 1968]. As in the case of proton whistlers, these whistlers are not observed on ground records.

Several different kinds of whistlers may be received at R_4. One of these is the ion-cutoff whistler, sketched in Figure 2f [Muzzio, 1968]. The double valued trace presented by these whistlers results from reflection of downcoming waves in the ionosphere. Another whistler that may be received by R_4 is the one indicated by 1_- in the sketch of Figure 2g. This whistler propagates in a nonducted mode and is the result of the presence of large horizontal gradients in the ionosphere [Scarabucci et al., 1969].

Another whistler that may be observed is indicated by the letters WT in Figure 2g. It has the characteristic of a rising tone, and also has not been observed on ground records. Generally in a spectrogram a sequence of these whistlers is observed displaying a constant lower cutoff and an upper-cutoff frequency that decreases with the latitude of the receiver. The increase of travel time for a given frequency when the receiver is moving toward higher latitudes makes them appear to walk through the 1_- component, and for this reason have been named "walking trace" (WT) whistlers. These are the whistlers that will be explained in this report. The understanding of these whistlers led to an explanation of certain other VLF phenomena. For example, in special circumstances WT whistlers are followed immediately by a trace that has been interpreted as caused by refraction in the ionosphere. These whistlers have the appearance of a fish hook and are illustrated in Figure 2h.

The U. S. Navy has transmitters at fixed frequencies in the range of WT whistlers, and it is expected that the associated signals may propagate in the same mode as the WT whistlers. Fixed-frequency signals received by a satellite in the hemisphere conjugate to the transmitter not only exhibit the main characteristics of WT whistlers, but also show two new effects not observable in the WT whistlers, a focusing effect and large Doppler shifts in frequency.

B. OBJECTIVE OF THIS WORK

One of the purposes of the present work is to describe and interpret WT whistler phenomena identified in midlatitude ($\sim 50^{\circ}$) spectrographic records from the VLF experiment aboard the low-altitude polar satellites OGO 2 (419-1521 km) and OGO 4 (412-908 km).

The WT whistlers and their counterparts in manmade VLF signals present a remarkable variety of effects, including limited latitude range of observation, rapid variation in travel time with position, upper and lower intensity cutoffs, focusing, and Doppler shifts. Ray tracing analysis has been successful in predicting nearly all of the observed effects.

Another purpose of this work is to describe the ray equations in a more simple way than the ones found in the literature. A description of a digital ray-tracing program is also given.

C. RAY-TRACING TECHNIQUE

Ray-tracing has been used successfully to explain new whistler phenomenon observed on records from satellites. Historically the first whistler ray paths in a smooth magnetosphere were graphically calculated by Maeda and Kimura [1956]. This study was made to explain ground observed whistlers. For the refractive index they used the quasi-longitudinal (Q.L.) approximation (see for instance Stix [1962] or Helliwell [1965]) and they considered a magnetosphere constituted of electrons only. Haselgrove [1954] derived a set of first order differential equations based on Fermat's principle suitable to be solved with the aid of a digital computer. Haselgrove [1957] presented calculations of ray paths using her two-dimensional cartesian ray tracing equations. In these calculations three assumptions were made. The quasi-longitudinal approximation for the whistler refractive index was used, the movement of positive ions was neglected, and a horizontally stratified magnetosphere was assumed.

Whistler ray path calculations which used the exact expression for the refractive index and a digital computer were published

by Yabroff [1961]. The hypothesis of a magnetosphere composed of electrons only was again assumed in this work. Yabroff also studied the problem of ducting of whistlers by columns of enhanced ionization along the field line.

Hines [1957] has shown that for VLF it is possible to have transverse propagation and to have rays refracted back toward the earth at low latitudes when the movement of positive ions is allowed for. Hines, Hoffman and Weil [1959] did ray tracing including protons for the special case of transpolar propagation. Kimura [1966] published the first ray-tracing results that included effects of three major ions in the magnetosphere H^+, He^+, and O^+. Shawhan [1966] wrote a two-dimensional ray-tracing program of which the main purpose was to explain some whistler phenomena observed in Injun satellites. Smith and Angerami [1968] showed qualitatively that some of the ray paths calculated by Kimura could be used to explain anomalous nose whistlers observed near the equatorial region at high altitude in the data from OGO-1. These whistlers are called 'magnetospherically reflected' (MR) whistlers.

D. PLAN OF THIS RESEARCH

The walking trace whistler is described and explained in Chapter 2. Doppler shifts and focusing effects in fixed-frequency signals are analyzed and explained in Chapter 3. Development of the ray equations for a two dimensional geometry is given in Chapter 4. Also in this chapter a digital ray-tracing program is described, and physical interpretations of typical ray paths are given. The summary and conclusions of the results of this work are presented in Chapter 5.

The listing of the ray-tracing program constitutes Appendix A. An

example of input cards for this program is given in Appendix B, with a listing of a typical output shown in Appendix C. In Appendix D the equations derived in Chapter 4 are shown to be equivalent to the Haselgrove [1954] equations. The differential equation governing the variation with the phase time of the angle between the wave normal and the geomagnetic field is derived in Appendix E. Finally, in Appendix F, the differential Snell's law is derived.

E. CONTRIBUTIONS

New whistler phenomena, the walking trace whistler and focusing effects and Doppler shifts in manmade signals are described and explained using a ray-tracing technique. The two-dimensional ray equation is obtained in a simple way. It is shown that the differential Snell's law applied by Haselgrove [1954] is only valid for a medium with parallel stratification. A new way to write a two-dimensional ray-tracing program is presented based on three not four differential equations.

II. THE WALKING TRACE WHISTLER

A. INTRODUCTION

Satellite studies have revealed a remarkable variety of "nonducted" whistler phenomena, that is, whistlers whose paths are not confined to field-aligned irregularities in the magnetosphere. Particular types of nonducted whistlers are often observed in relatively limited regions of space and may exhibit unusual dispersion properties that vary rapidly with observing position. Such effects invite attempts at analysis by ray tracing. For example the magnetospherically reflected (MR) whistler has been explained qualitatively by Smith and Angerami [1968], based on Kimura's ray tracing results [1966].

The purpose of this report is to describe and interpret a new whistler phenomenon identified in mid-latitude ($\sim 50^{\circ}$) spectrographic records from the VLF experiment aboard the low-altitude polar satellites OGO 2 (419-1521 km) and OGO 4 (412-908 km). These whistlers, first called to our attention by John Katsufrakis of our laboratory, have been named "walking-trace" (WT) whistlers, for reasons explained below. In contrast to the MR whistler, whose path reaches the equatorial region and then oscillates back and forth across the equator, the WT whistler crosses the equator and then continues downward into the conjugate ionosphere. The WT whistler and its counterpart in manmade VLF signals presents a remarkable variety of effects, including limited latitude range of observation, rapid variation in travel time with position, upper and lower intensity cutoffs, focusing, and Doppler shifts. Ray-tracing analysis, applied for the first time to a complex nonducted whistler propagating between conjugate ionospheres, has been successful in predicting

nearly all of the observed effects. (Several of the effects were only recognized as part of the WT phenomenon after ray tracings were made.)

The next section contains a brief description of the observations. Following this is a description of the ray-tracing analysis and a discussion of the physical factors influencing the various WT whistler properties. Later sections are devoted to details of the observations.

B. DESCRIPTION OF THE WT WHISTLER

On frequency-time records from satellites, WT whistlers appear as rising tones whose travel time increases rapidly with increasing satellite latitude. The main features of the WT whistler are illustrated on an OGO-4 record in Figure 3a. Frequency in kHz is displayed versus UT and invariant latitude on a northbound pass over Rosman, North Carolina. Heavy arrows identify four WT whistlers. Typical features are the relatively constant lower cutoff frequency and an upper cutoff frequency that decreases with increasing satellite latitude. The second event is shown with an expanded time scale in Figure 4.

For each of the WT whistlers identified by a heavy arrow in Figure 3a, a vertical arrow in the lower margin identifies a corresponding nearly impulsive whistler. It propagates on the short, so-called 'fractional hop' or 0_+ path up through the nearby ionosphere to the satellite. A horizontal bar and asterisk in the upper margin identify still a third whistler component produced by the same lightning source. This whistler propagates on a long, so-called one-hop or 1_- path between conjugate hemispheres. Although nonducted, its path is topologically different from that of the WT whistler because the wave normals are small, as a result of horizontal gradients in the ionosphere [Scarabucci et al., 1969]. Within a measurement uncertainty of less than 20 msec, the dispersion of

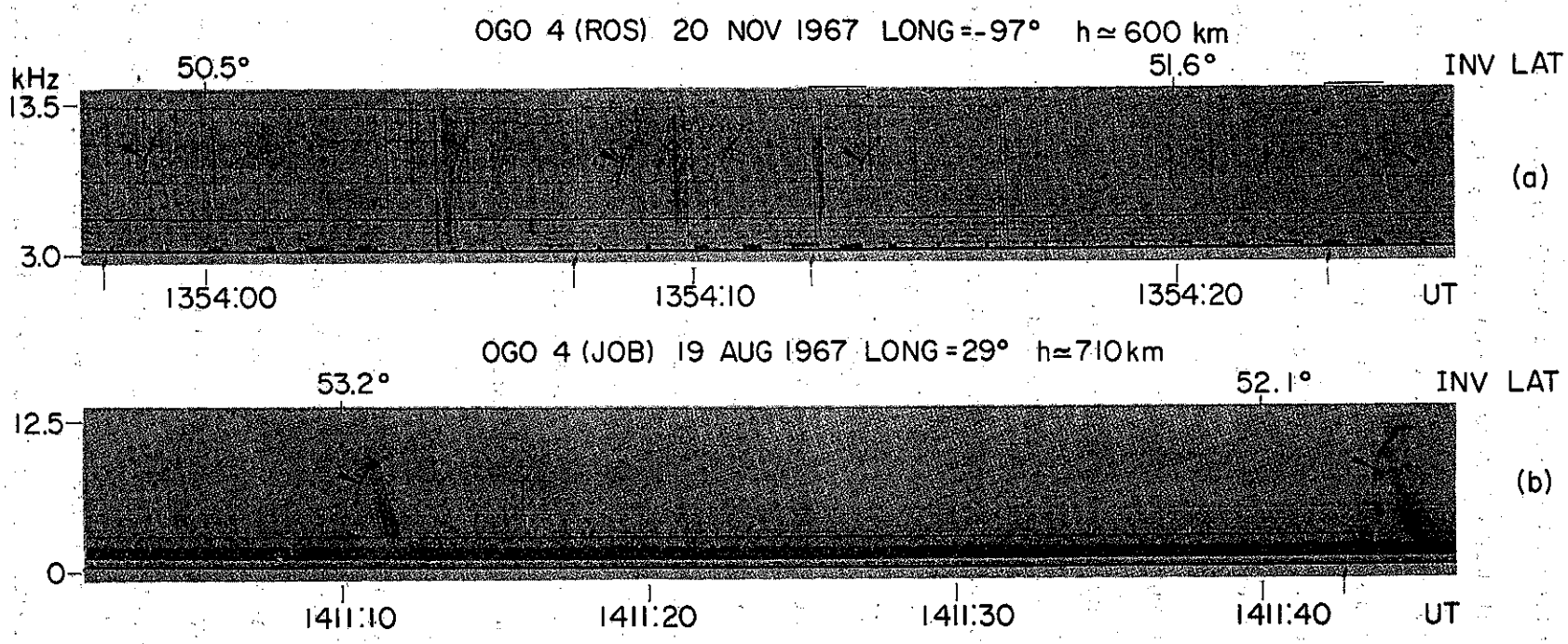

Figure 3. OGO-4 records of frequency versus time and invariant latitude illustrating several features of WT whistlers. In (a) four independent events are labeled, each consisting of three related components: 1) the impulsive signal propagating upward through the nearby ionosphere, (vertical arrow at bottom); 2) a falling tone whistler (asterisk); and 3) the WT whistler (heavy arrow). In (b) multicomponent falling tone whistlers are associated with the WT components indicated by heavy arrows. Fixed-frequency signals at 10.2 and 11-1/3 kHz from an Omega transmitter in the conjugate region (Aldra, Norway) appear after 1411:20 as the latitude decreases. These signals are interpreted as following the ray path of the WT whistlers. The measured travel time of the last Omega signal was used to locate the time of origin of the last whistler event (vertical arrow at bottom). A band of hiss appears below 1.7 kHz. The horizontal lines are interference at multiples of 2461 Hz.

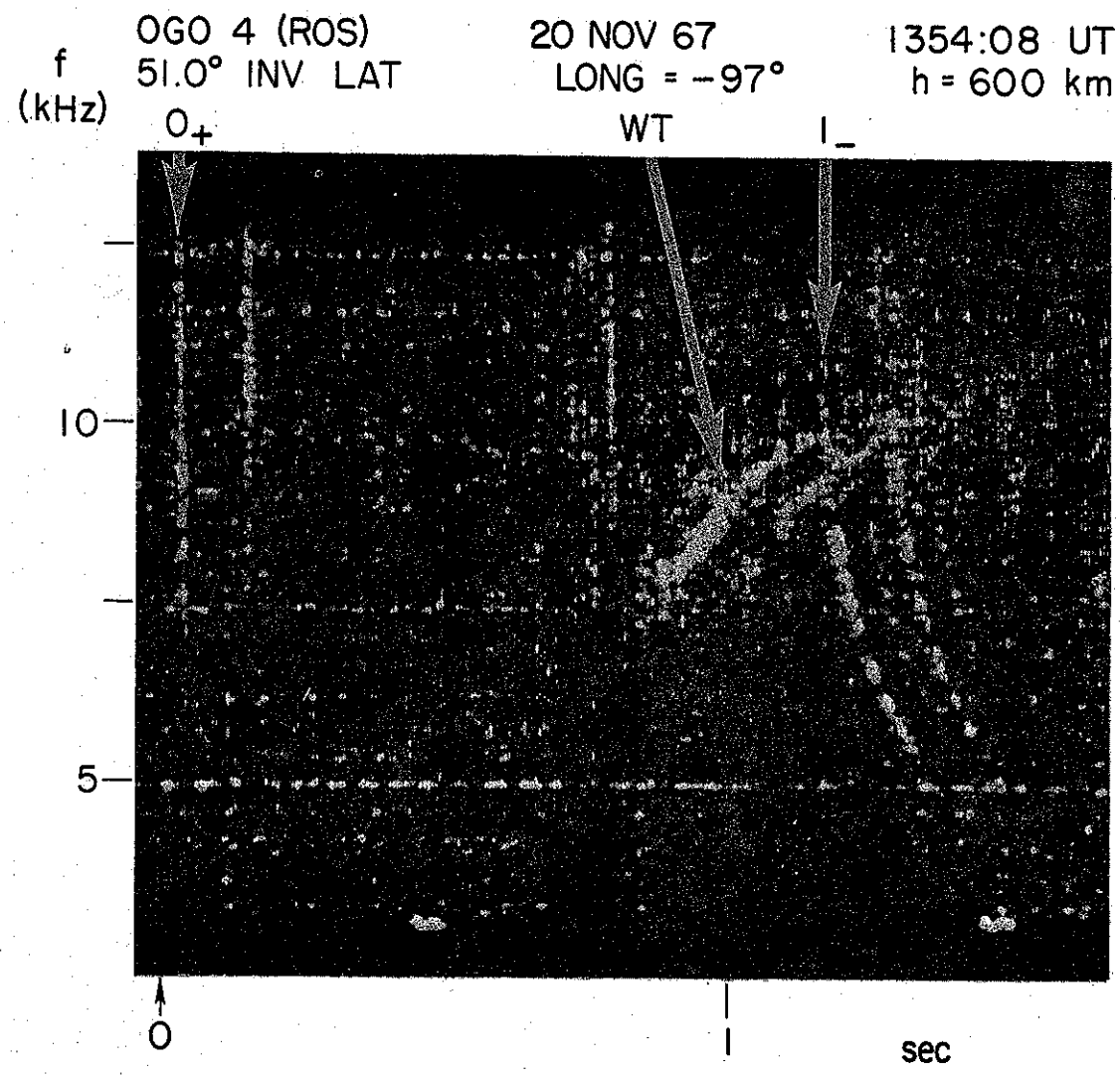

Figure 4. An expanded frequency-time spectrogram of the second WT whistler event shown in Figure 3a. There are actually two independent events spaced by ~ 0.1 sec. The time origin indicates the time of occurrence of the lightning discharge that produced the indicated whistler components and the horizontal lines are interference at multiples of 2461 Hz.

the 1_- whistlers* does not change throughout the record, whereas the travel time of the WT events increases significantly during the same interval of time ($\approx$ 30 sec). This is evidenced by the fact that the WT and the 1_- whistler cross at a point that moves to lower frequencies with increasing latitude. Hence it appears that the WT "walks through" the 1_- whistler, giving rise to the name "walking-trace" (WT) whistler.

The mode of propagation of the waves producing the WT whistlers will be referred to as the "Pro-Resonance" (PR) mode. An explanation as to the choice of the name PR mode will be given in Chapter 4, Section E.

When ray tracings were developed to analyze whistlers of the type shown in Figures 3 and 4, the analysis indicated that fixed-frequency signals propagating in the PR mode should exhibit both focusing and Doppler shift effects. Such effects were found in the data, and now may be understood as a natural part of the WT phenomenon.

Examples of focusing and Doppler shifts appear in receptions by OGO 4 of fixed-frequency signals from the U.S. Navy Omega navigation stations. These signals may exhibit anomalously large intensities and also Doppler shifts that reach hundreds of Hertz. A typical example is illustrated in the frequency-time spectrogram of Figure 5, recorded by OGO 4 near Johannesburg, South Africa. A pulse at 11-1/3 kHz transmitted by the Omega station at Aldra, Norway (66°25'N, 13°09'E) is represented in the upper margin of the record by a line with duration 1.1 sec starting at $t = 0$. This pulse is received twice by the satellite. The first signal begins at 11-1/3 kHz in the center of the record, near $t = 0.6$ sec. (This signal and the 1_- whistlers of Figure 3a are believed to follow analogous paths, differing topologically from those of the PR mode.) A

*In this context the term "1_- whistler" refers only to the falling-tone whistler usually associated with the WT whistler.

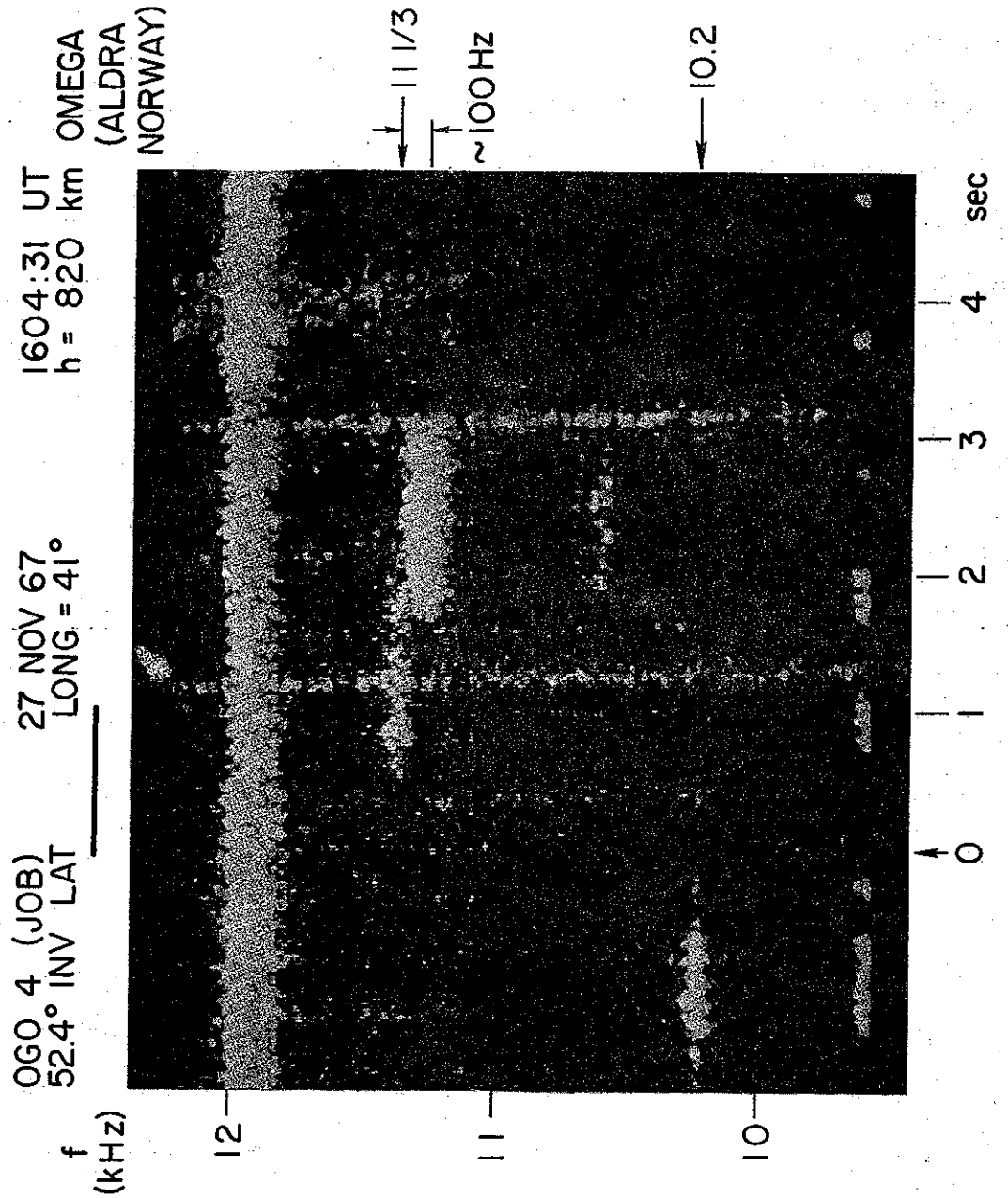

Figure 5. OGO-4 frequency-time spectrogram illustrating an ~ 100 Hz Doppler shift in nonducted fixed-frequency signals from an Omega transmitter in the conjugate region (Aldra, Norway). A transmitted pulse at 11-1/3 kHz is represented above the record by a dash beginning at $t = 0$. This pulse is received twice by the satellite. The first signal, presenting no Doppler effect, appears at 11-1/3 kHz, $t \sim 0.6$ sec. The second is shown by a strong dash at $t \sim 1.8$ sec, with a negative Doppler shift of about 100 Hz. The strong continuous signal near 11.9 kHz is a transmission from an unidentified VLF station. The nearly vertical lines are whistlers. Dots at the bottom of the record are time marks generated at the telemetry station. An Omega signal at 10.2 kHz appears near the left margin.

second, stronger pulse appears just below and to the right, starting at $t = 1.8$ sec. This signal exhibits a negative Doppler shift of about 100 Hz, and is interpreted as propagating to the satellite in the same kind of nonducted mode as the WT whistlers of Figures 3 and 4. (An Omega signal at 10.2 kHz appears near the left margin of the record. Signals in the PR mode at this frequency are not seen here, but were observed at higher latitudes--see Figure 14.) A later section presents some relatively complex examples of the data, including simultaneous occurrence in the PR mode of whistlers and fixed-frequency signals.

C. RAY-TRACING INTERPRETATION OF THE WT WHISTLER

Whistlers with the characteristics described above were reproduced by tracing nonducted ray paths from one hemisphere to the conjugate region. Ray tracings in a cold plasma, with the effects of ions included, were made with a FORTRAN IV program described in Chapter 4, Section D. The program is based on the differential equations developed in Chapter 4, Section B. The model magnetosphere was represented by a dipole magnetic field and isothermal diffusive-equilibrium distribution [Angerami and Thomas, 1964] of electrons and ions along the field lines at 3000 ^{o}K. An ion population of 90% O^+ and 10% H^+ was assumed at 1000 km. The model of the variation of electron density at 1) 1000 km as a function of latitude and at 2) the equator as a function of L value is shown in Figure 6 by the heavy lines. The thin lines, shown for comparison, correspond to a constant density model at 1000 km. (The ray tracing analysis described below predicts that certain features of the PR mode are highly sensitive to the indicated type of change in model.)

Figure 7a illustrates nonducted ray paths for waves at 10 kHz starting

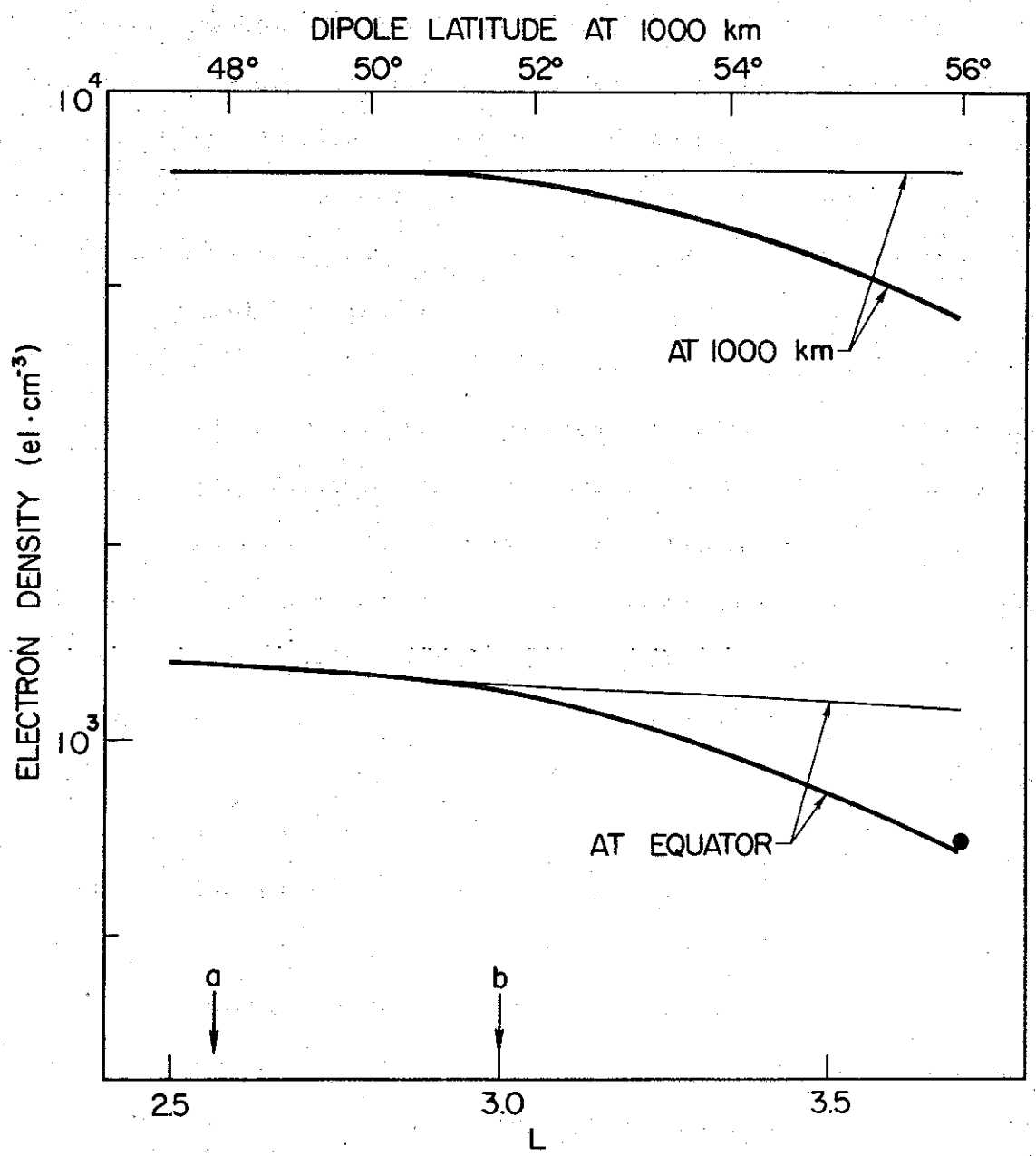

Figure 6. Models of the electron density variation at 1000 km as a function of dipole latitude (top) and at the equator as a function of L values (bottom). The heavy lines represent the basic model used in this paper, the thin lines a constant density model used for comparison. The portion between points a and b indicates the range of equatorial L values crossed by the rays that produced the WT whistlers shown in Figure 12. A dot shows the equatorial electron density measured using a nose whistler observed on OGO 4 a few minutes after the events shown in Figure 3a were recorded.

in the northern hemisphere at two different invariant latitudes (44.3° and 49.9°) with vertical wave normals at an altitude of 500 km. A dipole field line at $L = 4$ is shown for reference. Cumulative travel time along the paths (in sec) is indicated at the series of dots. The direction of the wave normal is indicated by arrows at several points, and at the arrows the value of the refractive index μ is marked. Thus the path beginning with vertical wave normal at A' has an initial μ of 15. To clarify Figure 7a, Figure 7b shows the single ray path A' - A and also the dipole field line of maximum L value along the path (dashed curve). Figure 7c presents five refractive index diagrams (not to scale) to illustrate wave normal and ray direction at the points (1) through (5) of Figure 7b. At point (1), the wave normal is vertical, and the ray, whose direction is normal to the refractive index surface, points outward toward higher L values. The wave normal is initially pulled away from the vertical toward $\vec{B}_o$ by the effect of the horizontal gradient in the magnetic field. The vertical gradient of electron density then becomes a controlling factor, causing further tilting of the wave normal toward $\vec{B}_o$. At some point (2) ψ reaches a minimum, beyond which it increases under the influence of the curvature of the magnetic field, Meanwhile, the ray continues to point outward, but at progressively smaller angles until it is oriented parallel to the magnetic field (3). This is the point of L_{max}, since from here on the ray direction is inward with respect to $\vec{B}_o$.

Between (3) and (4) ψ continues to increase under the influence of the curvature and the radial gradient of the magnetic field. The value of μ now increases rapidly, as shown by the increase from $\mu = 30$ to $\mu = 40$ on path A' - A in Figure 7a. At point (4), ψ is close to the

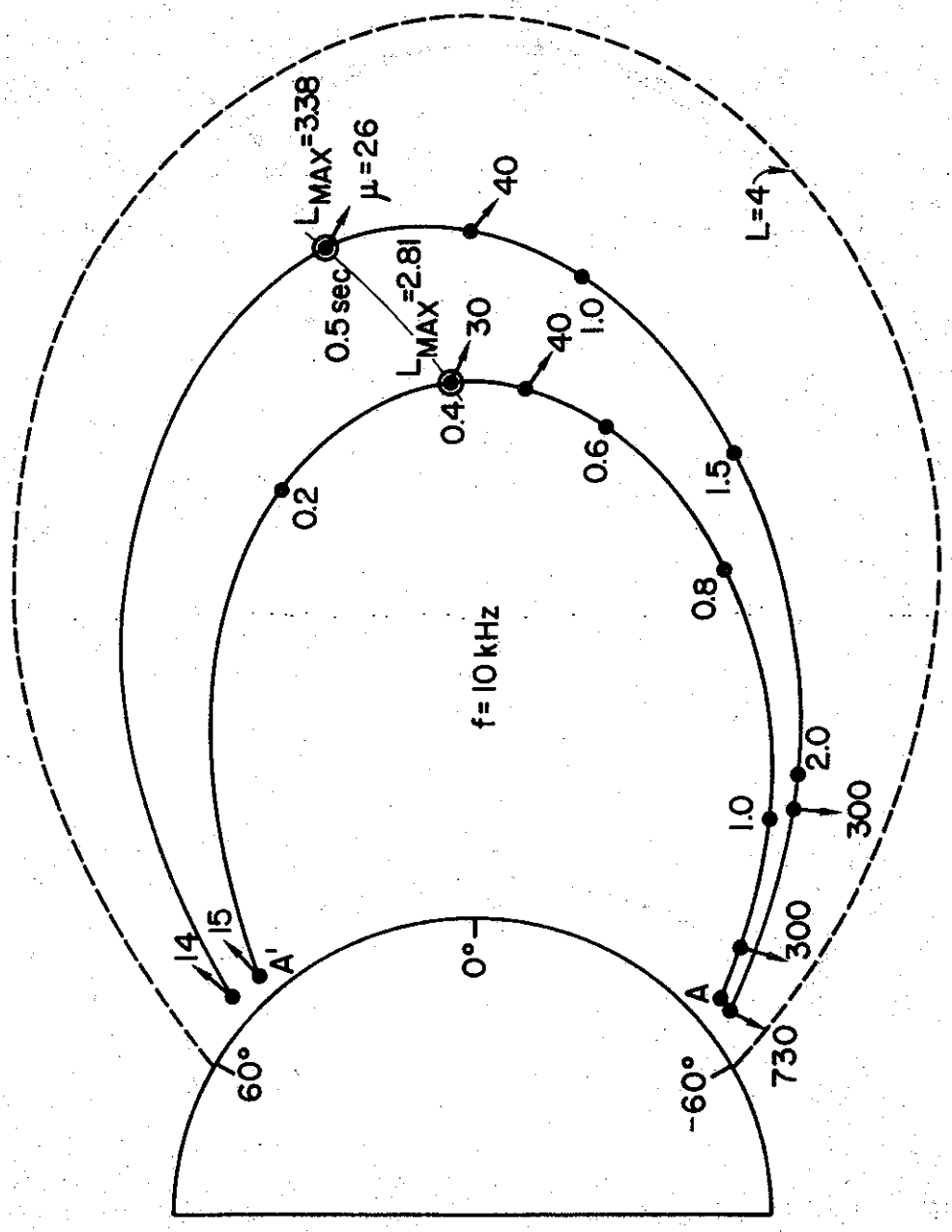

Figure 7a. Ray paths calculated for wave packets at 10 kHz starting with vertical wave normals at 500 km and invariant latitudes of 44.3° (point A') and 49.9°. A dipole field line at $L = 4$ is shown for reference. Arrows indicate the wave normal directions, and the accompanying values of the phase refractive index μ are indicated. Travel times calculated from the starting points at 500 km are indicated at several points along the rays. The thin line shows the locus of L_{max}.

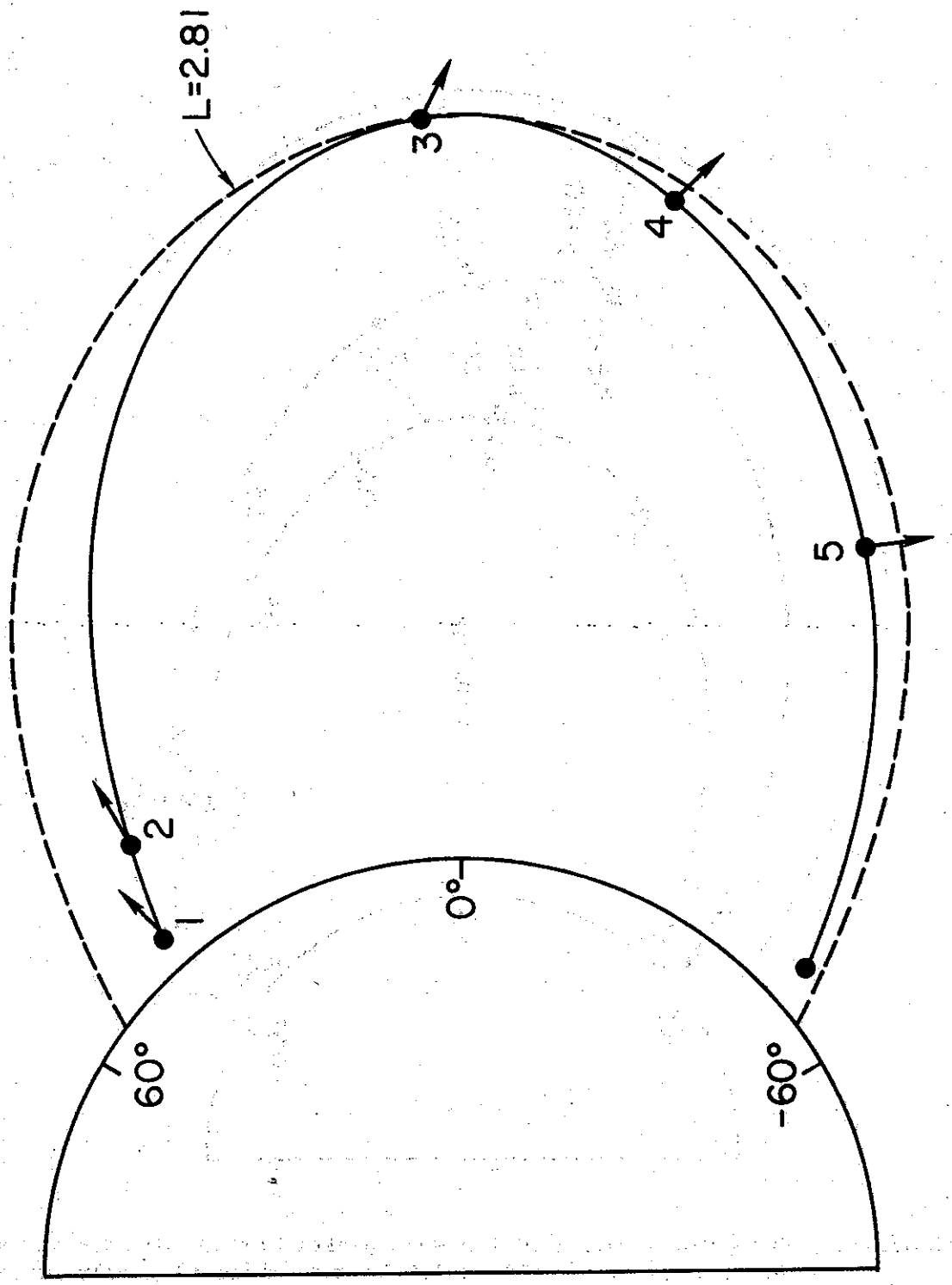

Figure 7b. Sketch of the inner ray path from Figure 7a, showing the dipole field line through maximum L along the path.

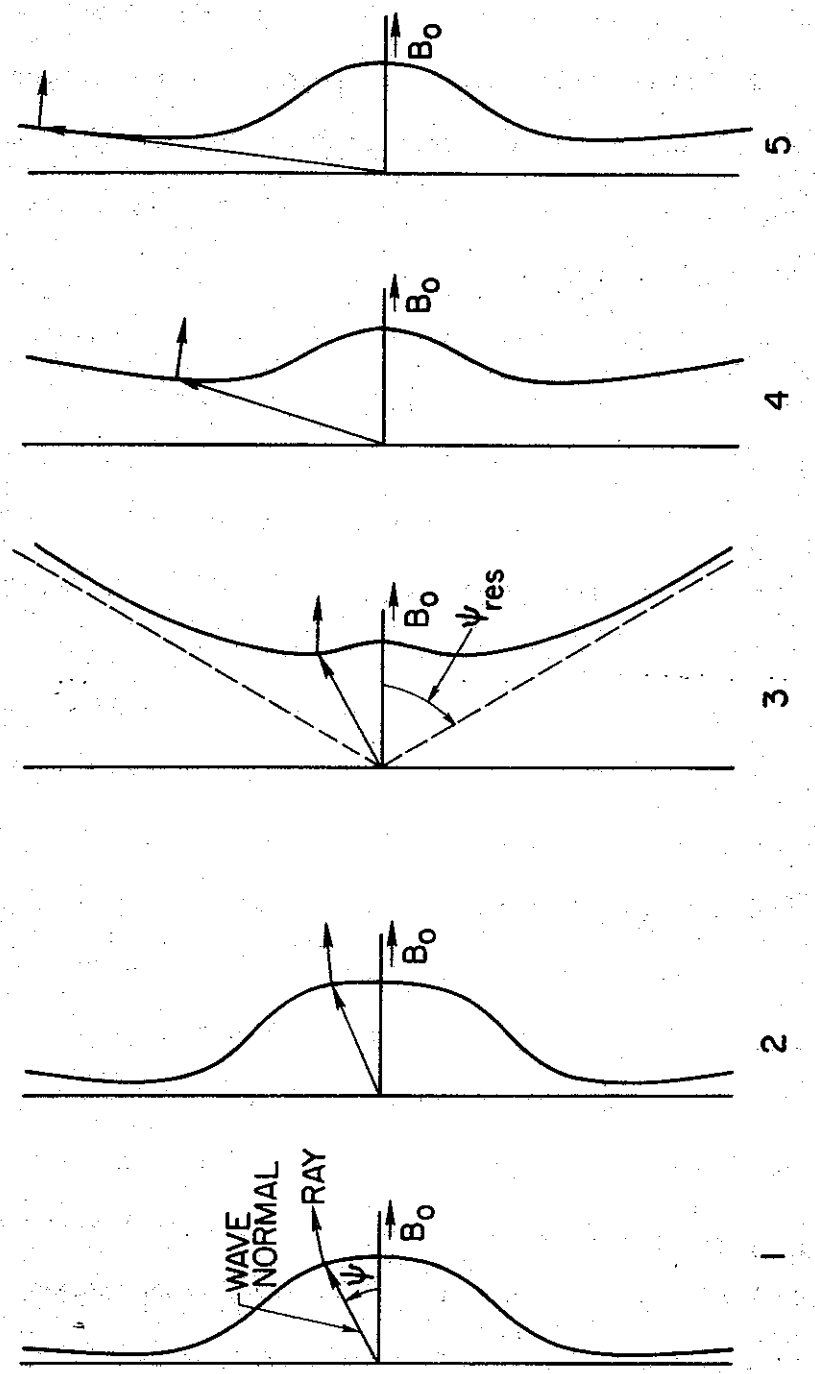

Figure 7c. Five refractive index diagrams (not to scale) indicating the wave normal and ray direction at four representative points along the ray path of Figure 7b.

resonance angle ψ_{res}, and the ray path is strongly dependent on the configuration of the magnetic field. At point (5), the resonance angle and the associated angle ψ have increased until the ray is approximately parallel to $\vec{B}_o$. Hence the ray follows closely a geomagnetic field line for the last several thousand km.

A different interpretation for the ray path is given in Chapter 4, Section E, where the equation that governs the variation of ψ along the path is used.

Another view of the ray tracing results is shown in Figure 8a where travel time through the magnetosphere to a satellite at 600 km is plotted as a function of the invariant latitude of the arrival point, with the wave frequency used as a parameter. (The thin line represents the constant-density-at-1000-km model of Figure 6.) The coordinates of the point B, for instance, are the time of propagation from A' to A (cf. Figure 7a) and the invariant latitude of point A. The dashed lines in Figure 8a indicate the outermost L-shell reached by each ray (for point B, L_{max} = 2.81). Figure 8b shows a corresponding plot of input latitude versus observing latitude. (Wave normals are assumed vertical at the input.) Point B, corresponding to path A' - A of Figure 7a, represents θ_{IN} = 44.31°, $\theta_{OBSERVED} = 50.78^{\circ}$. The input latitudes in Figures 8a and 8b were limited to 56°. (The behavior of rays starting above $\sim 51^{\circ}$ is very sensitive to details of the horizontal gradients in the ionosphere and is under investigation.)

Figures 8a and 8b may be used to predict a number of features of the PR mode. At a fixed satellite latitude, for example, travel time increases with frequency in the general manner illustrated by the data of Figure 3. For an observer at 51°, the calculated travel time at 8 kHz is ~ 0.8 sec

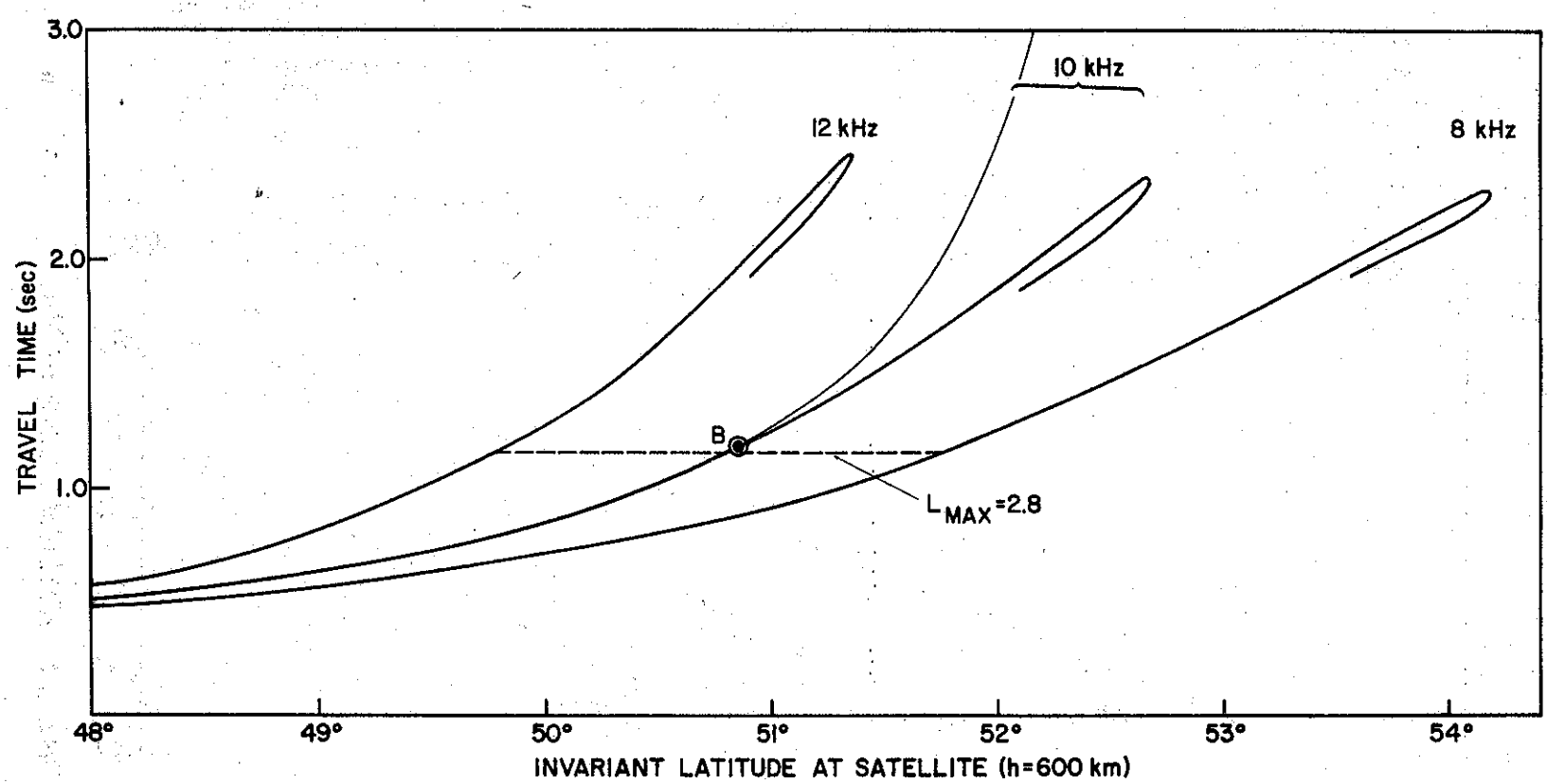

Figure 8a. Plot of calculated travel time versus observing latitude at 600 km in the conjugate hemisphere. For illustration, point B corresponds to the ray path A' - A of Figure 7a. The dashed line indicates the outermost L shell reached by the ray path. The thin line corresponds to the model with constant density at 1000 km shown in Figure 6.

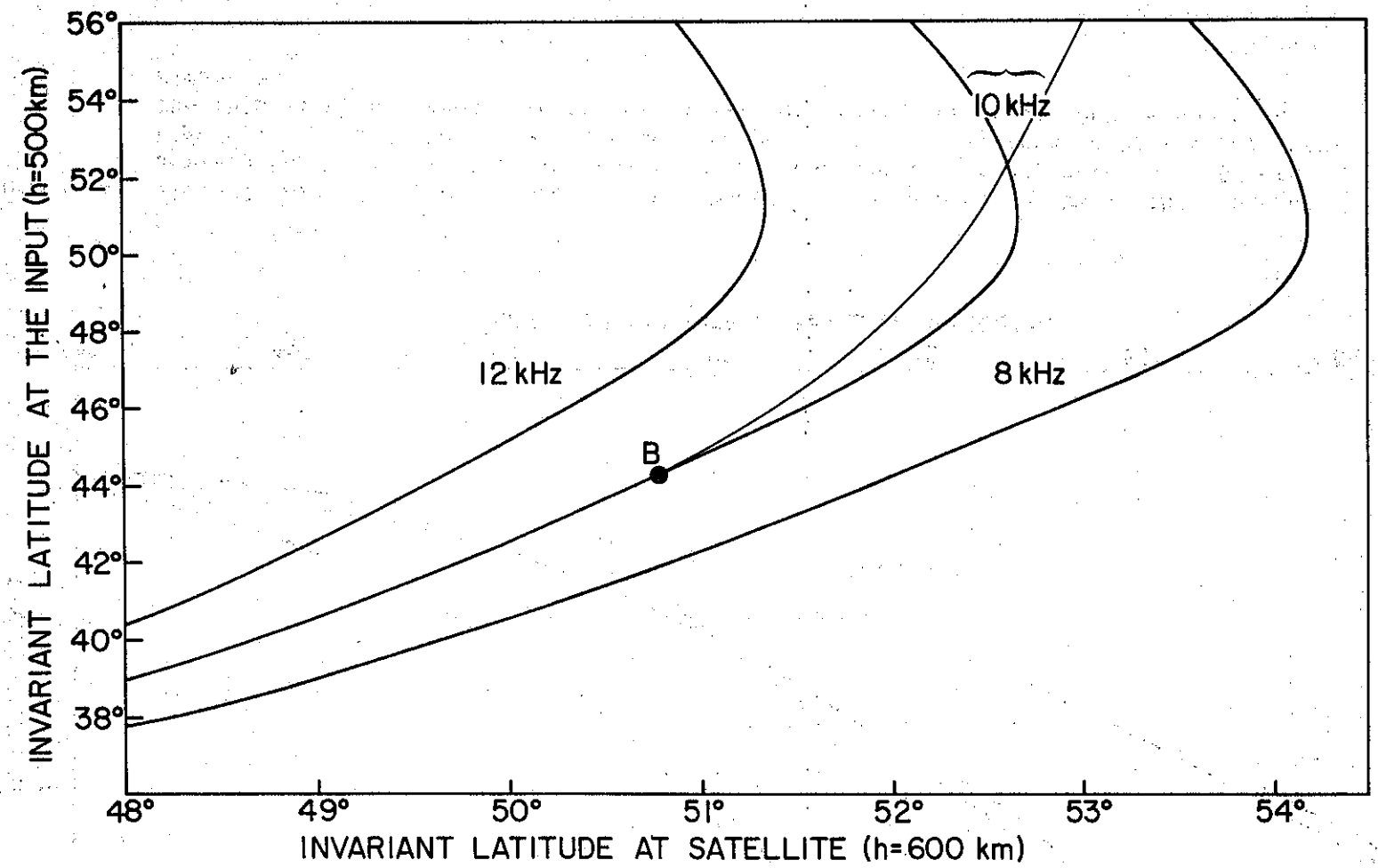

Figure 8b. Plot of calculated invariant input latitude at 500 km versus observing latitude at 600 km in the conjugate hemisphere. For illustration, point B corresponds to the ray path A' - A of Figure 7a. The thin line corresponds to the model with constant density at 1000 km shown in Figure 6.

and increases to ~ 2.0 sec for $f = 12$ kHz. For a fixed frequency, say $f = 10$ kHz, travel time increases with increasing starting and observing latitude (see also Figure 7a), ranging from near 0.8 sec at 50° observing latitude to ~ 2.0 sec at 52°. Note that over this 2° change in end-point latitude, the initial latitude changes by $\sim 6^{\circ}$, from $\sim 42^{\circ}$ to $\sim 48^{\circ}$.

Several features of the data will now be discussed in terms of the predictions of Figures 7 and 8.

1. Lower Cutoff Frequency Effects in the PR Mode

The downcoming rays in Figure 7 exhibit wave normals that are nearly, but not quite, transverse to the geomagnetic field. This condition continues on downward as long as the refractive index surface is open; that is, as long as the wave frequency is above the local lower hybrid resonance (LHR) frequency. Along the ray path if the LHR frequency reaches and then exceeds the wave frequency, the refractive index surface becomes closed and shrinks in size. This condition, combined with the large refractive indices generally encountered in the PR mode below a few thousand kilometers, leads to reflection as in the case of MR whistlers [Smith and Angerami, 1968]. Thus a satellite will not receive waves in the PR mode at frequencies below the maximum value of the LHR frequency above the spacecraft. If this maximum value does not change rapidly over a few degrees in latitude, WT whistlers observed on a single satellite pass should exhibit a relatively constant lower cutoff frequency. This is in fact the case, as Figure 3a illustrates.

Variation of the LHR frequency with height at an invariant latitude of 51° is shown in Figure 9 for the model magnetosphere used. The LHR frequency has two maxima, a lower one produced by the density peak at the

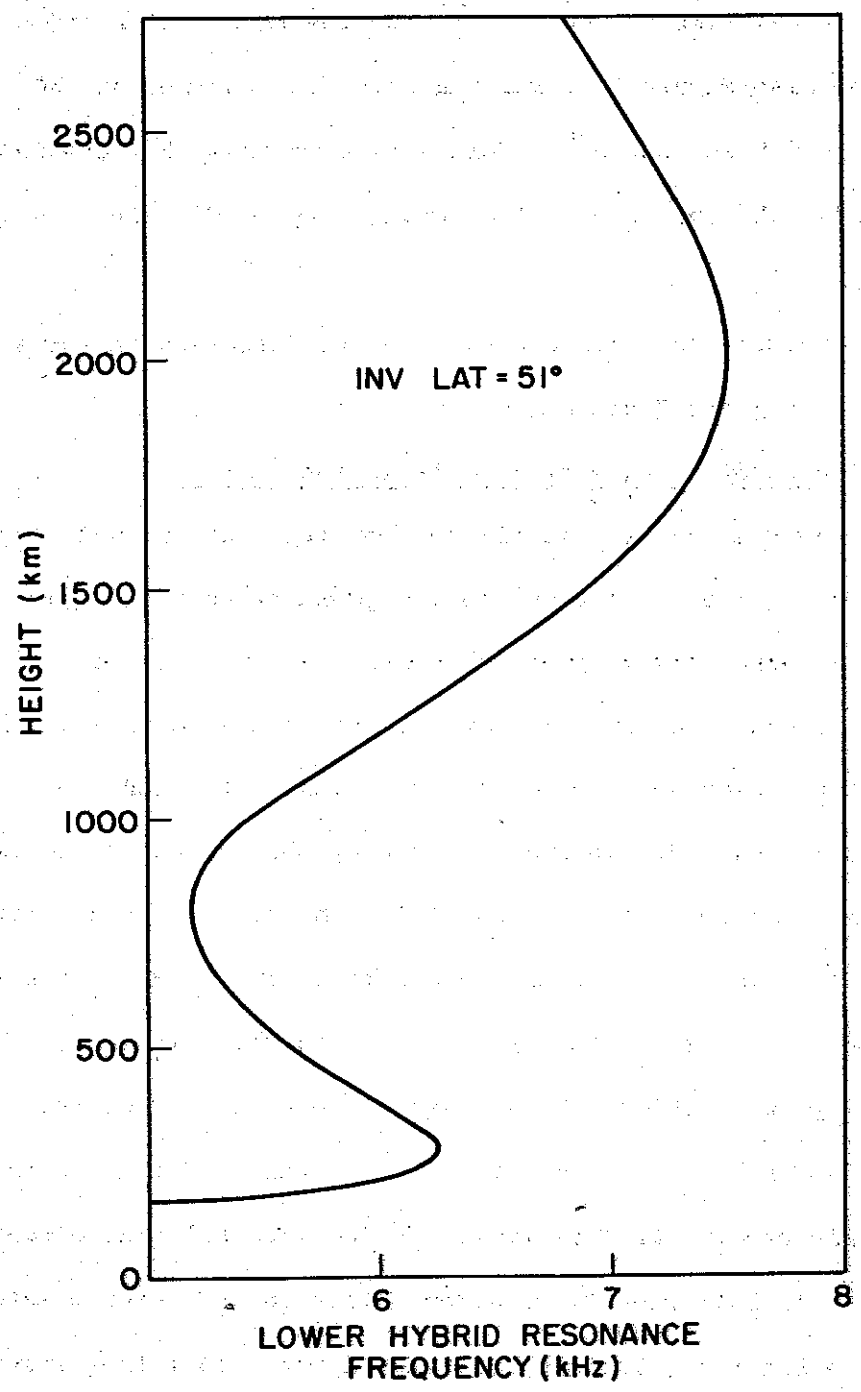

Figure 9. Behavior of the lower hybrid resonance (LHR) frequency with height at 51° invariant dipole latitude, for the model magnetosphere used.

F layer and an upper one by the transition from heavy ions (O^+) to light ions (H^+). In this work the term "maximum LHR frequency" will refer to the upper maximum. The curve in Figure 9 implies that WT whistlers observed by a satellite below 2000 km altitude will have a lower cutoff at 7.5 kHz (compare with data of Figure 3a and Figure 4 showing a lower cutoff at about 7.4 kHz).

Figure 9 implies that a satellite situated above the level of the maximum LHR frequency could receive both downcoming and reflected upgoing waves within a frequency range between the local and the maximum LHR below the satellite. A limited number of WT whistlers exhibiting this double component feature have been observed. An example, received by OGO 4 at an altitude of 792 km in the vicinity of Byrd Station, Antarctica, is shown in Figure 10. The WT whistler, indicated by the arrow, resembles a fish hook and is seen in a frequency range of 6 to 8.3 kHz. The portion between 6 and 7 kHz is observed again about 70 msec later, suggesting a reflection of these waves below the satellite in the manner proposed above. An example of a ray with this characteristic is shown in Figure 23.

WT whistlers of this kind yield information both on the value of the LHR at the satellite (minimum frequency reflected, 6 kHz in Figure 10) and on a lower bound for the maximum LHR below it (maximum frequency reflected, 7 kHz in Figure 10). The effect is similar to that producing the Nu whistler observed on the higher-altitude satellite OGO 1 [Smith and Angerami, 1968]. Reflection at the LHR frequency has also been studied by Smith et al., [1966] and Storey and Cerisier [1968] to explain bands of noise observed on the electric antenna of Alouette 1 near the LHR frequency [Barrington and Belrose, 1963; Brice and Smith, 1965].

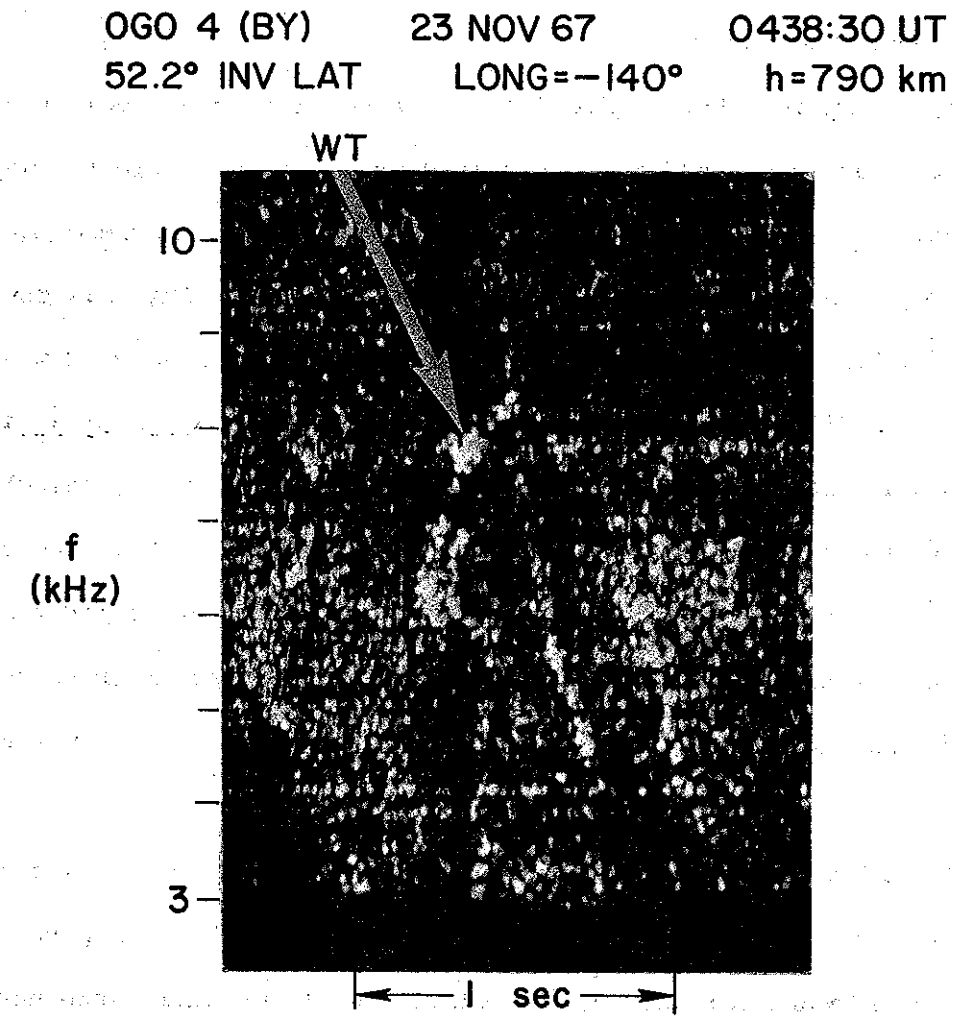

Figure 10. A frequency-time spectrogram of a walking-trace (WT) whistler (arrow) exhibiting two closely spaced components between the lower cutoff at 6 kHz and 7 kHz. The descending tone following the WT whistler was produced by the same lightning discharge.

2. Upper Cutoff Frequency Effects in the PR Mode

Figures 8a and 8b predict an upper cutoff frequency in WT whistlers, in the sense that rays at a given frequency will be confined within some upper limiting latitude. This effect can be appreciated from a comparison of the two ray paths for $f = 10$ kHz of Figure 7a. As input latitude increases, the value of L_{max} increases. However, the latitude of the point L_{max} also increases (along the thin line). This permits a considerable increase in length of the path segment over which the ray is tilted inward from B_o (segment corresponding to (4) - (5) of Figure 7b). Thus the increasing 'asymmetry' about the equator tends to compensate for the increase in L_{max}, and ray paths tend to cluster at a single value of L_{final}.

Variations in the model of electron density cause the locus of L_{max} in Figure 7a to be shifted or distorted. There are then appreciable changes in the predicted high frequency behavior in the PR mode. For example, in Figure 8b the solid curves based on the model exhibiting a horizontal density gradient (Figure 6) reach a maximum latitude of 52.7^{o} for a wave at $f = 10$ kHz starting at 50.8^{o}. Rays starting at higher initial latitudes cross over the other paths and arrive at latitudes less than 52.7^{o}, with lower travel times (see Figure 8a). However the thin line in the same figure (corresponding to constant density at 1000 km) extends above 52.7^{o}.

Both density models lead to predictions of a decrease in upper limiting frequency with increasing observing latitude. Clear upper cutoff effects of this kind are shown in Figure 12, middle of the upper panel. Additional comments on upper cutoff effects are given below in the section on comparison of calculated and observed spectra.

3. Latitudinal Limits of Observation of the PR Mode

PR mode propagation was identified in whistlers and/or Omega transmission on about 100 of 300 OGO-2 and OGO-4 passes representing the period August 1967 - February 1968. PR-mode effects were observed only in data from the range of invariant latitudes of 47° to 56°. One obvious mechanism for the high-latitude limit is a bandwidth effect, wherein the frequency range of the WT whistler decreases with increasing observing latitude until the upper and lower cutoff frequencies coincide. This tendency is illustrated in the upper panel of Figure 12, where the upper cutoff falls relatively smoothly from 13 kHz near 51° to about 5 kHz near 56°. The lower cutoff effects are not well defined here, being illustrated more clearly in Figure 3.

The high-latitude limiting-bandwidth effect is shown qualitatively in Figure 8a, where the observable bandwidth as a function of latitude is that region of plotted frequencies above the $f = 8$ kHz line (assuming that $f_{LHR(max)} \sim 8$ kHz). For example, at 51.37° the bandwidth is 4 kHz.

At low latitudes, observation of the WT trace is not in general limited by accessibility but rather by the reduction in the range of observable travel times. For example, Figure 8a shows that at low observing latitudes, say near 49°, the difference in travel time with increasing frequency is small; hence the characteristic rising form of Figure 3 is not observed.

4. Local Time of Occurrence of the PR Mode of Propagation

It was noted above (cf. Figure 8a) that the high-frequency, large-dispersion range of the WT whistler is highly sensitive to the electron density distribution in the upper ionosphere and magnetosphere. As

gradients of the type shown by the solid curve of Figure 6 are extended to lower L values, the effect in Figure 8 is to cause still larger departures from the behavior of the thin lines and to cause the double valued condition to arise at much lower travel times and input latitudes. The result is a prediction that the PR mode should not occur under daytime conditions that involve large-scale horizontal gradients in the ionosphere of the type shown by satellite experimenters such as Brace et al., [1967].

This prediction was verified by an analysis of VLF data from more than 300 real time passes of OGO 2 and OGO 4 for the period August 1967 to February 1968. The telemetry stations used were Byrd Station, Antarctica; Santiago and Quito, South America; Rosman, North Carolina; Johannesburg and Madagascar, South Africa. PR modes were observed only in data from Byrd, Johannesburg, Rosman and Madagascar, and as noted above, only in the range of invariant latitudes 47° to 56°.

Figure 11 illustrates the tendency for PR mode activity to be confined to nighttime hours. All data from all passages of OGO 4 over Johannesburg during the month of September 1967 are represented. Filled symbols indicate that the satellite was in the invariant latitude range of PR propagation, and squares indicate the presence of PR mode effects. The periods when the VLF receiver was connected with an electric antenna are indicated by the arrows labelled E. The solid vertical line indicates periods when the VLF experiment was turned off. Crosses indicate those passes on which the unbalanced electric antenna of OGO 4 did not operate properly due to strong interference in sunlight (J. Katsufrakis, personal communication). The approximate local times at the satellite are given by the dashed lines.

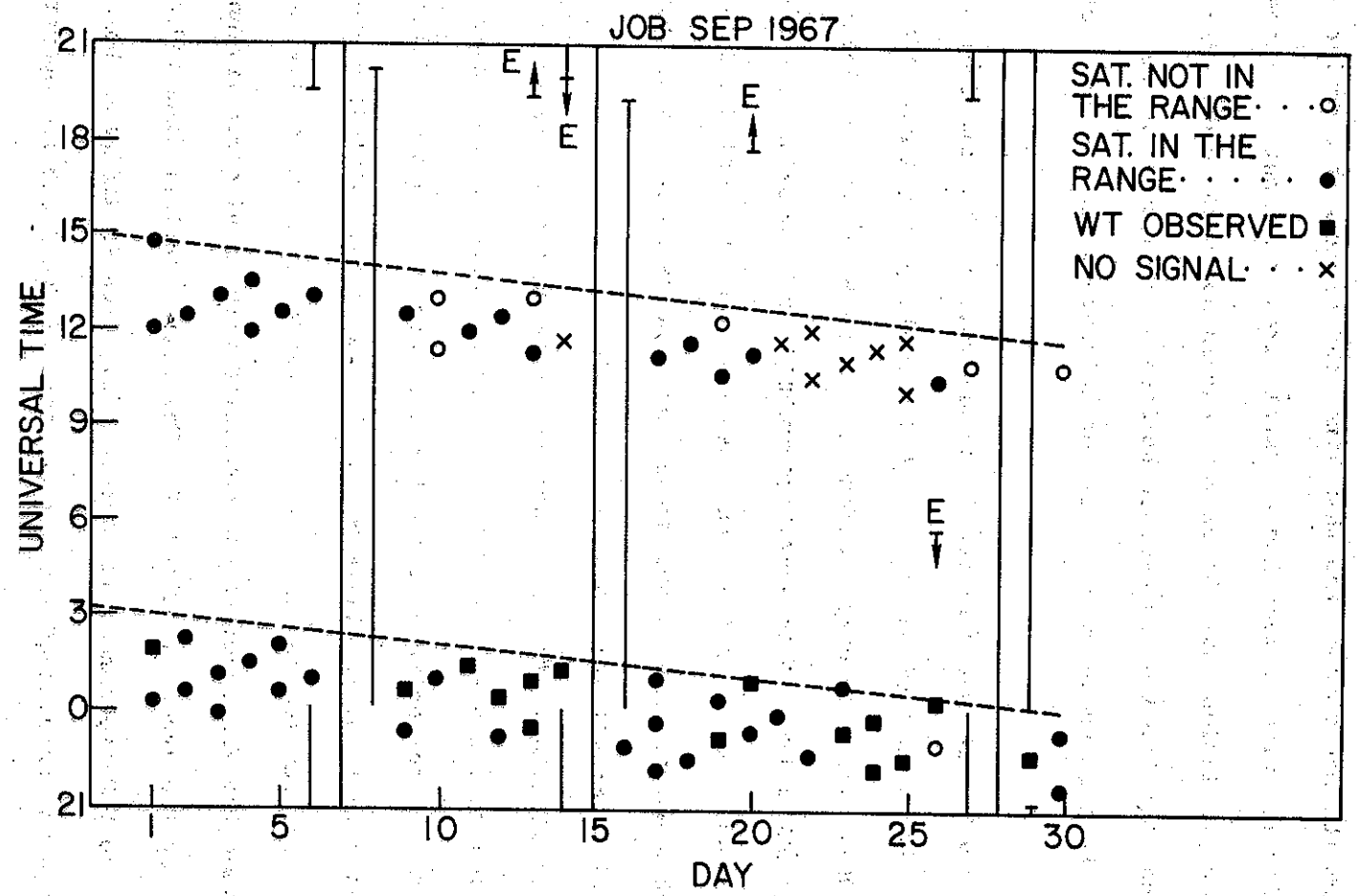

Figure 11. OGO-4 data showing a concentration of PR-mode activity on the nightside of the earth. Passes over Johannesburg (JOB) during the month of September, 1967 are represented in coordinates of universal time versus day of the month. The dashed line indicates the approximate local time of the passes. Symbols used to represent the data are shown at the upper right-hand corner of the figure (see text for details). Periods during which the VLF experiment was turned off are indicated by vertical lines. The periods of operation in an electric-antenna mode are indicated by E and arrows.

The figure indicates that the PR mode was observed only during local nighttime hours and that it was observed both by electric and magnetic antennas. The latter result is expected from the interpretation of the PR mode as an essentially electromagnetic phenomenon.

5. The Occurrence of the PR Mode as a Function of Magnetic Activity

There is as yet no evident dependence of the occurrence of WT whistlers on magnetic activity, at least within a range from very quiet conditions to conditions of moderate disturbance. For example, referring to Figure 11 and the observations during the month of September 1967 near Johannesburg, of the 15 passes involving PR mode observations, 10 were such that ΣK_p for the preceding day was < 20, 5 involved $\Sigma K_p > 20$.

6. Simultaneous Occurrence of the PR Mode and of Falling Tone Whistlers

The simultaneous occurrence of the rapidly varying walking-trace and the slowly varying falling-tone (1_-) whistlers of Figure 3 is apparently due to a condition in which there are horizontal gradients in the ionosphere. It was first thought that the constant-dispersion whistlers might be scattering from a duct. However recent research by R. Scarabucci (personal communication) suggests that they are nonducted but propagate at relatively small wave-normal angles, as a result of horizontal density gradients in portions of the magnetosphere. The presence of these gradients also limits the occurrence of WT whistlers in latitude, as shown in Figure 8.

D. COMPARISON BETWEEN CALCULATED AND OBSERVED WT WHISTLERS

The time-frequency spectra of the WT whistlers marked by heavy arrows in Figure 3a are shown by continuous lines in Figure 12 using the position of the lightning source (identified in Figure 3a) as a common time origin.

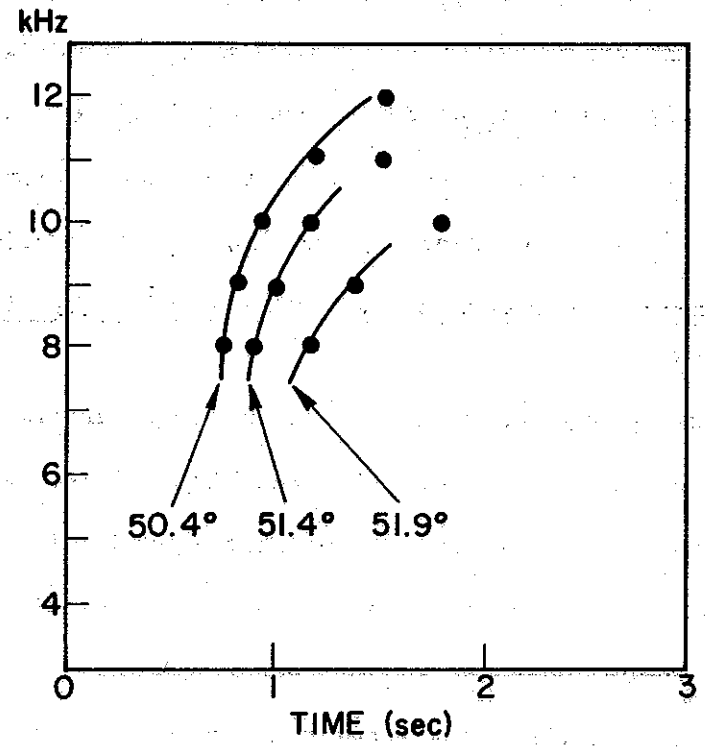

Figure 12. Comparison of calculated and observed WT-whistler spectra. The continuous lines are transcriptions of frequency-time spectra of WT whistlers observed at the invariant latitudes indicated. The examples were taken from the events marked by heavy arrows in Figure 3a, the lightning source positions serving as a common time origin. Spectra of WT whistlers calculated for invariant latitudes corresponding to those of the observations are shown by dots.

The time-frequency spectra of WT whistlers calculated for the invariant latitudes and altitudes where the observations were made are shown by dots in the same figure. The calculations were made by tracing rays in the model magnetosphere already described, and from which Figure 8 was produced. There is evidently very close agreement in travel time between the observed and calculated spectra.

There is also excellent agreement between calculated and observed spectra on lower cutoff frequency. This was achieved by choosing a model density with a maximum LHR frequency above the satellite (Figure 9) equal to the lower cutoff frequency of the observed whistlers.

The upper cutoff frequencies for the calculated WT whistlers are somewhat higher than the ones shown by the data in Figure 12. At 51.4° invariant latitude for instance, Figure 8 predicts an upper cutoff of about 12 kHz, whereas the observed WT whistler extends only to 10.5 kHz (Figure 13). Several mechanisms have been considered to account for such a discrepancy.

One possibility is that rays traveling beyond $L = 3.0$ are Landau absorbed, since in this region the wave normals in the PR mode make large angles with the geomagnetic field (cf. Figure 7). (This type of interaction has been proposed in order to explain the absence of MR whistlers at high L-shells [Thorne, 1968].) Before assessing the extent of this effect, it is necessary to examine the effect of horizontal gradients in the thermal plasma at low altitudes.

Another possibility is that an appropriate modification in the magnetospheric density model could lower the latitude of the upper cutoff shown in Figure 8b (nose of the solid curves). This hypothesis, which at present cannot be ruled out, involves further complications in the

density model and is under study.

A third possible explanation of the discrepancy is that the plasmapause was located near $L = 3.0$ at the time of the observations. This would essentially invalidate the predictions of Figure 8 for the behavior of rays near the line $L_{max} = 3.0$. This possibility may be discarded, since at the time of the observations, the plasmasphere extended at least to $L = 3.7$. This is shown by a plasmasphere level of equatorial density at $L = 3.7$ (dot in Figure 6) determined from nose whistlers received at OGO 4 within two minutes of the observations of the WT whistlers of Figure 3a.

III. FOCUSING AND DOPPLER SHIFTS IN THE PR MODE; OBSERVATIONS OF OMEGA FIXED-FREQUENCY TRANSMISSIONS

A. INTRODUCTION

The U.S. Navy has VLF transmitters in the range of frequencies from 10.2 to 13.6 kHz in different parts of the world. In Table 1 (for the period 16 August 1967 to 15 March 1968) is shown the approximate power transmitted, the frequencies of operation and the pattern at which the pulses are sent for each station. For instance, the station at Aldra (1) sends pulses at 10.2 kHz every ten seconds with 0.9 second duration. The location of these stations and of the telemetry stations for OGO 2 and OGO 4 is shown in Figure 13. Also the subsatellite path for an OGO-4 passage is indicated. Since the frequencies transmitted are in the range of the WT whistlers, it is expected that they must also propagate in this mode and be received at the conjugate hemisphere of the transmission with the same characteristics of the WT whistlers. Since the waves that produced the WT whistlers show large values for the phase refractive index, it is expected that these waves present Doppler shifts that may reach hundreds of Hertz and therefore may easily be observed in a frequency time spectrogram. Another phenomenon that may be observed on these fixed-frequency signals is the focusing effect due to the convergence of the energy at the opposite hemisphere of the transmission (see Figure 7a).

B. FOCUSING AND RELATED EFFECTS IN A CASE STUDY INVOLVING WHISTLERS AND FIXED-FREQUENCY SIGNALS

Focusing effects are a natural consequence of the convergence of ray paths discussed above in connection with Figure 7a. Figure 8b, for

Table 1. OMEGA TIME SCHEDULE

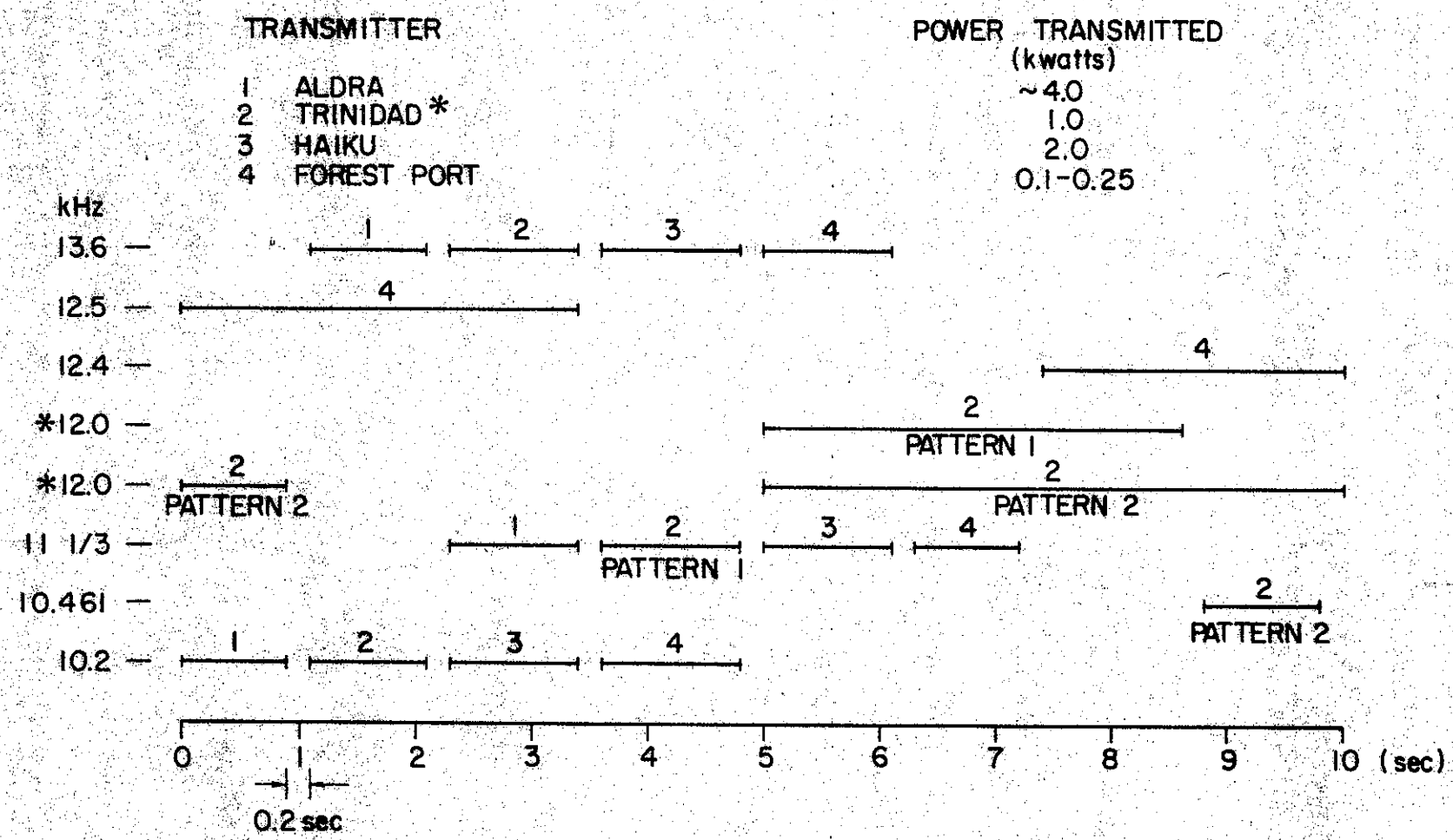

*TRINIDAD TRANSMITS EITHER PATTERN 1 OR PATTERN 2, USUALLY PATTERN 2

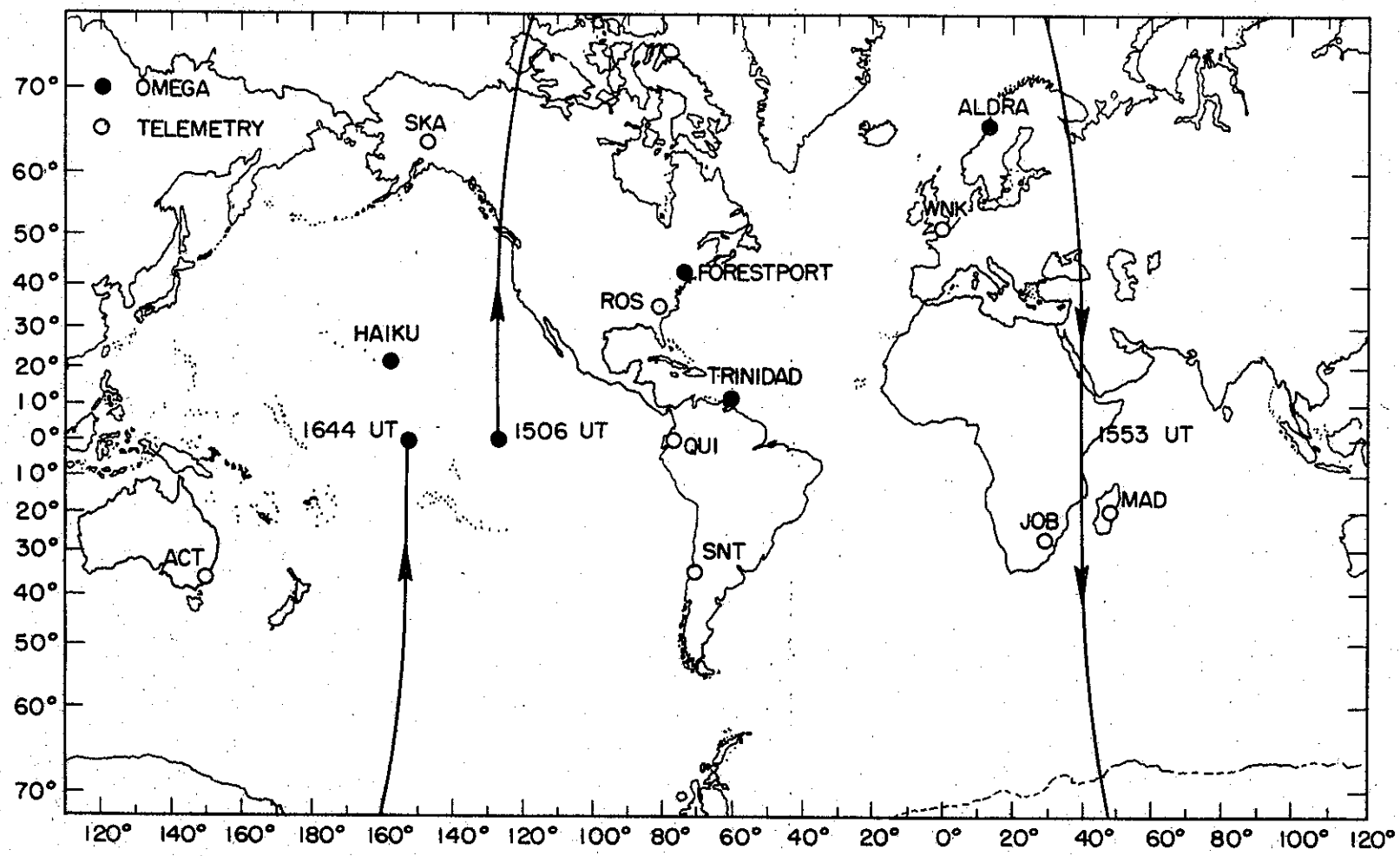

Figure 13. OGO-4 orbital subsatellite plot for revolution 1797 on November 27, 1967. Also shown are the locations of the U.S. Navy transmitter (Omega) and telemetry stations, except the telemetry station at Byrd (BY) which is located at LAT = 80.0°S and LONG = 120.0°W.

example, predicts that rays with a 6° spread in starting latitude arrive within a 2° range. Such effects, while observable in whistlers (compare the relative intensities of the WT and 1_{-} whistlers of Figure 4) are particularly clear in the observations of fixed-frequency VLF transmissions. The fixed frequencies from 10.2 to 13.6 kHz transmitted by the Omega stations are in the range of frequencies observed in WT whistlers, and when received by a satellite in the hemisphere conjugate to the transmitter generally exhibit characteristics similar to those of the prevailing WT whistler activity. Several such effects, including focusing, are illustrated in Figure 14, which shows OGO-4 spectra received near 50° latitude in the southern hemisphere. Horizontal lines at the right end of the panels identify the signal frequencies 10.2, 11-1/3, 12.4 and 12.5 kHz from the Omega transmitter in Forest Port, New York. In the top panel, the Omega signals appear as dashes of various lengths, and their intensity, as evidenced by the darkness of the display, drops sharply above and to the right of the sloping dark area that extends from $\sim 51^{\circ}$ to $\sim 56^{\circ}$. In the expanded time-scale portions of this record marked A and B and shown in the middle and bottom panels, the dark area may be identified as having been produced by WT whistlers, in the form of somewhat irregular rising tones. Some contribution to the darkness of the record is made by relatively pure, falling-tone whistlers that accompany many of the WT events. The stronger signals from Omega are interpreted as the result of propagation in the PR mode, the intensity enhancement near 50° being associated with the focusing effect predicted in Figure 7a or Figure 8b. The weaker signals from Omega received at higher latitudes are believed to reach the satellite on paths similar to those of the 1_{-} whistlers marked by asterisks in Figure 3a.

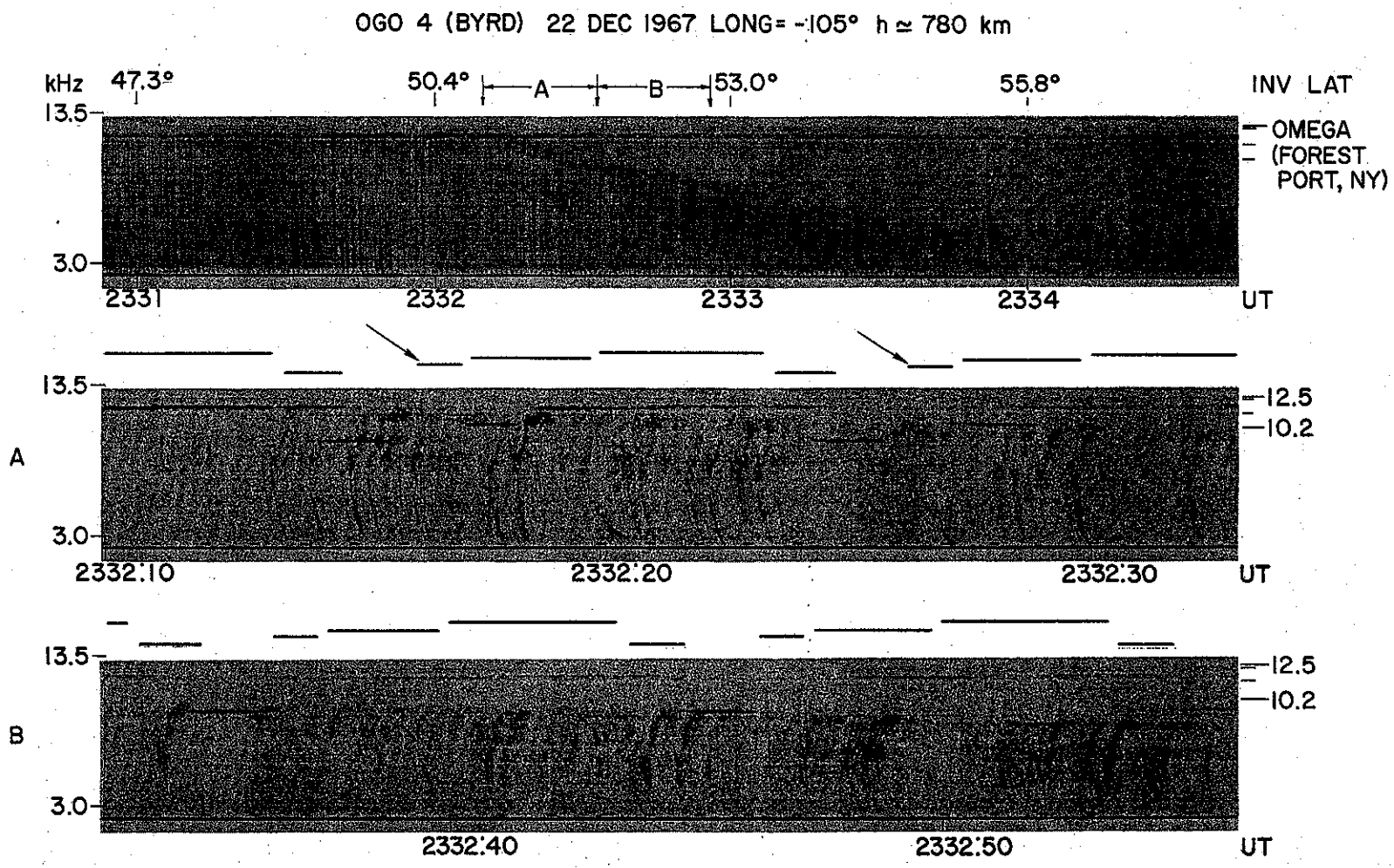

Figures 14. Frequency-time spectrograms of VLF data received on OGO 4 near Byrd Station, Antarctica. The sloping dark portion near the center of the top panel is produced by whistlers. The horizontal dashes of variable lengths above 10 kHz are signals from Omega (Forest Port, New York) at 10.2, 11-1/3, 12.4 and 12.5 kHz. The portions denoted A and B are presented with expanded time scale in the middle and bottom panels. Above these panels, the schedule of pulses transmitted from Omega (Forest Port) is shown for comparison with the received signals (see text).

The schedule of the transmitted pulses from Omega (Forest Port) is shown immediately above the middle and bottom panels in Figure 14. From a careful comparison of the transmitted and received pulses, it was found that the travel times of Omega signals increase rapidly with latitude, in agreement with the predictions for the PR mode (cf. Figure 8a). This increase in travel time with latitude may be seen in panel A in the case of two pulses transmitted at 11-1/3 kHz (arrows). The travel time from the trailing edge of the first transmitted pulse to the trailing edge of the corresponding received signal (below and just to the right) is $\sim$ 1.1 sec. For the second pulse the time is increased to $\sim$ 1.5 sec. The pulses received in the PR mode are longer than those transmitted, especially near the high-latitude cutoff. This is consistent with the behavior of the WT whistlers in the same figure, which on close inspection may be seen to exhibit pronounced increases in travel time with increasing frequency near the upper limiting frequency.

C. DOPPLER SHIFT EFFECTS IN THE PR MODE

The low phase velocities resulting from nearly transverse propagation at the end of the nonducted path (see Figure 7a) can cause a substantial Doppler shift when such waves are observed by a polar, low altitude satellite such as OGO 4. Also, the Doppler shift can be positive or negative depending on whether the satellite is moving equatorward or poleward. The phase refractive indices calculated for three different frequencies are plotted as a function of invariant latitude in Figure 15, where point C corresponds to point B of Figure 8 (the thin line corresponds to the model of electron density constant at 1000 km (cf. Figure 6). The relative Doppler shifts can be approximately obtained

from the scale on the right, which was calculated taking the average velocity of OGO 4 to be 7.5 $km \cdot sec^{-1}$, horizontal, and in the magnetic meridian plane. The angle between the wave normal and the satellite velocity was taken as the complement of the average dip angle for the range of latitudes shown since, as already stated, the wave normal lies close to the normal to the magnetic field in this region. The plot predicts that the magnitude of the Doppler shift should increase both with frequency and latitude.

Clear evidence of Doppler and focusing effects in Omega signals has been found in records from twelve OGO-2 and OGO-4 passes. The Doppler shifts were negative in all but two cases, due to the poleward direction of satellite motion on most of the passes suitable for observing PR mode effects. (The number of such passes is limited by local time restrictions on the distribution of electron density (described above), and by the requirement of approximate conjugacy to an Omega transmitter.)

Figure 16 shows examples from OGO 4 of Doppler shifts in PR mode signals from the Omega transmitter in Aldra, Norway. The transmission schedule of pulses at 10.2 and 11-1/3 kHz is indicated in the upper margin. A negative shift (consistent in sign with the poleward direction of satellite motion) is particularly well illustrated by the first pair of signals near 11-1/3 kHz (see Figure 5 for an expanded version of this part). The first weaker signal, corresponding to the 1_- whistler of Figure 3a, exhibits no frequency shift. The second, PR mode pulse, exhibits a clear negative offset of about 100 Hz, and is visibly more intense than the other signal. A similar Doppler shift effect ($\sim$ 100 Hz) is presented at higher latitudes by the pair of signals produced by the third transmitted pulse at 10.2 kHz. The two preceding signals at this

frequency, received at lower latitudes, exhibit no detectable Doppler shift (less than 10 Hz), indicating that at this point the projection of the refractive index along the velocity of the satellite was less than ~ 50. Note that as the signal frequency is lowered, the latitude at which a given Doppler shift is observed increases, in agreement with the calculations plotted in Figure 15. This example (Figure 16) illustrates the confinement of PR mode-signals to a narrow range of latitudes, and their relatively high amplitudes.

A quantitative comparison between the Doppler shift calculated by ray tracing and the observations is not given here, for reasons explained in a later section on models of the earth's magnetic field.

D. DISCUSSION

1. Earth's Magnetic Field Model

Up to now rays have been traced in a two dimensional magnetosphere where the earth's magnetic field is represented by a centered dipole. By tracing field lines in a magnetic field mode given by Cain et al., [1968] it has been found that this field is well represented by a centered dipole in the range of L values considered here and near the longitudes of Rosman ($\sim 97^{\circ}$W), but not near the longitudes of Johannesburg ($\sim 41^{\circ}$E), where the magnetic field lines are asymmetric. Under these conditions, it is not clear how to compare the results of ray tracings performed in a dipole field with observations near Johannesburg. A three-dimensional ray tracing in a magnetic field represented by a harmonic expansion [Cain et al., 1968] was therefore developed [Walter, 1969] and used for a closer comparison with the data, using geographic coordinates.

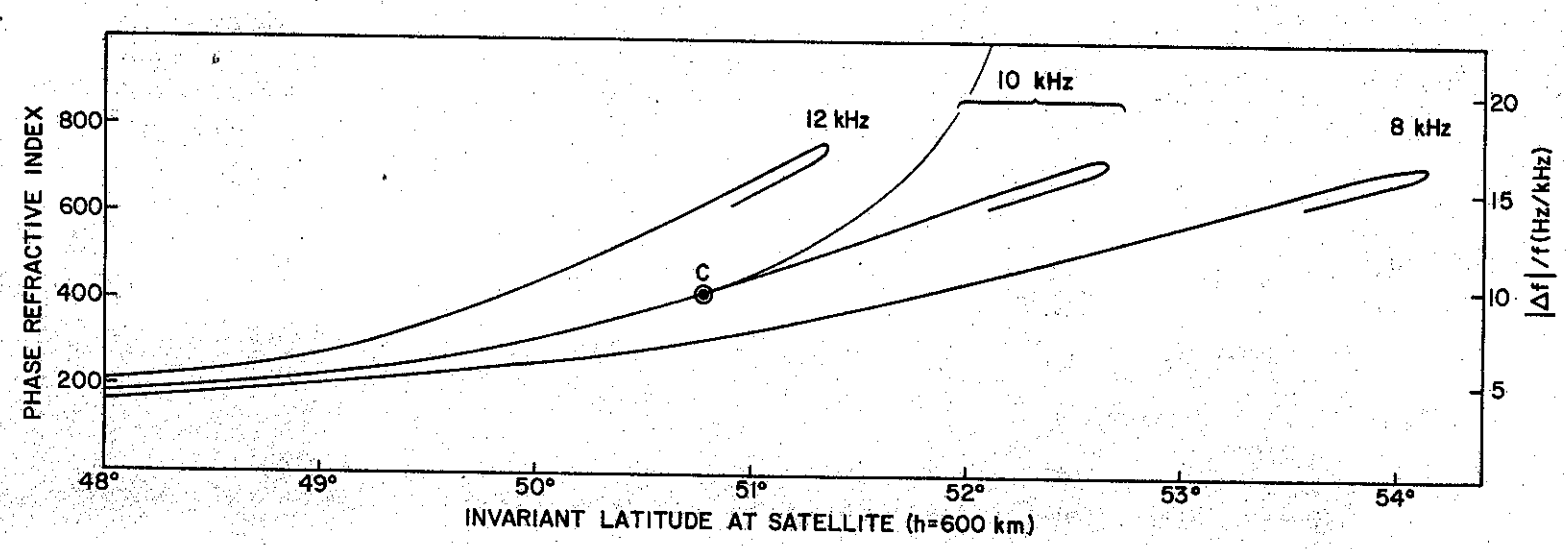

Figure 15. Plot of calculated phase refractive index as a function of invariant latitude for three different frequencies. For illustration, point C corresponds to point B in Figure 8a and to path A' - A (Figure 7a). The righthand scale gives approximately the ratio between the expected Doppler shift (in Hz) and the wave frequency (in kHz), calculated for a satellite with velocity of 7.5 km/sec, assumed horizontal and in the magnetic meridian plane. The thin line represents calculations for the model with constant density at 1000 km shown in Figure 6.

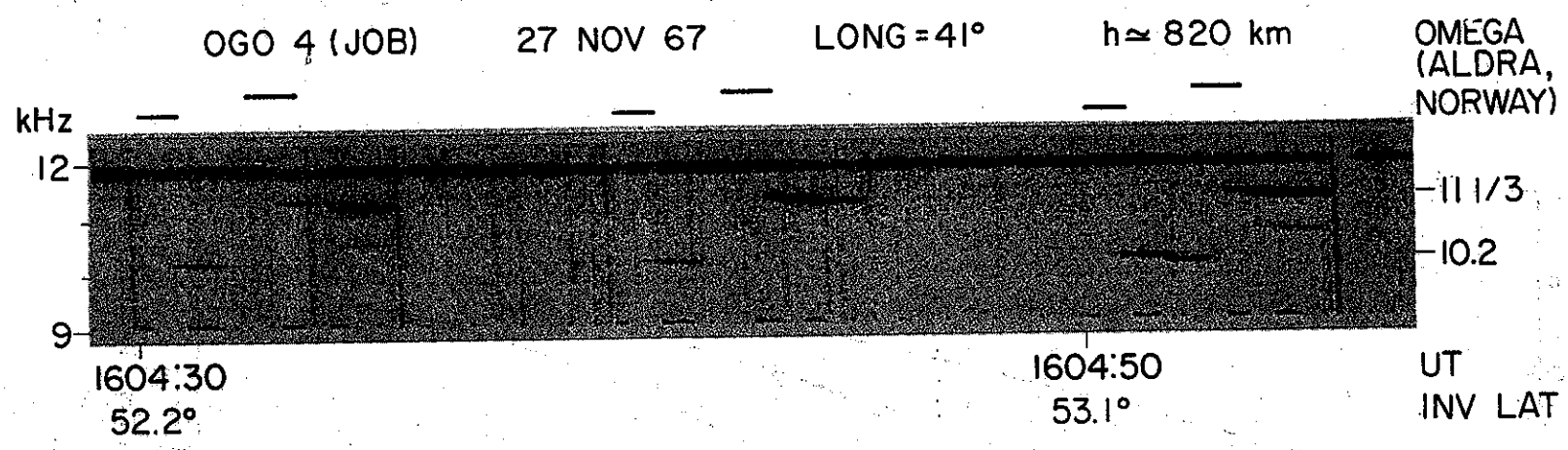

Figure 16. OGO-4 frequency-time spectra received near Johannesburg, South Africa, illustrating Doppler shifts in signals from the Omega transmitter in Norway at 10.2 and 11-1/3 kHz. The segments just above the spectrogram show the pattern of transmitted pulses. The first transmitted pulse at 11-1/3 kHz produces two clearly distinct signals received at the satellite (an expanded record of this event is shown in Figure 5). The first signal is weaker and probably follows the same path as most of the whistlers observed in this run (shown as nearly vertical traces). The segment with larger travel time is considerably stronger and propagates to the satellite in the PR mode, exhibiting a negative Doppler shift of about 100 Hz. A similar behavior is shown by the received signals produced by the last transmitted pulse at 10.2 kHz. The effect of flutter in the original tape recorder is apparent in the strong signal near 11.9 kHz (a transmission from an unidentified VLF transmitter).

Doppler shift results from the calculations using the two-dimensional (dipole field) and the three-dimensional ray tracings [Cain et al., 1968] were compared for longitudes near Johannesburg ($\sim 41^{\circ}$E). It was found that the latitude at which a given Doppler shift (of $\sim$ 100 Hz at 10 kHz) should be observed is about 1° lower for the dipole representation. Considering that the characteristics of signals propagating in the PR mode change very rapidly with latitude (note in Figure 3 the change in the spectra of WT whistlers observed in a range of 1.5° in latitude), one sees that a discrepancy of 1° is too large. As predicted, the magnetic field model has a first order effect on the PR mode of propagation and it is of little value to fit the data by changing density models only.

2. The Electron Density Model

The electron density model used in the calculations of Figure 12 was developed on the basis of several independent sources of information. These included: 1) a value of equatorial electron density (shown as a dot at $L = 3.7$ in Figure 6) deduced from a whistler received at the satellite within two minutes of the observations illustrated in Figure 3a; and 2) an estimate of a maximum LHR frequency above the satellite of 7.4 kHz from the lower cutoff frequency of the WT whistler of Figure 3a. Successive approximations within the constraints of this evidence led to the diffusive equilibrium model described earlier and summarized (in terms of electron density) in Figure 6.

Another bit of evidence obtained since the calculations were made suggests that the model is representative of actual conditions prevailing in the magnetosphere at the time. This evidence, kindly provided by L. Colin of the NASA/Ames Research Center, Moffett Field,

California, involves Alouette-2 topside sounder data obtained within 40 minutes and 30° longitude of the OGO-4 pass in question. The analysis showed an electron density of $\sim 7{,}500$ el cm^{-3} at 1000 km and latitude 45°, in close agreement with the model used.

IV. RAY-TRACING EQUATIONS

A. INTRODUCTION

Haselgrove [1954] derived the three dimensional ray equations based on Fermat's principle. Those same equations were also derived by Budden [1961] using the eikonal concept. The ray equations are derived here for the case of a two-dimensional geometry. When the parameters of the medium are known, that is the density and the static magnetic field vector are known at each point, only a closed set of three differential equations is necessary to determine the position of the wave packet, that is, to find the ray path. These differential equations are the time variation of the coordinates, plus the time variation of an angle that gives the wave normal direction.

B. TWO-DIMENSIONAL RAY EQUATIONS

To find these equations two hypotheses are made with respect to the phase refractive index in the range of frequencies of interest. The first requirement is that the medium must not present an anomalous phase refractive index. This is necessary in order for the concept of group velocity to be applicable. The second assumption is that the medium is slowly varying, or that the WKB solution is valid (see for instance Budden [1961]).

Based on the concept of group velocity, the time variation of the coordinates of a wave packet in a cartesian system is derived as follows. Supposing a wave packet moving from A to B (Figure 17), the following differential equations can be written:

$$\frac{dx}{ds} = \sin\beta \qquad (1)$$

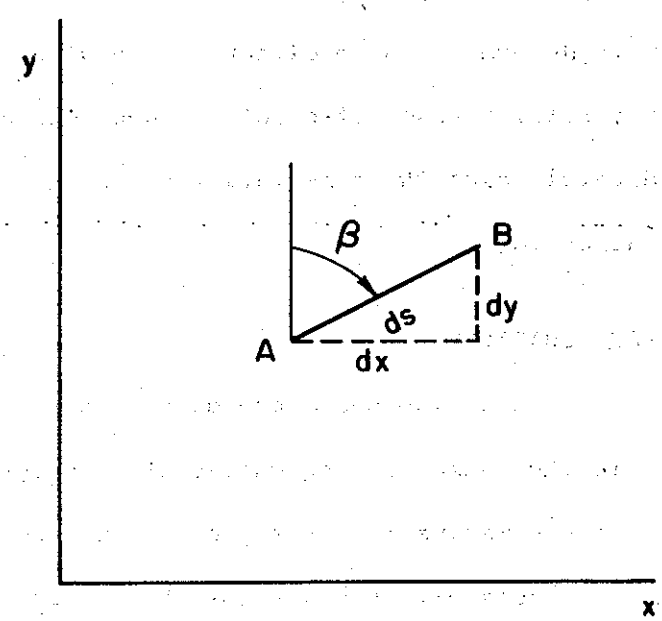

Figure 17. Wave packet moving from A to B. An elemental length on the ray path is ds, and β is the angle of the energy direction with the y axis.

and

$$\frac{dy}{ds} = \cos\beta$$

where x and y are the coordinates of the wave packet, s is the length measured along the ray path and β is the angle between the y-axis and the ray path. Denoting by t_g the time for the wave packet to move from A to B and V_{gr} as the ray group velocity, the above equations may be written in the following form:

$$\frac{dx}{dt_g} = V_{gr} \sin\beta \tag{2}$$

and

$$\frac{dy}{dt_g} = V_{gr} \cos\beta \tag{3}$$

since

$$\frac{ds}{dt_g} = V_{gr} .$$

The group ray velocity is given by:

$$V_{gr} = V_g/\cos\alpha, \tag{4}$$

where V_g is the group velocity (in the wave normal direction) defined as:

$$V_g = \frac{c}{\mu_g} \tag{5}$$

where c is the velocity in a vacuum and μ_g the group refractive index defined as:

$$\mu_g = \frac{\partial(\mu f)}{\partial f} = \mu + f\,\frac{\partial\mu}{\partial f} \tag{6}$$

The angle α measured in a clock-wise sense from the wave normal to the ray energy direction, expressed as:

$$\alpha = \tan^{-1}\left(-\frac{\partial(\log\mu)}{\partial\psi}\right), \tag{7}$$

with ψ as the angle measured clockwise from the static magnetic field to the wave normal vector.

The angle β may be expressed as (see Figure 18):

$$\beta = \phi + \alpha \tag{8}$$

where ϕ is the angle between the y-axis and the wave normal. The angle ψ may be expressed as a function of ϕ and γ (the angle between the y-axis and the magnetic field, see Figure 18).

To have a closed set of differential equations the time variation of ϕ will be found.

Taking the wave front that represents the principal wave at two different phase times, the way in which ϕ evolves with time is given by:

$$\frac{d\phi}{dt} = - \frac{\partial \vec{V}ph}{\partial \ell} \cdot \vec{k} = \frac{c}{\mu^2} \frac{\partial \mu}{\partial \ell} \bigg|_{\phi} \tag{9}$$

where $\partial\mu/\partial\ell|\phi$ is the variation of the phase refractive index on the wave front, and therefore the direction of wave normal is maintained constant (ϕ = constant). The phase refractive index as a function of the position (x,y) and of the angle ϕ with the y-axis, results in:

$$\frac{\partial \mu}{\partial \ell}\bigg|_{\phi} = \frac{\partial \mu}{\partial x}\bigg|_{\phi} \cos\phi - \frac{\partial \mu}{\partial y}\bigg|_{\phi} \sin\phi \tag{10}$$

and therefore Eq. (9) may be written as:

$$\frac{d\phi}{dt} = \frac{c}{\mu^2} \left[\frac{\partial \mu}{\partial x} \cos\phi - \frac{\partial \mu}{\partial y} \sin\phi \right] \tag{11}$$

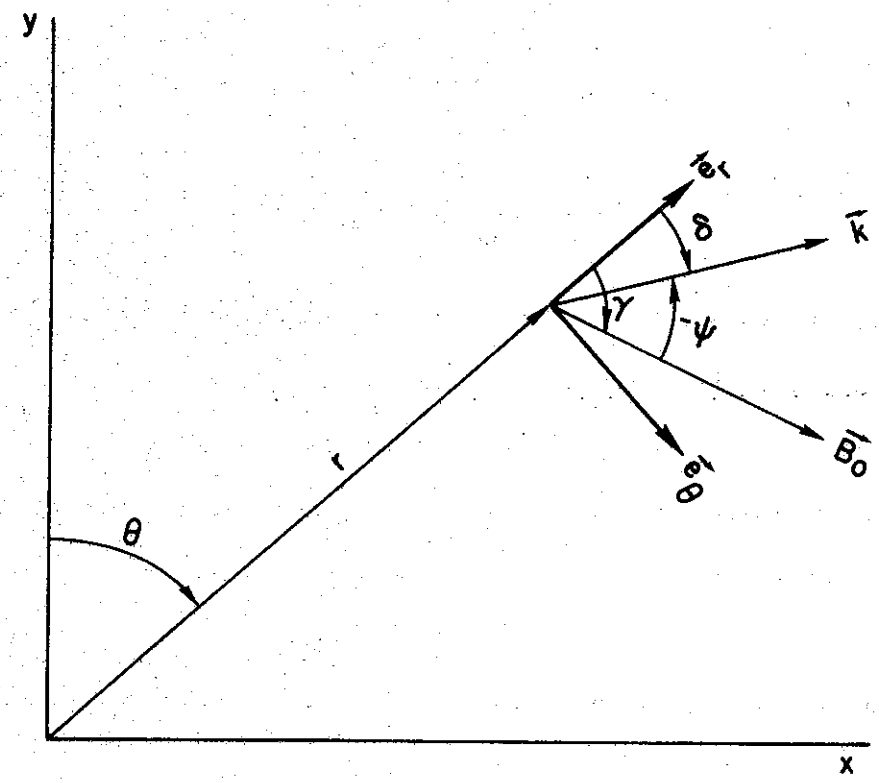

Figure 18. Origin of the angles is shown. The angles are positive in the clockwise direction. The wave normal direction is $\vec{k}$, and $\vec{B}_o$ is the static magnetic field.

Taking now as an independent variable the phase time, t, and knowing that

$$\frac{dt}{dt_g} = \frac{\mu}{\mu_g} , \tag{12}$$

Eqs. (2) and (3) may be written in the following way:

$$\frac{dx}{dt} = \frac{c}{\mu \cos\alpha} \sin\beta \tag{13a}$$

and

$$\frac{dy}{dt} = \frac{c}{\mu \cos\alpha} \cos\beta \tag{13b}$$

Equations (11), (13a) and (13b) form a set of differential equations suitable for solving in a digital computer.

The densities and the magnetic field are in general expressed in terms of polar coordinates and, therefore, it is convenient to express the equations above, Eq. (11) and Eqs. (13a-b) in this same system of coordinates.

Equations governing the position of the ray path in polar coordinates are easily obtained (see Figure 19):

$$\frac{dr}{dt_g} = V_{gr} \cos\beta \tag{14a}$$

$$\frac{d\theta}{dt_g} = \frac{V_{gr}}{r} \sin\beta \tag{14b}$$

Taking the phase time as the independent variable and using the relation, Eq. (12), the above equations may be written in the following way:

$$\frac{dr}{dt} = \frac{c}{\mu \cos\alpha} \cos\beta \tag{15a}$$

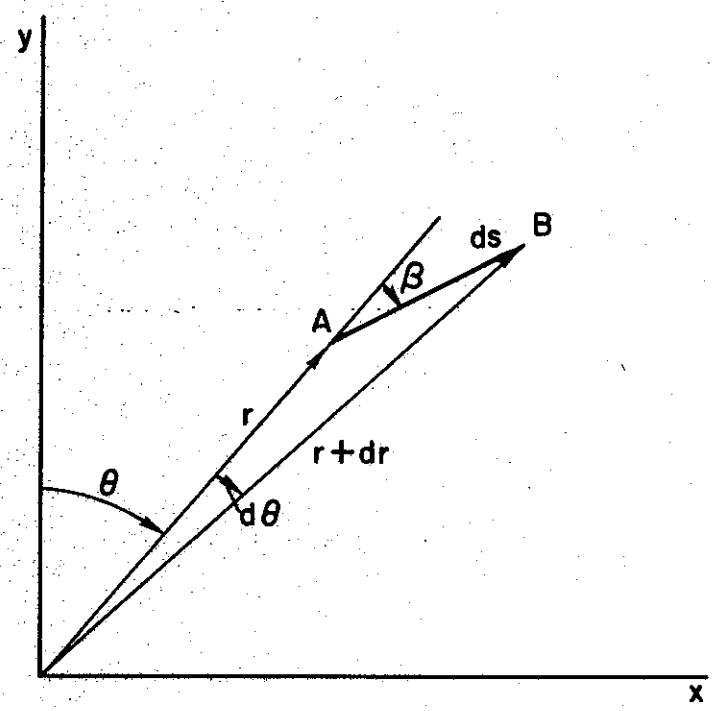

Figure 19. The polar coordinates of a point A on the ray path are θ and r, ds is the elemental length on the ray path, and β is the angle between the radial and the energy direction.

and

$$\frac{d\theta}{dt} = \frac{c}{r\,\mu\,\cos\alpha}\,\sin\beta\ . \tag{15b}$$

Using δ as the angle between the wave normal and the radial vector, the following relations may be written:

$$\delta = -\,\theta + \phi \tag{16}$$

and

$$\frac{d\delta}{dt} = -\,\frac{d\theta}{dt} + \frac{d\phi}{dt} \tag{17}$$

where $d\theta/dt$ is given by Eq. (15b), and $d\phi/dt$ is

$$\frac{d\phi}{dt} = -\,\frac{\partial\vec{V}ph}{\partial t}\cdot\vec{k} \tag{18}$$

or

$$\frac{d\phi}{dt} = -\,\frac{c}{\mu^2}\left[\left.\frac{\partial\mu}{\partial r}\right|_{\phi,\theta}\sin\delta - \frac{1}{r}\left.\frac{\partial\mu}{\partial\theta}\right|_{\phi,r}\cos\delta\right] \tag{19}$$

Therefore,

$$\frac{d\delta}{dt} = -\,\frac{c}{\mu^2}\left[\frac{\partial\mu}{\partial r}\sin\delta - \frac{1}{r}\frac{\partial\mu}{\partial\theta}\cos\delta\right] - \frac{c}{\mu r}\,(\sin\delta+\tan\alpha\cos\delta) \tag{20}$$

Now writing the phase refractive index as a function of r, θ, and δ:

$$\left.\frac{\partial\mu}{\partial r}\right|_{\phi} = \left.\frac{\partial\mu(r,\theta,\delta)}{\partial r}\right|_{\theta,\delta} + \frac{\partial\mu}{\partial\delta}\,\frac{\partial\delta}{\partial r} \tag{21}$$

and

$$\left.\frac{\partial\mu}{\partial\theta}\right|_{\phi} = \left.\frac{\partial\mu(r,\theta,\delta)}{\partial\theta}\right|_{\theta,\delta} + \frac{\partial\mu}{\partial\delta}\,\frac{\partial\delta}{\partial\theta} \tag{22}$$

Because

$$\frac{\partial\delta}{\partial r} = 0$$

and

$$\frac{\partial\delta}{\partial\theta} = -1$$

Therefore:

$$\frac{d\delta}{dt} = -\frac{c}{\mu^2}\left[\frac{\partial\mu}{\partial r}\sin\delta - \frac{1}{r}\frac{\partial\mu}{\partial\theta}\cos\delta\right] - \frac{c}{\mu r}\sin\delta \qquad (23)$$

In Appendix D it is shown that Eqs. (15a-b) and (23) are equivalent to the ones derived by Haselgrove [1954].

A set of differential equations in polar coordinates for the ray-tracing problem was obtained. To solve these equations it is necessary to assume a phase refractive index, which is carried out in the next section.

C. EQUATIONS NECESSARY FOR A TWO-DIMENSIONAL RAY-TRACING PROGRAM

The two-dimensional ray-tracing equations in polar coordinates are:

$$\frac{dr}{dt} = \frac{c}{\mu}(\cos\delta - \tan\alpha\,\sin\delta) \qquad (24)(379)^*$$

$$\frac{d\theta}{dt} = \frac{c}{r\mu}(\sin\delta + \tan\alpha\,\cos\delta) \qquad (25)(380)$$

$$\frac{d\delta}{dt} = -\frac{c}{\mu^2}\left(\frac{\partial\mu}{\partial r}\sin\delta - \frac{1}{r}\frac{\partial\mu}{\partial\theta}\cos\delta\right) - \frac{c}{r\mu}\sin\delta \qquad (26)(381)$$

---

*The second number corresponds to the left-most number on the listing of the program (Appendix A).

where

r and θ - polar coordinates of the ray path,

μ - phase refractive index,

t - phase time of the principal wave,

α - angle between the wave normal and the energy,

δ - angle between the radial vector and the wave normal.

The differential equation that governs the group delay time t_g is

$$\frac{dt_g}{dt} = \frac{\mu_g}{\mu} , \qquad (27)(382)$$

where μ_g is the group refractive index.

To solve the set of Eqs. (24) to (27), it is necessary to have the phase refractive index as well as its partial derivatives with respect to r, θ and ψ, and the group refractive index.

Assuming the cold plasma approximation the phase refractive index is given by the equation (see Stix [1962]):

$$A\mu^4 - B\mu^2 + C = 0 , \qquad (28)$$

with solutions given by

$$\mu^2 = \frac{B \pm F}{2A} , \qquad (29)$$

where

$$A = S \sin^2\psi + P \cos^2\psi , \qquad (30)(252)$$

$$B = RL \sin^2\psi + PS (1 + \cos^2\psi) , \qquad (31)(253)$$

$$C = PRL , \qquad (32)(254)$$

$$F^2 = B^2 - 4AC , \qquad (33)$$

ψ = angle between the wave normal and the static magnetic field vector,

$$S = \frac{1}{2}(R + L) , \qquad (34)(246)$$

$$D = \frac{1}{2}(R - L) , \qquad (35)(247)$$

$$R = 1 - \sum_i X_i \frac{1}{1 + Y_i} , \qquad (36)(242)$$

$$L = 1 - \sum_i X_i \frac{1}{1 - Y_i} , \qquad (37)(243)$$

$$P = 1 - \sum_i X_i , \qquad (38)(244)$$

$$X_i' = \left(\frac{f_{oi}}{f}\right)^2 \qquad (39)(215)$$

f_{oi} = the plasma frequency of the ith ions (40)(214)

f = the wave frequency,

$$Y_i = \frac{f_{Hi}}{f} , \qquad (41)(209)$$

$$f_{Hi} = \frac{\epsilon_i e B_o}{m_i} \text{ (gyrofrequency of the } i^{th} \text{ ion)}, \qquad (42)$$

ϵ_i = the signal of the charge of the ith ion,

e = a positive number equal to the electron charge,

B_o = the static magnetic field of the medium,

m_i = the mass of the ith ion.

The possible positive solutions for Eq. (28), in the case of a four component plasma (electrons, protons $[H^+]$, helium $[He^+]$ and oxygen $[O^+]$ ions), lie in the shaded area shown in Figure 20a where μ^2 is plotted against wave frequency. In this figure only the solutions of μ^2 are shown for frequencies below the electron gyrofrequency. In Figure 20b only the region for which Figure 20a is modified is shown for the case in which the plasma frequency is below the electron gyrofrequency.

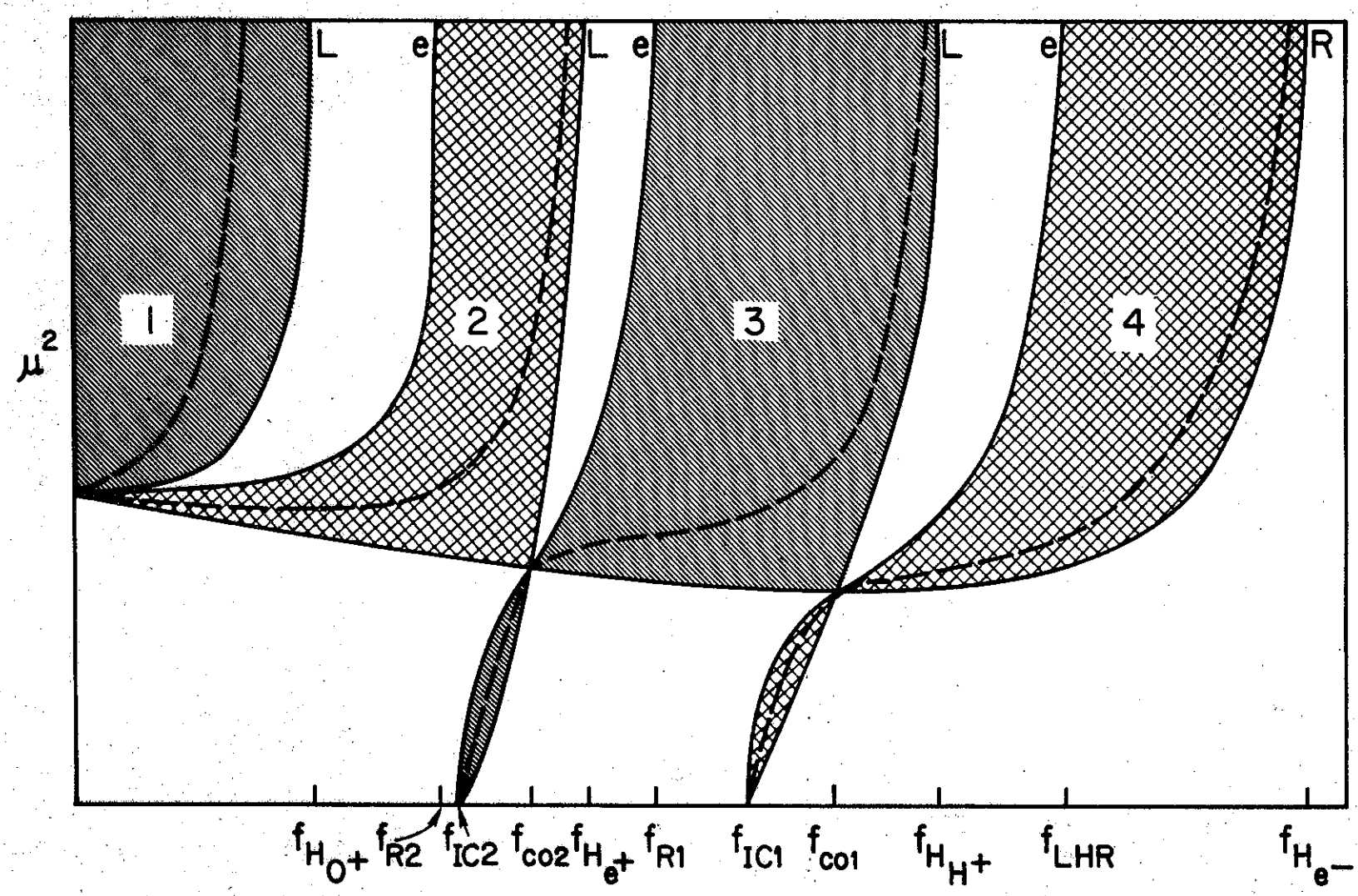

Figure 20a. The positive solutions for μ^2 are shown as a function of frequency; case that the electron gyrofrequency is below the plasma frequency.

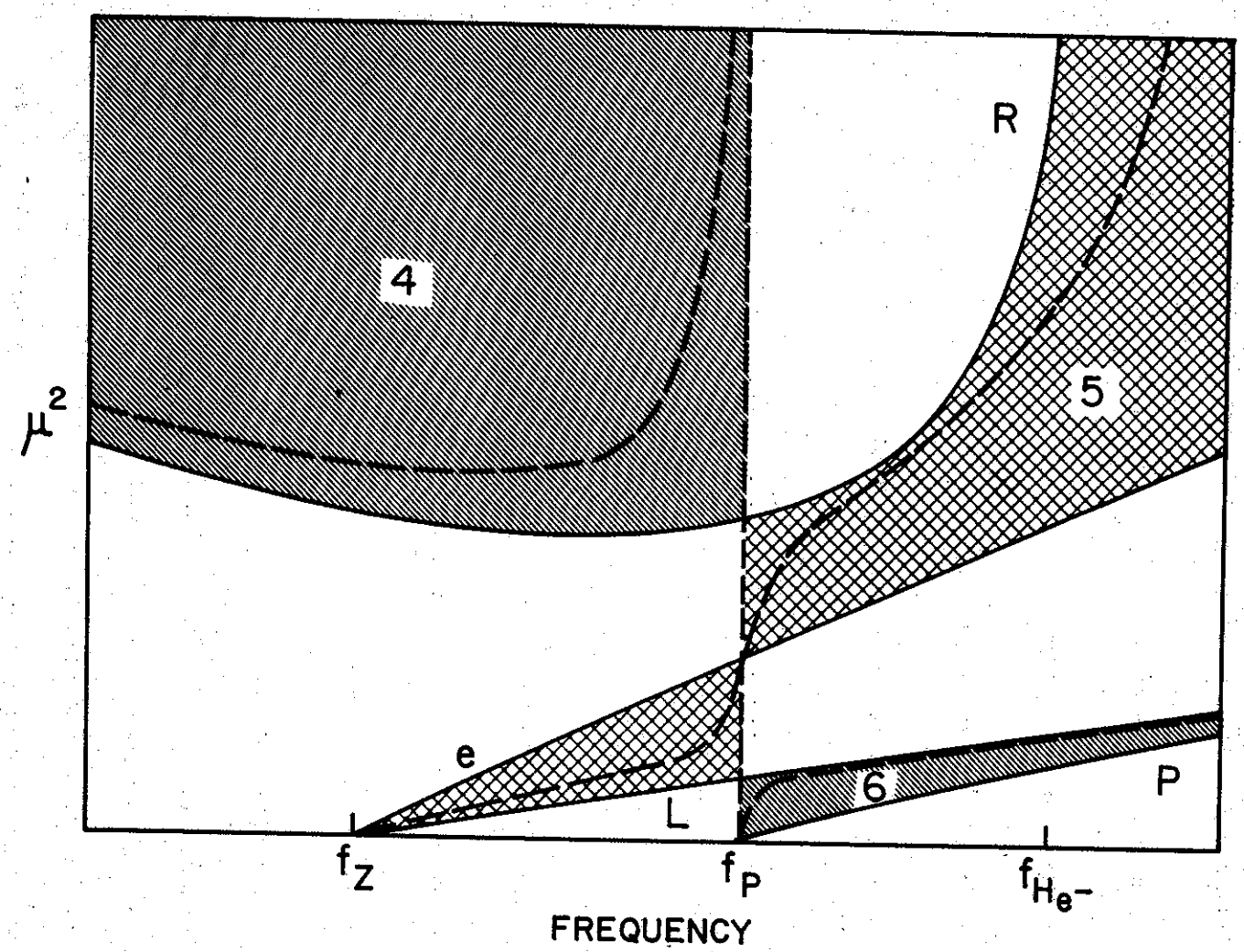

Figure 20b. The positive solutions for μ^2 are shown as a function of frequency; case that the plasma frequency is below the electron gyrofrequency (for details see text).

In this figure

$f_{H_{O^+}}$ - the O^+ gyrofrequency,

f_{R2} - the multiple-ion resonance frequency,

f_{IC1} - the multiple-ion cutoff frequency,

f_{CO1} - the cross over frequency,

$f_{H_{He^+}}$ - the He^+ gyrofrequency,

f_{R1} - the multiple-ion resonance frequency,

f_{IC2} - the multiple-ion cutoff frequency,

f_{CO2} - the cross over frequency,

$f_{H_{H^+}}$ - the H^+ gyrofrequency,

f_{LHR} - the lower hybrid resonance,

f_{He^-} - the electron gyrofrequency,

f_Z - the Z frequency,

f_p - the plasma frequency.

The letters L, R, e and P stand for particular solutions of Eq. (28). In the case where ψ is equal to 0° or 180° (wave normal parallel to the static magnetic field), Eq. (28) has two solutions (μ^2 = R, L). The solutions represent circularly polarized waves (see for example, Stix [1962]), one being right handed polarized (R) and the other one being left handed polarized (L). In the case where ψ is

equal to 90° (wave normal perpendicular to the static magnetic field) the two solutions of Eq. (28) represent waves which propagate with the electric field vector parallel to the static magnetic field ($\mu^2 = P$) or with the electric field vector perpendicular to the static magnetic field $\left(\mu^2 = \frac{RL}{S} \equiv e\right)$. These waves are commonly called plasma waves (P) since they only propagate above the plasma frequency, and extraordinary waves (e), since they are the ones arising from the anisotropy of the medium.

Here, attention is focused only into the region of propagation indicated by numbers 3 and 4 in Figure 20a-b. The shaded area indicated by number 3 is referred to as the proton whistler mode, and region 4 is called the electron whistler mode of propagation. An algorithm to find the root corresponding to the mode of propagation specified is discussed in conjunction with the description of the ray-tracing program.

From Eq. (28) the derivatives $\partial\mu/\partial j$ $(j=r,\theta)$ can be found. $\partial\mu/\partial j$ is given by

$$\frac{\partial\mu}{\partial j} = \sum_i \frac{\partial\mu}{\partial X_i}\frac{\partial X_i}{\partial j} + \sum_i \frac{\partial\mu}{\partial Y_i}\frac{\partial Y_i}{\partial j} + \frac{\partial\mu}{\partial\psi}\frac{\partial\psi}{\partial j} \qquad (43)(372)$$

Again, from Eq. (28), the following expressions may be written:

$$\frac{\partial\mu}{\partial X_i} = -\frac{\mu^4\frac{\partial A}{\partial X_i} - \mu^2\frac{\partial B}{\partial X_i} + \frac{\partial C}{\partial X_i}}{4\mu^3 A - 2\mu B} \qquad (44)(351)$$

and

$$\frac{\partial\mu}{\partial Y_i} = -\frac{\mu^4\frac{\partial A}{\partial Y_i} - \mu^2\frac{\partial B}{\partial Y_i} + \frac{\partial C}{\partial Y_i}}{4\mu^3 A - 2\mu B}, \qquad (45)(358)$$

where

$$\frac{\partial A}{\partial X_i} = \frac{1}{2}\left(\frac{\partial R}{\partial X_i} + \frac{\partial L}{\partial X_i}\right)\sin^2\psi + \frac{\partial P}{\partial X_i}\cos^2\psi \,, \qquad (46)(348)$$

$$\frac{\partial B}{\partial X_i} = \left(L\frac{\partial R}{\partial X_i} + R\frac{\partial L}{\partial X_i}\right)\sin^2\psi + \left(P\frac{\partial S}{\partial X_i} + S\frac{\partial P}{\partial X_i}\right)(1+\cos^2\psi) \qquad (47)(349)$$

$$\frac{\partial C}{\partial X_i} = PR\frac{\partial L}{\partial X_i} + RL\frac{\partial R}{\partial X_i} + RL\frac{\partial P}{\partial X_i} \,, \qquad (48)(350)$$

$$\frac{\partial R}{\partial X_i} = -\frac{1}{1 + Y_i} \,, \qquad (49)(345)$$

$$\frac{\partial L}{\partial X_i} = -\frac{1}{1 - Y_i} \,, \qquad (50)(346)$$

$$\frac{\partial P}{\partial X_i} = -1, \qquad (51)(347)$$

$$\frac{\partial A}{\partial Y_i} = \frac{\partial S}{\partial Y_i}\sin^2\psi + \frac{\partial P}{\partial Y_i}\cos^2\psi \,, \qquad (52)(355)$$

$$\frac{\partial B}{\partial Y_i} = \left(L\frac{\partial R}{\partial Y_i} + R\frac{\partial L}{\partial Y_i}\right)\sin^2\psi + \left(P\frac{\partial S}{\partial Y_i} + S\frac{\partial P}{\partial Y_i}\right)(1+\cos^2\psi) \qquad (53)(356)$$

$$\frac{\partial C}{\partial Y_i} = RL\frac{\partial P}{\partial Y_i} + P\left(L\frac{\partial R}{\partial Y_i} + R\frac{\partial L}{\partial Y_i}\right), \qquad (54)(357)$$

$$\frac{\partial R}{\partial Y_i} = X_i\frac{1}{(1 + Y_i)^2} \,, \qquad (55)(352)$$

$$\frac{\partial L}{\partial Y_i} = - X_i \frac{1}{(1 - Y_i)^2} \qquad (56)(353)$$

and

$$\frac{\partial P}{\partial Y_i} = 0 \ . \qquad (57)(354)$$

To calculate $\partial\psi/\partial j$, it is supposed that the earth's magnetic field is given by a centered dipole. Assuming also that the geomagnetic meridian plane lies in the plane $r - \theta$, $\partial\psi/\partial j$ is calculated through the expression

$$\frac{\partial\psi}{\partial j} = \frac{\partial\psi}{\partial\gamma} \frac{\partial\gamma}{\partial j} \qquad (58)(333)$$

For a centered dipole the relation between γ (the complement of the dip angle) and the co-latitude θ is given by:

$$\tan\gamma = \frac{1}{2} \tan\theta \qquad (59)$$

Therefore

$$\frac{\partial\gamma}{\partial r} = 0 \qquad (60)(332)$$

and

$$\frac{\partial\gamma}{\partial\theta} = \frac{2}{3 \cos^2\theta + 1} \qquad (61)$$

From

$$\psi = \delta - \gamma \ ,$$

is obtained

$$\frac{\partial\psi}{\partial\gamma} = - 1 \ . \qquad (62)$$

The relation that gives $\partial\mu/\partial\psi$ is derived from Eq. (28):

$$\frac{\partial\mu}{\partial\psi} = -\frac{\mu^4 \frac{\partial A}{\partial\psi} - \mu^2 \frac{\partial B}{\partial\psi} + \frac{\partial C}{\partial\psi}}{4\mu^3 A - 2\mu B} , \qquad (63)(331)$$

where

$$\frac{\partial A}{\partial\psi} = \sin 2\psi \ (S-P) , \qquad (64)(328)$$

$$\frac{\partial B}{\partial\psi} = \sin 2\psi \ (RL-PS) , \qquad (65)(329)$$

and

$$\frac{\partial C}{\partial\psi} = 0 . \qquad (66)(330)$$

To evaluate $\partial X_i/\partial j$ it is necessary to assume a model for the ionization distribution. The diffusive equilibrium model given by Angerami and Thomas [1964] is assumed here.

For this model the electron density, n_{De} is given by

$$n_{eD}(z) = n_{eb} \left(\sum_i \alpha_{ib} \, e^{-z/H_i} \right)^{1/2} \qquad (67)$$

where z is the geopotential height

$$z = r_b \left(1 - \frac{r_b}{r}\right), \qquad (68)(418)$$

r_b is the reference geocentric distance at which the electron density n_{eb}, and the ion percentage α_{ib} are specified. The scale height of

the ith ion is H_i, given by

$$H_i = \frac{kT}{m_i g_b} , \qquad (69)(414)$$

where g_b is the gravity acceleration at r_b, k is the Boltzmann constant and T is the temperature in Kelvins.

The electron and ion densities can be written as

$$n_{De}(z) = n_{eb} Q^{1/2}, \qquad (70)(431)$$

and

$$n_{Di}(z) = n_{eb} \alpha_{ib} e^{-z/H_i} Q^{-1/2} , \qquad (71)(436)$$

where

$$Q = \sum_i \alpha_{ib} e^{-z/H_i} . \qquad (72)(426)$$

Using the previous equations the following expressions may be written:

$$\frac{1}{n_{De}} \frac{\partial n_{De}}{\partial r} = \frac{1}{2Q} \frac{\partial Q}{\partial r} , \qquad (73)(432)$$

and

$$\frac{1}{n_{Di}} \frac{\partial n_{Di}}{\partial r} = - \left(\frac{1}{H_i} \frac{\partial z}{\partial r} + \frac{1}{2Q} \frac{\partial Q}{\partial r} \right) , \qquad (74)(437)$$

where

$$\frac{\partial Q}{\partial r} = - \sum_i \alpha_{ib} \frac{e^{-z/H_i}}{H_i} \qquad (75)$$

and

$$\frac{\partial z}{\partial r} = \left(\frac{r_b}{r}\right)^2 \qquad (76)(430)$$

In this model we suppose that the densities at the reference level, and scale heights are not functions of latitude, therefore

$$\frac{1}{n_{De}} \frac{\partial n_{De}}{\partial \theta} = 0 , \qquad (77)(433)$$

and

$$\frac{1}{n_{Di}} \frac{\partial n_{Di}}{\partial \theta} = 0 . \qquad (78)(438)$$

To calculate $\partial Y_i/\partial j$ $(j=r,\theta)$, it is necessary to know the electron gyrofrequency as a function of r and θ. The electron gyrofrequency for a centered dipole is given by:

$$f_{He} = f_{Heo} \left(\frac{r_E}{r}\right)^3 \left(1 + 3 \cos^2\theta\right)^{1/2} , \qquad (79)(204)$$

where

f_{He} = the electron gyrofrequency at the dipole equator ($\theta = 90^o$) and at the earth's surface, and r_E = earth radii. Therefore

$$\frac{1}{Y_i} \frac{\partial Y_i}{\partial r} = - \frac{3}{r} , \qquad (80)(207)$$

and

$$\frac{1}{Y_i} \frac{\partial Y_i}{\partial \theta} = - 3 \frac{\sin\theta \cos\theta}{(1 + 3 \cos^2\theta)} \qquad (81)(208)$$

The expressions giving $\sin\psi$ and $\cos\psi$ are

$$\sin\psi = \sin\delta\ Y_{or} - \cos\delta\ Y_{o\theta}\ , \qquad (82)(227)$$

and

$$\cos\psi = \cos\delta\ Y_{or} + \sin\delta\ Y_{o\theta}\ , \qquad (83)(228)$$

where

$$Y_{or} \equiv \frac{B_r}{B} = \frac{2\cos\theta}{(1 + 3\cos^2\theta)^{1/2}}\ , \qquad (84)(205)$$

and

$$Y_{o\theta} \equiv \frac{B_\theta}{B} = \frac{\sin\theta}{(1 + 3\cos^2\theta)^{1/2}} \qquad (85)(206)$$

The group refractive index (μ_g) is calculated using the relation

$$\mu_g = \mu + f\,\frac{\partial\mu}{\partial f}\ , \qquad (86)$$

where $\partial\mu/\partial f$ is obtained from Eq. (28):

$$\frac{\partial\mu}{\partial f} = -\frac{\mu^4\,\frac{\partial A}{\partial f} - \mu^2\,\frac{\partial B}{\partial f} + \frac{\partial C}{\partial f}}{4A\mu^3 - 2B\mu}\ , \qquad (87)(377)$$

where

$$\frac{\partial A}{\partial f} = \frac{\partial S}{\partial f}\sin^2\psi + \frac{\partial P}{\partial f}\cos^2\psi\ , \qquad (88)(374)$$

$$\frac{\partial B}{\partial f} = \left(L\,\frac{\partial R}{\partial f} + R\,\frac{\partial L}{\partial f}\right)\sin^2\psi + \left(S\,\frac{\partial P}{\partial f} + P\,\frac{\partial S}{\partial f}\right)\left(1+\cos^2\psi\right)^2 \qquad (89)(375)$$

$$\frac{\partial C}{\partial f} = RL\,\frac{\partial P}{\partial f} + PL\,\frac{\partial R}{\partial f} + PR\,\frac{\partial L}{\partial f}\ , \qquad (90)(376)$$

$$\frac{\partial S}{\partial f} = \frac{1}{2}\left(\frac{\partial R}{\partial f} + \frac{\partial L}{\partial f}\right), \tag{91}$$

$$\frac{\partial R}{\partial f} = \frac{1}{f}\sum_i X_i \frac{(2 + Y_i)}{(1 + Y_i)^2}, \tag{92}(367)$$

$$\frac{\partial L}{\partial f} = \frac{1}{f}\sum_i X_i \frac{(2 - Y_i)}{(1 - Y_i)^2}, \tag{93}(368)$$

and

$$\frac{\partial P}{\partial f} = \frac{2}{f}\sum_i X_i \tag{94}(371)$$

Now that all the equations needed to solve the differential equations, Eqs. (24) to (27), have been developed, a program for a digital computer to solve them will be described in the next section.

D. DESCRIPTION OF THE PROGRAM

The program described here is written in FORTRAN IV level H for an IBM 360/67. The program is composed of a MAIN program and four subroutines. The listing of the program is given in Appendix A.

1. Description of the MAIN Program

In the MAIN program values of the parameters to start the integration of the ray tracing differential equations are originated. Some variables which are used throughout the program are also initialized here and transfered to other subroutines through the common statement (#2). A list of some constants that appear in the MAIN program is given below:

RO - earth's radius in kilometers,

MASS - proton to electron mass ratio,

RADGRA - factor to convert angles from radians to degrees,

GRARAD - factor to convert angles from degrees to radians,

N - number of differential equations.

The parameters that are read in are described below.

The first parameters to be read in are the wave frequency (FKC), in kiloHertz, an integer that specifies the mode of propagation (MODE), and a logical parameter (OPTION) that indicates the angle given for the direction of the wave normal. The parameter MODE may assume two values which are the integer 1 for the proton whistler mode (corresponding to propagation in region 3 of Figure 20a), and the integer 2 for the electron whistler mode (region 4 in Figure 20a). There are two possible ways to specify the wave normal direction, one is to give its angle with the radial vector (OPTION = TRUE), and the other is to specify the direction with respect to the geomagnetic field (OPTION = FALSE). In Appendix B a listing is given of input cards in the sequence they are read in. (See this appendix for one example of a card with the parameters FKC, MODE and OPTION (card #1).)

The second set of parameters to be read in are the initial conditions of the starting point. These are: the height in kilometers (HEIGHT); the latitude in degrees (LAT); the angle, in degrees, between the vertical and the wave normal vector (DELTA);* and the angle, in degrees, between the wave normal and the vertical (PSI) which is only given when OPTION is FALSE. These are the parameters that constitute the second card which is shown in Appendix B (card #2).

---

*The origin of the angles and the sense in which they are measured is shown in Figure 21.

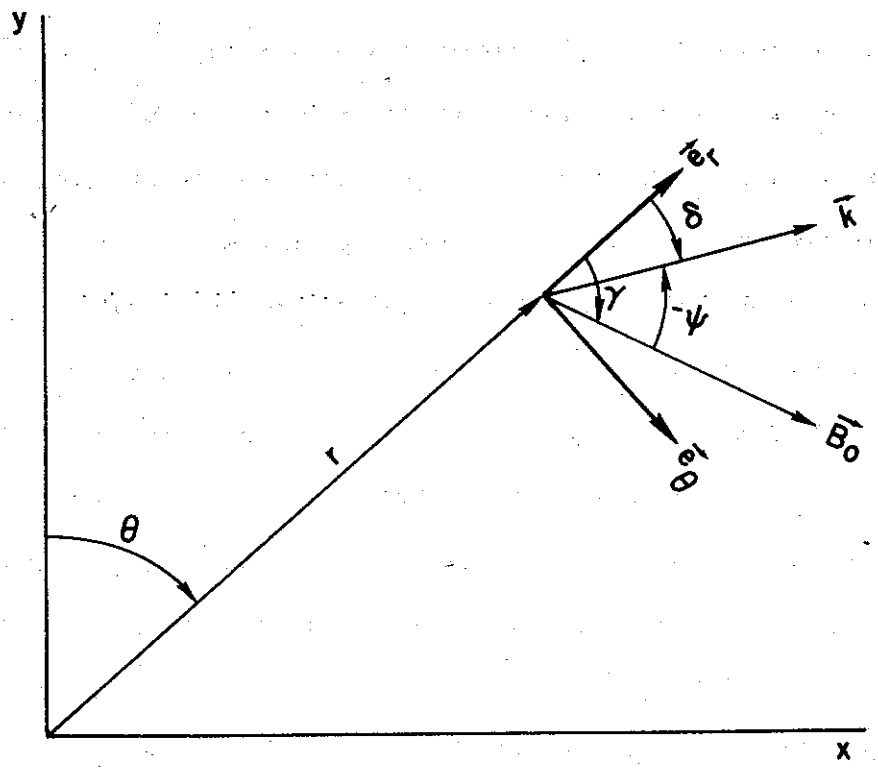

Figure 21. Origin of angles in polar coordinates is shown. The angles are positive in the clockwise direction.

The next set of parameters to be read in are the ones used in the integration procedure (subroutine ADAMS). They are: the logical parameter SKIP which indicates whether the error check in subroutine ADAMS is to be skipped (SKIP = ·TRUE·) or not; the upper bound in the absolute error (ABSB); the upper bound in the relative error (RELB); an integer (KOUNT) indicating the number of increments in the independent variable, that must be done before new results are printed out; and the initial increment of the independent variable (HM). An example of this card is shown in Appendix B (card #3). These input parameters are part of the heading of the output listing (see Appendix C).

In order for the initial increment to stay the same for every new wave frequency, when the parameters of the medium are kept the same, the parameter HM is divided by the square root of the wave frequency. It will be this parameter that will be used as the initial increment in the ADAMS subroutine and will be printed on the heading of the output listing (see Appendix C).

2. Description of the Subroutine ADAMS

This subroutine is not discussed in detail here since it was based on a procedure written in SUBALGOL for the IBM 7090 at the Stanford University Campus Facility [1965]. This procedure solves a system of N first order differential equations, using a fourth order ADAMS predictor-corrector method where the starting values are generated by a fourth order Runge-Kutta method. A discussion of this method is presented by Hildebrand [1956].

3. Description of Subroutine FUNCT

The input parameters for this subroutine are: the independent variable (T); the dependent variables which are 1) the geocentric

distance (P(1,J)), 2) the colatitude (P(2,J)), 3) the angle between the vertical and the wave normal (P(3,J)); and an integer variable (J) which identifies the step in the ADAMS subroutine in which the subroutine FUNCT was called. The output parameters (DZDT) are the first derivatives of the dependent variables with respect to the independent variable.

The equivalent electron gyrofrequency on the earth's surface, at the magnetic equator is read in this subroutine (see Appendix B--card #4).

The solution of Eq. (28) is given by the statements from #257 to #286. Now the solutions of Eq. (28) may be written in two equivalent forms:

$$\mu_1^2 = \frac{B+F}{2A} \qquad (95)(274)^*$$

and

$$\mu_2^2 = \frac{2C}{B+F} , \qquad (96)(285)$$

or

$$\mu_1^2 = \frac{B-F}{2A} \qquad (97)(268)$$

and

$$\mu_2^2 = \frac{2C}{B-F} . \qquad (98)(283)$$

The first set is preferred when B is positive. The parameter F may also be expressed in two different forms:

$$F^2 = B^2 - 4AC , \qquad (99)(257)$$

or

$$F^2 = (RL-PS)^2 \sin^4\psi + 4(PD)^2 \cos^2\psi . \qquad (100)(260)$$

---

*The second number corresponds to the left-most number on the listing of the program (Appendix A).

The first form is preferred when AC is negative. The sign of AC gives the number of the positive roots of Eq. (28) and therefore the possible number of modes of propagation. The value 1 or 2 depending on the possible number of modes of propagation will be given to a variable (#258 or #261). If it is desired this parameter may be printed out.

An algorithm was written to choose the correct solution for Eq. (28), once the mode of propagation was specified (#263 to #305). Only for the electron whistler mode (region 4 in Figure 20a-b) will this algorithm be explained.

To choose the right solution of Eq. (28) for a given mode, an algorithm was written based on the concept that two or three regions depending on whether the Z frequency is greater or smaller than the electron gyrofrequency, may be distinguished by the sign of C(=PRL) and the number of possible positive solutions. For instance focusing the attention on region 4 of Figure 20a the parameter C may be positive (in the case that the wave frequency is above the proton gyrofrequency) or negative, (in the case that the wave frequency is between the ion cutoff and proton gyrofrequency). If the wave frequency is above the proton gyrofrequency the sign of C must be positive (Figure 20a). If in any step of integration, C assumes a negative value the interval of integration given is such that (see Figure 20a), the wave frequency is above the electron gyrofrequency (R has a negative value). In the case where the wave frequency is below the proton gyrofrequency, C must assume a negative value. Therefore in the case that C is positive, a step in the integration is given such that the wave frequency is lying below the ion cutoff frequency (Figure 20a). In both cases a message is given (#303) and the program returns to the ADAMS subroutine where

the interval of integration is divided by four. It is possible that an increment in the independent variable is given in a way that A assumes a positive value, althought the wave frequency is lying between $f_{H_{H^+}}$ and f_{He^-} (C is positive). In this case Eq. (28) has two negative solutions. Therefore the angle ψ calculated in the integration process is larger than the resonance angle. Automatically a message is given calling attention to this fact (#299), and the program returns to the ADAMS subroutine where the interval of integration is divided by four.

4. Description of the Subroutine DENS

This subroutine calculates the densities of the components of the plasma based on the diffusive equilibrium model. The input parameters are the geocentric distance (R) and the colatitude (COLAT) of the point of which the densities are required. The output parameters are the electron density (ND(1)), the H^+ density (ND(2)), the He^+ density (ND(3)), the O^+ density (ND(4)), the ion composition (ALPHA(I)), and the derivatives of the logarithm of the densities of the components of the plasma with respect to the radial distance (DLNDR(I)) and with respect to the colatitude (DLNDT(I)).

The first time this subroutine is called the following parameters are read in: the height (HBASE) at which the electron density and the ion composition are specified; the electron density (NEO) and the percentage of the ions (ALPHAO(I)) at this height; the electron temperature (THERM); the number of plasma components (NUM); and an integer (IM) specifying whether helium is present in the model of ionization (see Appendix B for example). These parameters are punched on the fifth card (see Appendix B--card #5). These parameters constitute part of the heading of the output listing (see Appendix C).

5. Description of the Subroutine ESC

The output of the program is given through the subroutine ESC. To transfer parameters from the subroutine FUNCT to the subroutine ESC the common block statement /ESCF/ is used. These parameters must have a subscript J in order to be printed correctly.

Four variables are read in this subroutine corresponding to the sixth card (Appendix C--card #6). These variables are NOUT and TGEND. NOUT will specify the parameters wanted for output. When NOUT is equal to 1 the parameters that will be printed out are the ones specified by statement #467. The other possible output is the one specified by NOUT = 2 and given by statement # 489. Example of a heading when NOUT = 2 is given in Appendix C. Below is given a list of the parameters of the output followed by their meanings.

TG - group delay time in seconds,

ALT - altitude of the ray path in kilometers,

LAT - latitude of the ray path in degrees,

INV - the corresponding invariant latitude in degrees,

ELE - the $L(= r/(r_o \sin^2\theta))$ value,

GF - electron gyrofrequency in kiloHertz,

GFP - proton gyrofrequency in kiloHertz,

FLHR - LHR frequency in kiloHertz,

FCO - the ion cutoff frequency in kiloHertz,

FOE - plasma frequency in kiloHertz,

FC2 - a two ion resonance frequency in kiloHertz,

MU - phase refractive index,

BETA - the angle, in degrees, between the ray energy direction and the vertical,

DELTA - the angle, in degrees, between the vertical and the wave normal,

PSI - the angle, in degrees, between the static magnetic field and the wave normal,

PSIR - the angle, in degrees, of the resonance angle,

$\%H^+$ - percentage of the hydrogen ion.

The parameters TGEND, will specify if the ray path must continue or must stop. The program will stop if the group delay time is greater than the one specified by TGEND(3), or if the height and the colatitude of the ray path are greater than the ones specified by TGEND(1) and TGEND(2) (see statement #458). The end of the ray path is indicated in the output by a message (#495). The program then returns back to the MAIN program to check if there is a new set of cards to be read in.

E. PHYSICAL INTERPRETATION OF THE RAY-PATH BEHAVIOR

1. The PR Mode

Plotted in Figure 22a is the ray path from Appendix C. The arrows along the path indicate the wave normal direction. The phase refractive index surface for the points on the ray path are sketched in Figure 22b. To understand the behavior of this ray, Eq. (E.26) is written

$$\frac{d\psi}{dt} = \frac{c}{\mu r} \left\{ f_1 \sin\delta - \frac{3}{2} \frac{Y \cos\psi}{Y \cos\psi - 1} (f_2 \sin\delta - f_3 \cos\delta) - f_4 \sin\delta \right\} ,$$

where the functions f_1, f_2, f_3 and f_4 are given in Appendix E. This equation is obtained under the hypotheses that the wave frequency is above the LHR frequency when the wave normal is close to the resonance cone and that the Q.L. approximation holds throughout the path. The

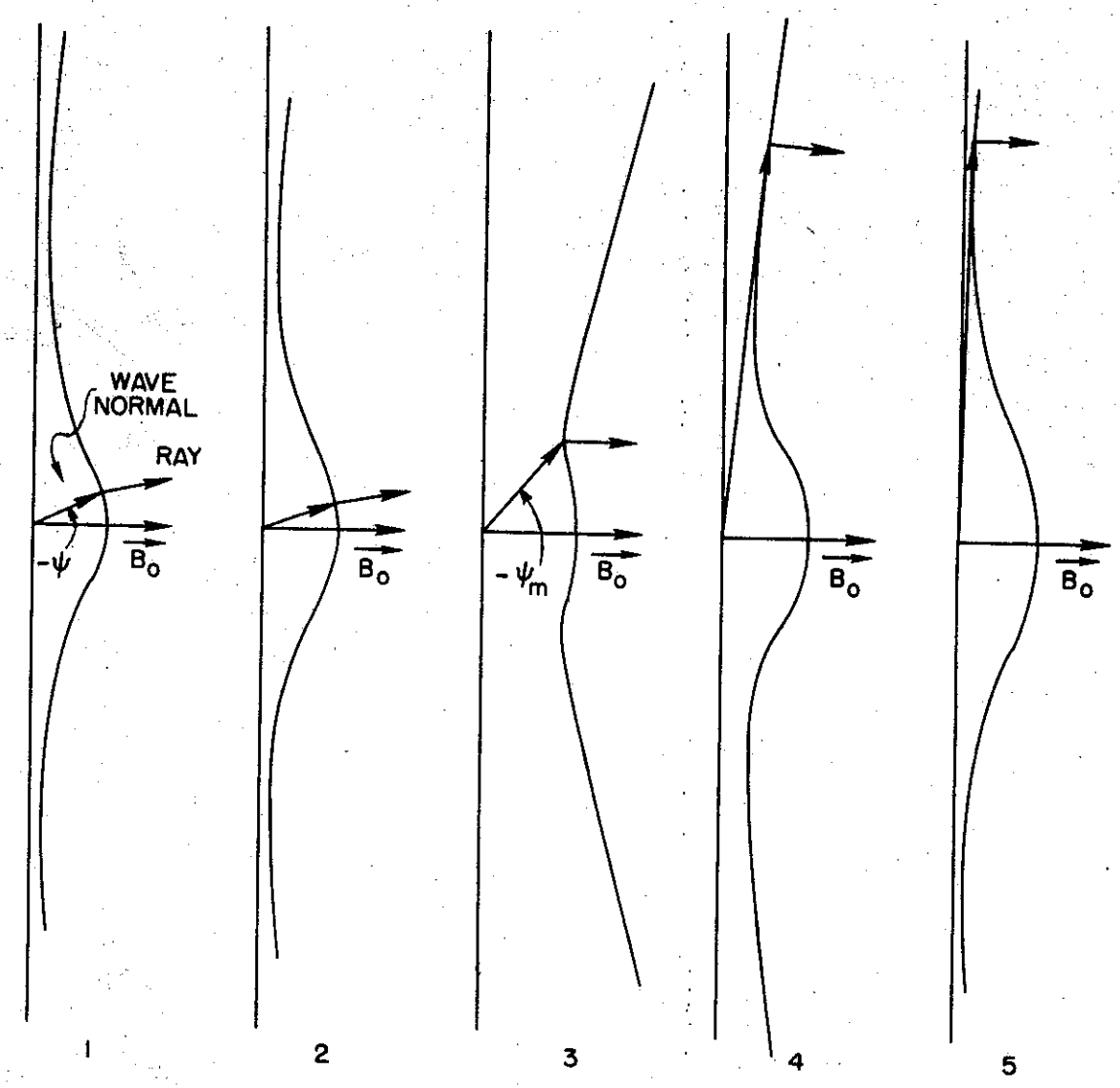

Figure 22a. Plot of ray path from results shown in Table 5. Dashed line is the dipole field line through the maximum L along the path.

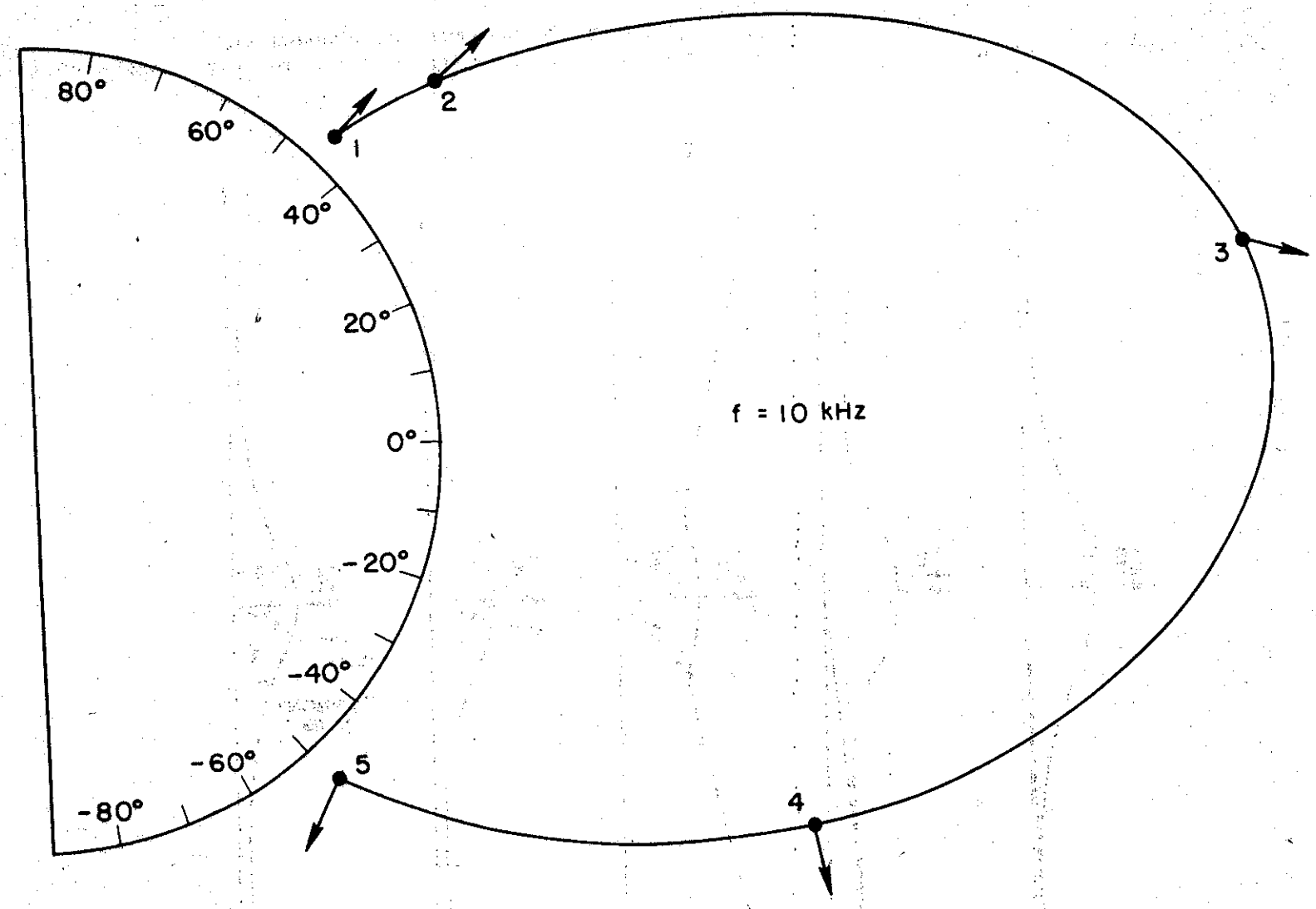

Figure 22b. Five refractive index diagrams (not to scale) indicate the wave normal and ray directions at five representative points along the ray path of Figure 6a.

ray path plotted in Figure 22a satisfies these hypotheses (see Appendix C). Therefore Eq. (E.26) may be used to analyze the ray plotted in Figure 22a.

At point 1 the wave normal is at the vertical direction ($\delta=0$) and only the term due to the horizontal component of the magnetic field gradient (f_3) is different from zero, causing the wave normal to move toward the geomagnetic field. It is noted (see Figure 21) that the angle ψ is measured from the geomagnetic field to the wave normal and is positive in the clockwise direction. Let us examine each of the terms in the equation above. The function f_1 is due to the vertical gradient of the electron density, which decreases with height (see Figure E-2). This gradient is inversely proportional to the scale height. The scale height is inversely proportional to the mean mass, which decreases with height. Therefore this function decreases with height not only because it is inversely proportional to the geocentric distance, but also because the scale height increases with height. The function f_1 (Figure E-2) was plotted for a scale height of 1000 km, which is a reasonable value for the case of hydrogen only and therefore a good assumption for heights above 2000 km. The value for f_1, from Figure E-2, is approximately 32 at 500 km where O^+ is the dominant ion and about 1.6 at 2000 km where H^+ is the predominant ion.

For small ψ the term $Y \cos\psi (Y \cos\psi - 1)^{-1}$ is approximately equal to 1. For the case of a centered dipole, the function f_2, which is proportional to the vertical component of the magnetic field gradient, is equal to 1. The function f_3 results from the vertical component of the magnetic field gradient. This function is odd (see Figure E-3) and has a maximum value equal to 0.25 at the colatitude of 63.5°. The last term (f_4) contains the variation of the geomagnetic field

direction. The function f_4 is even with a maximum equal to 3.0 at the equator. At low altitudes the function f_1 has larger values than f_4, and $f_2 \sin\delta$ is smaller than $f_3 \cos\delta$, causing the angle ψ to increase. However f_1 decreases more rapidly with height which makes ψ increase up to a point where H^+ is the predominant ion (point 2). Then the curvature of the magnetic field is the main factor governing the behavior of ψ. The angle ψ decreases toward the value ψ_m, which is given by

$$\left.\frac{\partial(\mu \cos\psi)}{\partial\psi}\right|_{\psi_m} = 0$$

At point 3 ($\psi = \psi_m$) the energy is traveling parallel to the geomagnetic field and

$$\frac{Y \cos\psi}{Y \cos\psi - 1} = 2$$

Now the term containing f_2 is of the order of the term f_4. The wave normal continues to move toward the resonance cone, causing the function $Y \cos\psi/(Y \cos\psi - 1)$ to increase. The phase refractive index also varies with $(Y \cos\psi - 1)^{-1}$ and increases very rapidly in this region as it is observed by the values found under the column MU in Appendix C. There is a positive feedback causing the angle ψ to move toward the resonance cone. Large gradients of ionization are necessary to take the wave normal from this condition. Therefore this mode of propagation will be referred to as the Pro-Resonance (PR) mode of propagation. The scale height necessary to make the angle ψ increase once this condition is reached is now calculated. For the latitude of -4.0° from Appendix C it is calculated

$$\frac{Y \cos\psi}{Y \cos\psi - 1} \cong 4.2$$

Therefore a value for f_1 greater than 10 will be necessary to make the angle ψ increase. This value of f_1 corresponds to a scale height for H^+ less than 70 km which is an unrealistic value.

After point 3 the energy moves toward lower L shells and the wave normal continues to move toward the resonance cone. Since the resonance angle is moving toward 90° the energy which is perpendicular to the phase refractive index is traveling almost parallel to the geomagnetic field (point 4). This wave eventually reaches the ionosphere (point 5) with a large phase refractive index and with wave normals almost perpendicular to the geomagnetic field since $Y \gg 1$.

2. Refractions in the Ionosphere and in the Magnetosphere

In Figure 23 a case is shown where the wave is refracted down in the ionosphere and bounces back and forth in the magnetosphere. These are the types of rays that produce the fish hook kind of spectrogram as shown in Figure 10. An enlargement of the first point of refraction is shown in Figure 24a. A sketch of the phase refractive index with the wave normal and the ray direction for the four points indicated in Figure 24a is shown in Figure 24b. The behavior of the ray in this region is understood through the sketches in Figure 24b or through the equations

$$\frac{dr}{ds} = \sin\beta$$

and

$$\frac{d\theta}{ds} = \frac{1}{r}\cos\beta$$

where β is the angle between the ray and the vertical. Only when the surface is closed (LHR frequency above wave frequency), points 2 and 3 in Figure 24, can the angle β reach values greater than 90°. The

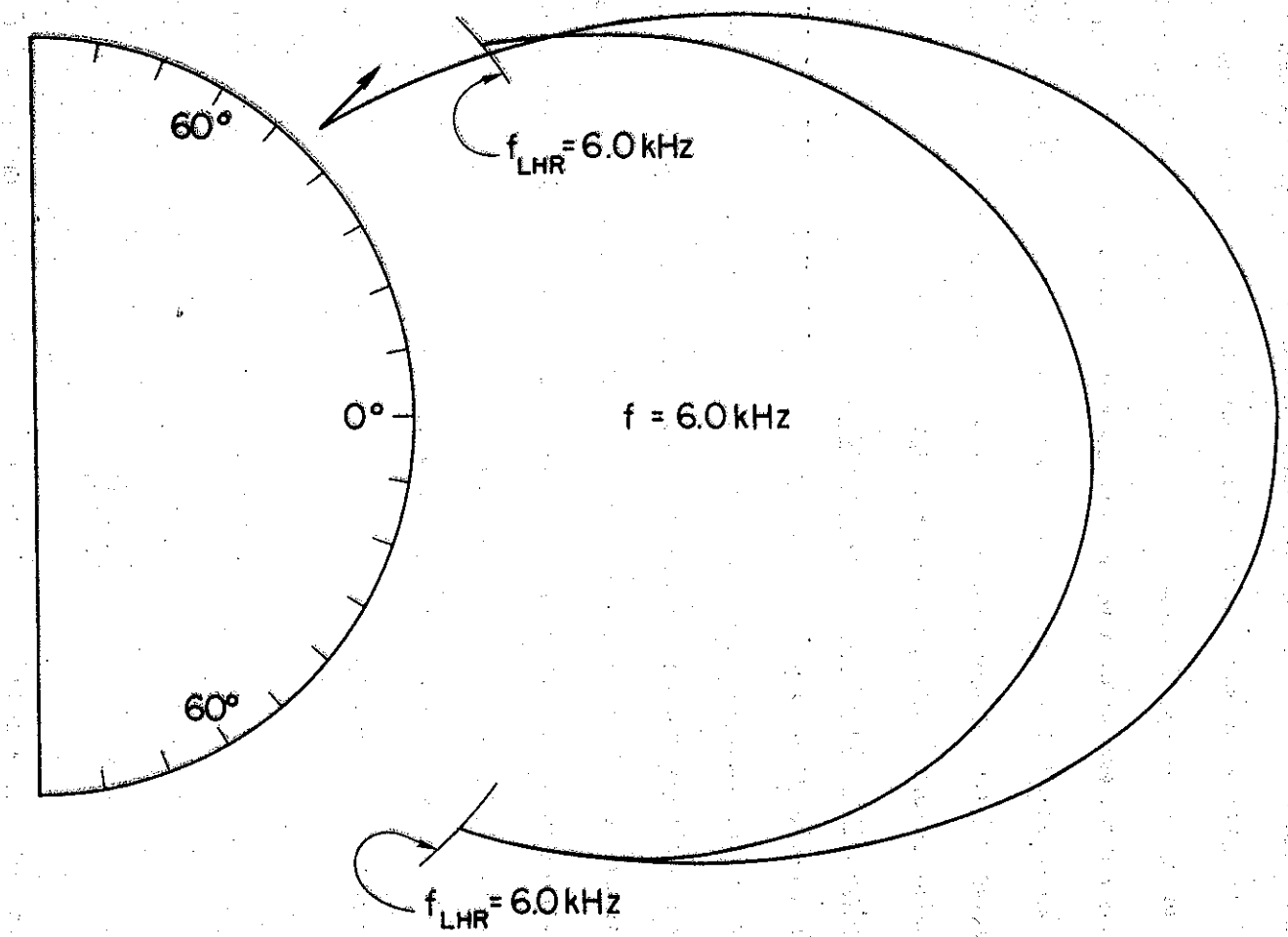

Figure 23. Ray path for a wave at 6.0 kHz is shown. The arrow indicates the wave normal at the starting point, and the thin lines indicate the locus for which the LHR frequency is equal to 6.0 kHz. Only two refractions are shown.

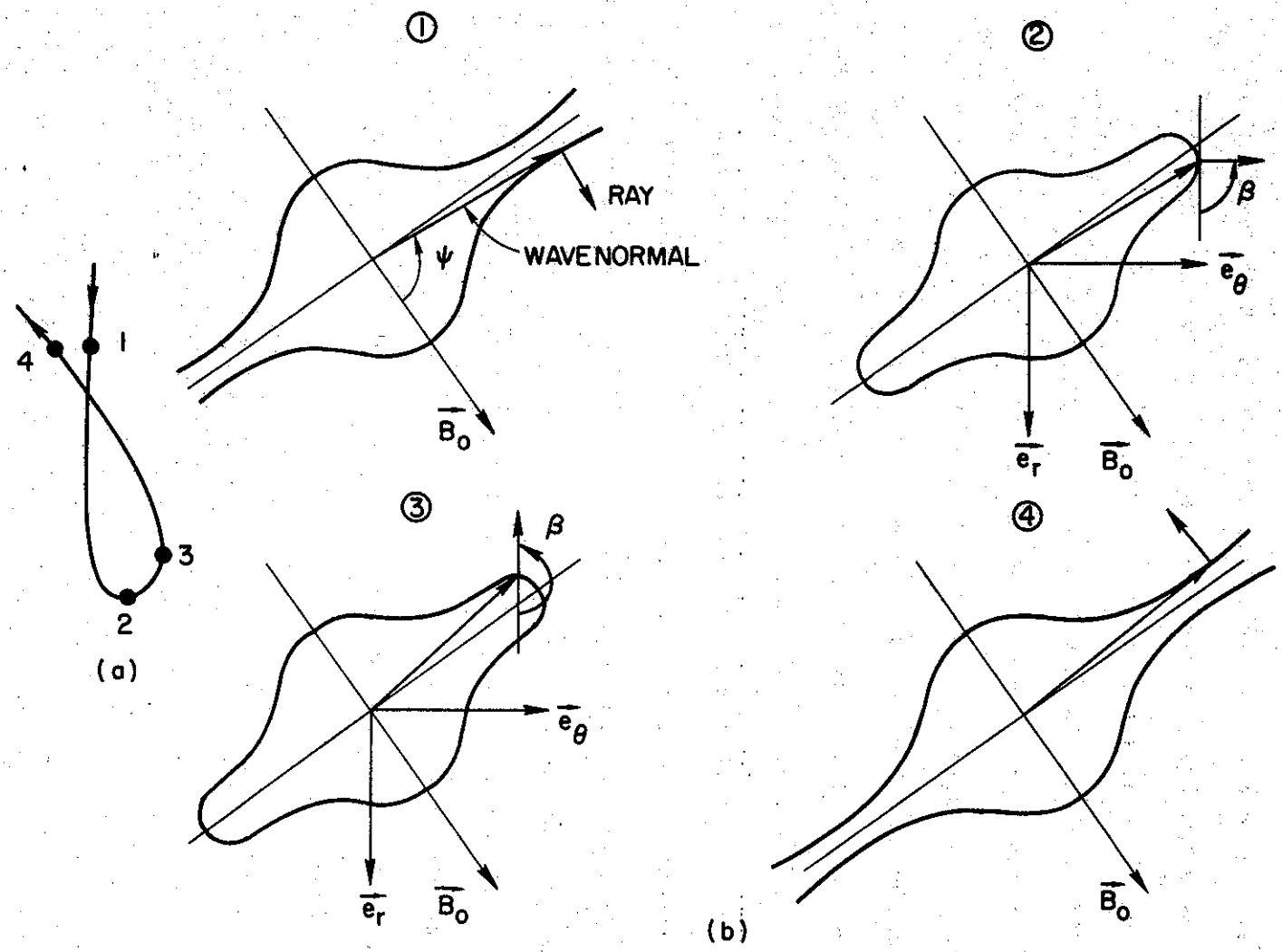

Figure 24. (a) Detail of the first refraction of the ray path of Figure 1 is shown, and (b) sketches of the phase refractive index surface for the points along the path in (a) are shown. For reference, in 2 and 3, the polar unit vectors are drawn.

energy will reach a minimum height at point 2 ($\beta = 90^{\circ}$) and from this point on will travel upward, reaching a maximum in colatitude at point 3 ($\beta = 180^{\circ}$). The ray is soon traveling in a region where the local LHR frequency is below the wave frequency and the energy will then travel toward lower L shells (point 4).

This behavior is different from the one presented by waves refracted in the magnetosphere. An example of a ray refracted in the magnetosphere is shown in Figure 25 with an enlargement of the first refraction shown in Figure 26a. The main difference in behavior is due to the fact that the wave does not travel far enough in the magnetosphere before the point is reached where the local LHR frequency is equal to the wave frequency. This causes the wave normal to be far from the resonance angle when the region is reached where the LHR frequency (point 1) is greater than the wave frequency. The wave will therefore travel further down before the point of minimum height is reached (point 2). At point 3 the ray reaches a maximum in colatitude and at point 4 the energy is moving toward higher L shells. This is the type of ray that produces the MR and the Nu whistlers [Smith and Angerami, 1968].

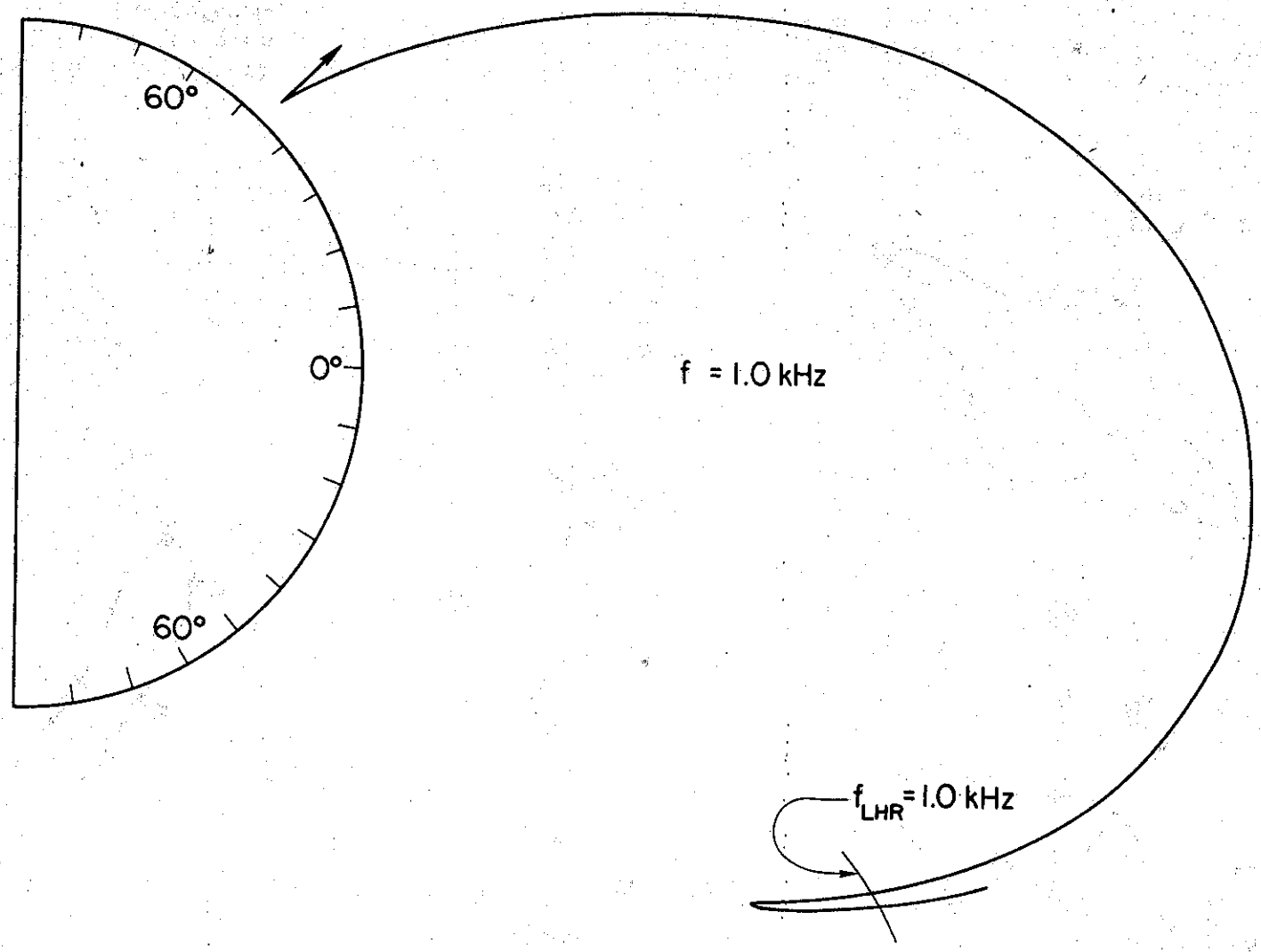

Figure 25. Ray path for wave at 1.0 kHz is shown. The arrow indicates the wave normal at the starting point. The locus for the LHR frequency equal to 1.0 kHz is indicated by the thin line. Only one refraction is shown.

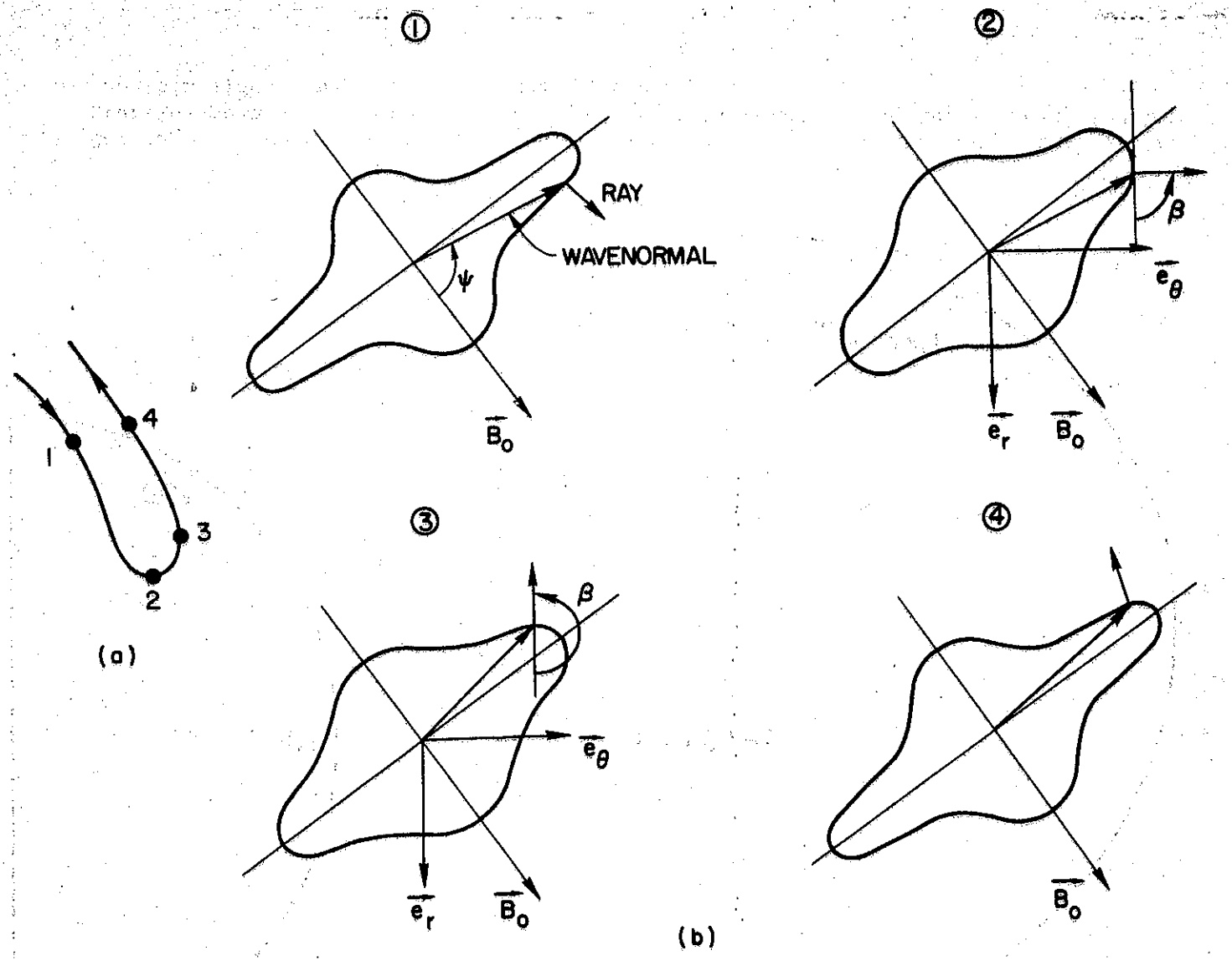

Figure 26. (a) Detail of the refraction of the ray path of Figure 25 is shown, and (b) sketches of the phase refractive index surface for the points along the path in (b) are shown. For reference, in 2 and 3, the polar unit vectors are drawn.

V. DISCUSSION AND CONCLUDING REMARKS

A. THE PRO-RESONANCE MODE

Evidence for nonducted whistler-mode propagation from one hemisphere to the conjugate ionosphere has been found in frequency-time spectra of VLF signals recorded by the broadband (0.3 - 12.5 kHz) receivers aboard the OGO-2 and OGO-4 polar satellites. The nonducted propagation manifests itself both in naturally occurring whistlers and in manmade signals.

The whistlers have been called "walking trace" (WT) whistlers because their travel times increase rapidly with latitude, producing an effect of "walking through" other whistler components that are excited by the same lightning sources but whose dispersion characteristics remain nearly unchanged with satellite position.

Many diverse characteristics of PR-mode propagation have been explained by ray tracings in a model magnetosphere represented by a dipole geomagnetic field and a diffusive-equilibrium distribution of ionization. The excellent agreement obtained provides additional support for the ray-tracing technique as a means of predicting the behavior of nonducted whistler-mode waves in the magnetosphere, and also suggests that the electron-density field-line model used (diffusive equilibrium, with about 1200 $el \cdot cm^{-3}$ at $L = 2.8$ at the equator) is a good approximation for the actual density in the plasmasphere.

The main characteristics of the PR-mode predicted by the ray tracing are given in Table 2 and are compared with the satellite observations.

B. APPLICATIONS

The diagnostic potential of the PR-mode remains to be fully evaluated. There are several promising possibilities, including use of

Table 2. COMPARISON BETWEEN RAY TRACING RESULTS AND OBSERVATIONS

PREDICTIONS OF RAYTRACING	OBSERVATIONS FROM OGO 4	COMMENTS
1) large wave normal angles, with associated phase refractive index approaching 1000	1a) Doppler shifts up to several hundred Hz near 10 kHz 1b) both positive and negative Doppler shifts, depending on equatorward or poleward motion of the satellite	
2) at a fixed frequency phase refractive index increases with latitude	2) at a fixed frequency, magnitude of Doppler shift increases with observing latitude	
3) at a fixed observing point, phase refractive index increases with frequency	3) at a fixed observing point, magnitude of Doppler shift increases with frequency	
4) for satellite below the level of the upper maximum in the LHR frequency, WT whistlers exhibit a single component with a low frequency cutoff in intensity	4) typical WT mode whistlers exhibit a single component with a lower cutoff ($f_{\ell co}$) near 7 kHz	4) the OGO-4 orbit lies between ~ 500 and 900 km altitude. The observations imply the existence of a maximum in the LHR frequency above the satellite ($f_{\ell co} \approx f_{LHR(max)}$)
5) for satellite above a maximum in the LHR frequency, WT whistlers exhibit two closely spaced components ($\Delta t \approx 70$ msec)	5) a small number of WT whistlers exhibit two closely spaced components with a lower cutoff ($f_{\ell co}$) near 6 kHz and an upper cutoff of the reflected component (f_{uco}) about 7 kHz	5) implies the absence of a maximum in the LHR above the satellite. Implies that $f_{\ell co} \approx f_{LHR(local)}$ and $f_{LHR(max\ below\ satellite)} \gtrsim f_{uco}$
6) for satellite below the upper LHR maximum, the low frequency of WT whistlers is relatively constant with latitude	6) over a typical observing range of 2-3 degrees invariant, the lower cutoff frequency is usually constant within ~ ±5%	6) implies that the upper maximum of the LHR frequency varies relatively slowly with latitude over the 2-3° observing range
7) at a fixed frequency, travel time increases with latitude	7) observed in whistlers as the "walking trace" effect, also observed in fixed frequency signals	
8) at a fixed observing point, travel time increases with frequency	8) observed in both whistlers (rising tone) and fixed frequency signals	
9) a high-frequency cutoff in intensity	9) observed in both whistlers and fixed frequency signals. In a case study the ray tracing predictions were about 1 kHz above the observed cutoffs (case of Figure 13)	9) the discrepancy is possibly due to Landau damping or to effects of detailed features of the electron density distribution
10) upper cutoff frequency decreases with latitude	10) observed in both whistlers and fixed frequency signals. Frequently causes the WT mode to disappear as the upper cutoff reaches the relatively constant lower limiting frequency	
11) a high latitude limit of observations near 55° invariant	11) WT mode observations thus far limited to latitudes < 56° invariant	
12) focusing effect (3 to 1 compression in latitude range at endpoint compared to input)	12) observed in whistlers, but particularly clearly in fixed frequency signals	
13) well defined WT-mode effects depend on a model ionosphere with relatively small horizontal gradients at 1000 km	13) well defined WT mode effects have not thus far been observed in daytime, when relatively large horizontal gradients exist in the latitude range of interest	

WT whistlers to obtain information on:

1) The plasma density and its gradient across the geomagnetic field in the magnetosphere.

2) The largest lower hybrid resonance (LHR) frequency above the satellite (from the lowest observed frequency), which in turn sets theoretical limits to ionic compositions.

WT whistlers presenting a double trace just above the lower cutoff indicate that the LHR frequency at the satellite is larger than all values above it. This condition imposes severe theoretical constraints on the rate at which the fractional abundance of H^+ can vary with altitude above the spacecraft.

Signals propagating in the PR-mode at 10.2 and 11-1/3 kHz from the U.S. Navy Omega stations have been observed in the conjugate hemisphere with amplitudes comparable to (or even larger than) those detected near the transmitter. The enhanced signals suggest the feasibility of communication between a low power VLF transmitter and a satellite in the conjugate region. For this application a better understanding of nonducted propagation is needed in order to cope with the Doppler shifts (up to hundreds of Hertz) that are normally present in the enhanced signals.

A VLF transmitter aboard a satellite may be used to determine the LHR frequency below it. Measuring the time delays, the point of refraction can be determined. Simultaneous measurement of the electron densities with the LHR frequencies will permit a determination of the profile of the effective mass below the satellite. With these data it will be possible to have an idea of the ion distribution below the spacecraft.

C. MODELS FOR THE MAGNETOSPHERE

The magnetosphere for the calculations in this report was assumed to be constituted of a plasma of electrons, H^+, He^+ and O^+ in a

diffusive equilibrium permeated by a static magnetic field represented by a centered dipole. Although as a simple model it permitted the understanding of interesting phenomena observed by VLF receivers aboard satellites. Also features of the data were predicted by tracing rays in this magnetosphere. To match the data, horizontal gradients above latitudes of $\sim 50^{\circ}$ were necessary, in agreement with measurements of electron densities with satellites around the local time of the data. Also large horizontal gradients are expected during day time which will prevent the propagation of the PR mode. This is in agreement with the survey of the data from OGO 4; an example is the data plotted in Figure 11. During the night, horizontal gradients, below a latitude of $\sim 45^{\circ}$, are expected to decrease in the direction of the equator. These gradients are in a direction to favor the propagation of the PR mode. Studies to be carried out using a hump in the electron density at 1000 km are necessary.

As it has been shown the PR mode is very sensitive to the geomagnetic field and it is expected that distortion of the magnetic field from the dipole configuration will show in the PR mode of propagation. Field lines in the vicinity of the longitude of Rosman ($\sim 97^{\circ}$W) were plotted using the Cain et al. [1968] coefficients and it has been found that the dipole lines are a good approximation for this longitude. However the same is not true in the case of longitudes near Johannesburg ($\sim 40^{\circ}$E). Therefore rays were traced in a magnetosphere where the geomagnetic field is represented by a harmonic expansion [Cain et al., 1968]. It was found that the latitude at which a given Doppler shift should be observed is about 1° lower for the dipole representation, near the longitude of Johannesburg ($\sim 41^{\circ}$E). Since the characteristics of signals propagating

in the PR mode change very rapidly with latitude a discrepancy of 1° is too large. This result confirms the prediction given in Chapter 4, Section E.

D. RAY-TRACING TECHNIQUE

Ray tracing was the essential tool used to understand the behavior of the rays that produced the PR mode of propagation. An equation that governs the variation of the angle between the wave normal and the geomagnetic field was used in order to explain the behavior of the rays that produced the PR mode. It has been found that the geomagnetic field has a preponderant role in the general behavior of the waves in the PR mode. Therefore it is expected for the same ionization distribution; however for longitudes where the geomagnetic field differs from the dipole the waves will show a different behavior than those in a dipole field. This has been tested through a ray-tracing program where a more realistic model for the geomagnetic field is used. The geomagnetic field is developed in harmonics with coefficients given by Cain et al. [1968].

The distribution of ionization given by a diffusive equilibrium model appears to be representative of the distribution presented in the magnetosphere. The use of VLF waves in the magnetosphere, with the ray tracing technique will certainly bring insight into the modeling of the magnetosphere.

One questionable problem is that related to the upper cutoff presented by the WT whistlers. Here it is proposed that this upper cutoff is caused by horizontal gradients occurring at latitudes above $\sim 45^{o}$. The MR whistlers [Smith and Angerami, 1968] show a similar

upper cutoff and Thorne [1968] proposed Landau damping as a mechanism to explain this upper cutoff. Although these waves present favorable conditions for Landau damping it is necessary to study further the propagation effects on these waves.

Influence of longitudinal gradients in the ionization was left out in this study. These gradients will certainly be important during the sunrise and sunset where large horizontal gradients are expected.

E. RECOMMENDATIONS FOR FURTHER WORK

Toward higher latitudes a descending tone whose lower cutoff generally merges with the upper cutoff of the WT whistlers is seen on occasion. This whistler has been interpreted as a consequence of the presence of large horizontal gradients and it is a kind of change from the PR mode to the PL mode of propagation.

Another problem to be explored is the one related to the upper cutoff. Apparently this upper cutoff is produced by the presence of horizontal gradients at higher latitudes which will cause the rays to change their mode of propagation. However a detailed study of this phenomena is necessary. In the case where this possibility is ruled out, the Landau damping will be the other possible mechanism. If the upper cutoff is produced by this last mechanism, measurements of energetic particles in the magnetosphere will be possible using the PR mode of propagation.

On several occasions, particularly during November 1967, artificially stimulated emissions (ASE) associated with Omega signals were observed on OGO 4. Some of the ASE's appear to be triggered by ducted signals; in this respect they are similar to those observed on the ground (see Carpenter et al. [1969]), whereas some appear to be related to nonducted

signals. The latter signals were observed both in the hemisphere conjugate to the transmitter and in the same hemisphere (in this case several echoes were also present). Study of the ASE's is possible, using ray tracings to locate possible regions of generation and corresponding wave normal directions.

The ray tracing has been shown to be a promising tool to determine the electron density distribution in the magnetosphere in conjunction with VLF data. An interesting problem not yet studied is that in connection with longitudinal gradients in the electron density. These gradients certainly will be important near the dawn-dusk meridian. This is another problem where the use of a ray-tracing program is necessary to obtain a quantitative answer.

APPENDIX A.

A listing of the two-dimensional ray tracing is given in Table 3. The leftmost number on each line is the sequential number of the statements. The number that appears at the right side of some statements corresponds to the sequential number of the corresponding equation in the text. For instance, Eq. (48) generated statement #350.

Table 3. LISTING OF THE RAY TRACING PROGRAM.

```
$WATFOR        RUN=NOCHECK,TIME=1,KP=29                                    4
C*********************************************************************C
C                              MAIN PROGRAM.                          C
C*********************************************************************C
      DIMENSION XO(10)
      COMMON RO,MASS,RADGRA,GRARAD,NUM,FKC,MODE,FIRST,IM
      COMMON /MAINF/ PSI,OPTION
      REAL MASS,LAT
      LOGICAL FIRST,SKIP,OPTION
                    RO=6372.0
                    MASS=1836.0
                    RADGRA=57.29578
                    GRARAD=1.745329E-02
    4 READ (5,1,END=500) FKC,MODE,OPTION,
     X                   HEIGHT,LAT,DELTA,PSI,
     X                   SKIP,ABSB,RELB,KOUNT,N,HM
    1 FORMAT (E6.1,I2,L5/
     X        F8.1,F8.2,F8.2,F8.2/
     X        L5,E6.1,E6.1,I3,I2,F6.2)
                WRITE (6,5) FKC,DELTA,MODE,
     X                      SKIP,ABSB,RELB
    5 FORMAT('1','   FREQUENCY=',E9.2,'KHZ        DELTA=',F7.2,
     X'      MODE ',I2,//,
     X'    SKIP=',L5,'    ABSB=',E8.1,'    RELB=',E8.1,//)
                    FIRST=.TRUE.
                    XO(1)=HEIGHT+RO
                    XO(2)=(90.00-LAT)*GRARAD
                    IF (.NOT.OPTION) PSI=PSI*GRARAD
                    XO(3)=DELTA*GRARAD
                    XO(4)=0.0
                    DELTA=DELTA*GRARAD
                    TINIT=0.0
                    H=HM/SQRT(FKC)
                    WRITE (6,3) H,KOUNT
    3 FORMAT (' ','         H=',F6.1,'      KOUNT=',I3,/)
      CALL ADAMS (N,TINIT,H,KOUNT,ABSB,RELB,SKIP,XO)
                GO TO 4
  500 RETURN
C*********************************************************************C
C                          END OF MAIN PROGRAM.                       C
C*********************************************************************C
      END
```

```
      SUBROUTINE ADAMS (N,TINIT,H,KOUNT,ABSB,RELB,SKIP,XO)
C     ADAMS PREDICTOR-CORRECTOR SUBROUTINE.
C*********************************************************************C
      DIMENSION XC(10),XP(8,5)   ,F(8,5),AK(8,5),E(8)
      COMMON RO,MASS,RADGRA,GRARAD,NUM,FKC,MODE,FIRST,IM
      COMMON /ESCA/ P(8,5)
      REAL MASS
      LOGICAL FIRST,SKIP
   70 IF (.NOT.FIRST) H=H*0.25
C*********************************************************************C
C     SET UP INITIAL VALUES.
C*********************************************************************C
      DO 90 I=1,N
      P(I,1)=XO(I)
   90 CONTINUE
      KTEMP=0
      T=TINIT
      IF (.NOT.FIRST) GO TO 140
C*********************************************************************C
C        *** WRITE THE HEADING ***                                    C
C*********************************************************************C
      CALL FUNCT(T,P,F,1,&1400)
      J=1
      CALL ESC(J,&1400)
  140 IF (.NOT.SKIP) GO TO 180
      IA=2
      IB=4
      GO TO 300
  180 RELTES =14.2*RELB
      ABSTES =14.2*ABSB
      FACTOR=RELB/ABSB
      DB=RELTES /400.0
      H=2.0*H
      GO TO 270
  240 T=TS
      H=0.5*H
      GO TO 300
  270 IA=2
      IB=2
      TS=T
C*********************************************************************C
C     RUNGE=KUTTA STARTING METHOD.
C*********************************************************************C
  300 DO 510 J=IA,IB
      CALL FUNCT(T,P,F,J-1,&70)
      DO 350 I=1,N
      AK(I,1)=H*F(I,J-1)
      P(I,J)=P(I,J-1)+0.5*AK(I,1)
  350 CONTINUE
      TTEMP=T+0.5*H
      CALL FUNCT(TTEMP,P,F,J,&70)
      DO 410 I=1,N
      AK(I,2)=H*F(I,J)
      P(I,J)=P(I,J-1)+0.5*AK(I,2)
  410 CONTINUE
      CALL FUNCT(TTEMP,P,F,J,&70)
      DO 450 I=1,N
      AK(I,3)=H*F(I,J)
      P(I,J)=P(I,J-1)+AK(I,3)
  450 CONTINUE
```

```
      T=T+H
      CALL FUNCT(T,P,F,J,&70)
      DO 510 I=1,N
      AK(I,4)=H*F(I,J)
      P(I,J)=P(I,J-1)+0.1666667*(AK(I,1)+2.0*AK(I,2)
     1+2.0*AK(I,3)+AK(I,4))
  510 CONTINUE
C*********************************************************************C
C     END RUNGE-KUTTA METHOD.
C*********************************************************************C
      IF (IB-2) 640,530,640
  530 DO 550 I=1,N
      XP(I,5)=P(I,2)
  550 CONTINUE
C*********************************************************************C
C     XP(I) ARE THE VALUES OF DOUBLE INTERVAL TO BE
C     USED IN ERROR ANALYSIS.
C*********************************************************************C
      T=T-H
      H=0.5*H
      WRITE (6,581) H
  581 FORMAT('  IN THE FOLLOWING CALCULATION H=',E15.8,/)
      IF (ABS(H).GT.1.0E-07) GO TO 620
      WRITE (6,601)
  601 FORMAT (' ','  *** EQUATIONS CAN NOT BE SOLVED FURTHER WITHIN',
     X            ' GIVEN ERROR BOUND *** ',/)
      RETURN
  620 IB=3
      GO TO 300
  640 IF (IB-3) 810,650,810
  650 J=3
      KKK=0
C*********************************************************************C
C     IS ACCURACY CRITERION MET?
C*********************************************************************C
  660 DO 760 I=3,4
      IF (KKK) 670,670,720
  670 E(I)=ABS(XP(I,5)-P(I,J))
      IF (E(I)-ABS(P(I,J))*RELTES ) 681,690,690
  681 E(I)=E(I)/ABS (P(I,J))
      GO TO 760
  690 IF (E(I)-ABSTES ) 691,700,700
  691 E(I)=E(I)*FACTOR
      GO TO 760
  700 T=T-H
      IF (J-5)530,720,530
  720 DO 740 III=1,N
      P(III,1)=P(III,4)
  740 CONTINUE
      GO TO 270
  760 CONTINUE
      IF (J-5) 780,1080,780
  780 IA=4
      IB=4
      GO TO 300
C*********************************************************************C
C     SHOULD ANY OF THE STARTING VALUES BE PRINTED OUT?
C*********************************************************************C
  810 T=T-3.0*H
      DO 921 J=2,3
```

```
      T=T+H
      KTEMP=KTEMP+1
      GO TO 910
  870 CALL ESC(J,&1400)
  900 KTEMP=0
      DO 901 IJ=1,N
      XO(IJ)=P(IJ,J)
  901 CONTINUE
      TINIT=T
  910 IF (KTEMP-KCUNT) 921,870,870
  921 CONTINUE
      T=T+H
  930 CALL FUNCT(T,P,F,4,&1310)
C*********************************************************************C
C     BEGIN ADAMS METHOD.
C     TEST WHETHER COMPUTED VALUES SHOULD BE PRINTED OUT.
C*********************************************************************C
      KTEMP=KTEMP+1
      GO TO 1200
 1160 J=4
      CALL ESC(J,&1400)
 1190 KTEMP=0
      DO 1201 IJ=1,N
      XO(IJ)=P(IJ,J)
 1201 CONTINUE
      TINIT=T
 1200 IF (KTEMP-KCUNT) 940,1160,1160
C*********************************************************************C
C     XP IS PREDICTOR VALUE.
C*********************************************************************C
  940 DO 960 I=1,N
      XP(I,5)=P(I,4)+0.04166666667*H*(55.0*F(I,4)-
     159.0*F(I,3)+37.0*F(I,2)-9.0*F(I,1))
  960 CONTINUE
      T=T+H
      CALL FUNCT(T,XP,F,5,&70)
C*********************************************************************C
C     P IS THE CORRECTOR VALUE.
C*********************************************************************C
      DO 1010 I=1,N
      P(I,5)=P(I,4)+0.0416666667*H*(9.0*F(I,5)+19.0*F(I,4)
     1-5.0*F(I,3)+F(I,2))
 1010 CONTINUE
      IF (SKIP) GO TO 1080
 1030 J=5
      GO TO 660
 1080 DO 1120 I=1,N
      P(I,4)=P(I,5)
      DO 1120 J=2,5
      F(I,J-1)=F(I,J)
 1120 CONTINUE
      IF (SKIP) GO TO 930
C*********************************************************************C
C     TEST WHETHER THE INTERVAL CAN BE DOUBLED.
C*********************************************************************C
 1220 DO 1240 I=3,4
      IF (E(I)-DB) 1240,1240,930
 1240 CONTINUE
      DO 1270 I=1,N
      P(I,1)=P(I,4)
```

```
 1270 CONTINUE
      H=4.0*H
      WRITE (6,1291) H
 1291 FORMAT('  DOUBLE H ',E15.8,/)
      GO TO 270
 1310 WRITE (6,1311)
 1311 FORMAT (' ','    *** SUSPICIOUS RETRY ***',/)
      KKK=1
      GO TO 660
 1330 T=T-H
      KKK=1
      GO TO 660
 1400 RETURN
C*********************************************************************C
C     END OF THE ADAMS SUBROUTINE.
C*********************************************************************C
      END
```

```
      SUBROUTINE FUNCT (T,P,DZDT,J,*)
C*********************************************************************C
      DIMENSION Z(8),P(8,5),DZDT(8,5),YO(2),Y(4),ALPHAO(4),ALPHA(4),
     X          DLNDR(4),DLNDT(4),DLNDP(4),ND(4),X(4),DBDZ(3),DBTDZ(3),
     X          DBPDZ(3),DGDZ(3),DBEDZ(3),DMUDZ(6),       DBRDZ(3)
      COMMON RO,MASS,RADGRA,GRARAD,NUM,FKC,MODE,FIRST,IM
      COMMON /MAINF/ PSI,OPTION
      COMMON /ESCF/ WALPHA(5),WBETA(5),WGAMA(5),WPSI(5),WPSIRE(5),
     X              WALFA(5),WFOE(5),WMU(5),WAL(5),WAP(5),WAR(5),
     X              NMODE(5),WGF(5)
      LOGICAL FIRST,OPTION
      REAL   ND,MASS,NEO,MU,ML2,MU1,MU12,MU13,MU14,MUG
          DO 100 I=1,4
             Z(I)=P(I,J)
  100     CONTINUE
      COSZ2=COS(Z(2))
      SINZ2=SIN(Z(2))
      SINZ22=SINZ2*SINZ2
      COSZ22=COSZ2*COSZ2
      IF (.NOT.FIRST) GO TO 200
      READ (5,201) GFO
  201 FORMAT (F7.2)
      WRITE (6,202) GFO
  202 FORMAT (' ', ' *** THE EARTHS MAGNETIC FIELD IS REPRESENTED BY A',
     X          ' CENTERED DIPOLE WITH A GFO=',F7.2,' KHZ ***',/)
  200 R=Z(1)
             AA=1.0/(1.0+3.0*COSZ22)
             BB=SQRT(AA)
             GF=GFO*(RO/R)**3/BB                                    079
             YO(1)=2.0*COSZ2*BB                                     084
             YO(2)=SINZ2*BB                                         085
             DBDZ(1)=-3.0/R                                         080
             DBDZ(2)=-3.0*SINZ2*COSZ2*AA                            081
             Y(1)=-GF/FKC                                           041
             Y(2)=-Y(1)/MASS                                        041
             Y(3)=0.25*Y(2)                                         041
             Y(4)=0.25*Y(3)                                         041
      CALL DENS (R,COLAT,ND,ALPHA,DLNDR,DLNDT)
             FOE=SQRT(80.7*ND(1))                                   040
             X(1)=(FOE/FKC)**2                                      039
             CONS=X(1)/MASS
             X(2)=CONS*ALPHA(2)                                     039
             X(3)=0.25*CONS*ALPHA(3)                                039
             X(4)=0.0625*CONS*ALPHA(4)                              039
          IF (.NOT.FIRST) GO TO 61
      YY=Y(3)
      IF (IM.EQ.3) YY=Y(4)
      IF (.NOT.OPTION) GO TO 6
   61 DELTA=P(3,J)
          CDELTA=COS(DELTA)
          SDELTA=SIN(DELTA)
          SPSI=SDELTA*YO(1)-CDELTA*YO(2)                            082
          CPSI=CDELTA*YO(1)+SDELTA*YO(2)                            083
          PSI=ATAN2(SPSI,CPSI)
             GO TO 7
    6     CPSI=COS(PSI)
          SPSI=SIN(PSI)
          CDELTA=YO(1)*CPSI-YO(2)*SPSI
          SDELTA=YO(2)*CPSI+YO(1)*SPSI
          P(3,J)=ATAN2(SDELTA,CDELTA)
```

```
236        7        CPSI2=CPSI*CPSI
237               SPSI2=SPSI*SPSI
238                    AR=1.0
239                    AL=1.0
240                    AP=1.0
241               DO 8 I=1,NUM
242                    AR=AR-X(I)/(1.C+Y(I))                                036
243                    AL=AL-X(I)/(1.0-Y(I))                                037
244                    AP=AP-X(I)                                           038
245        8      CONTINUE
246                    AS=0.5*(AR+AL)                                       034
247                    AD=0.5*(AR-AL)                                       035
248                    ARL=AR*AL
249                    APS=AP*AS
250                    APL=AP*AL
251                    APR=AP*AR
252                    A=AS*SPSI2+AP*CPSI2                                  030
253                    B=ARL*SPSI2+APS*(1.0+CPSI2)                          031
254                    C=AP*ARL                                             032
255                    AC=A*C
256               IF (AC) 9,9,10
257        9           F2=B*B-4.0*AC
258                    NMODE(J)=1
259               GO TC 11
260       10           F2=((ARL-APS)*SPSI2)**2+4.0*(AP*AD)**2*CPSI2
261                    NMODE(J)=2
262       11      GO TO (1001,1002),MODE
263     1001 IF (AL.GT.0.0) GO TO 12
264          IF (1.0.GT.YY.AND.1.0.LT.Y(2)) GO TO 13
265               GO TO 34
266       12 IF (1.0.LT.YY) GO TO 20
267       21 IF (A.GT.0.0) GO TO 31
268       14           MU2=(B-SQRT(F2))/(2.0*A)
269               GO TC 30
270       13 IF (A.GT.0.0) GO TO 31
271          IF (B.GT.0.0) GO TO 18
272                 GO TO 14
273       20 IF (A.LT.C.C.OR.B.LT.0.0) GO TO 17
274                    MU2=(B+SQRT(F2))/(2.0*A)
275               GO TC 30
276     1002           FZ=-0.5*GF+SQRT(GF**2+0.25*FOE**2)
277          IF (FKC.GT.FZ) GC TO 22
278          IF (AL.GT.0.0) GC TO 20
279          IF (1.0.GT.Y(2).AND.R.GT.0.0) GO TO 13
280                 GO TC 34
281       22 IF (AP.GT.0.0) GC TO 34
282                 GO TO 21
283       17           MU2=(2.0*C)/(B-SQRT(F2))
284               GO TO 30
285       18           MU2=(2.C*C)/(B+SQRT(F2))
286       30      IF (MU2) 31,32,32
287      310           WRITE (6,2000)
288     2000 FORMAT (' ',' *** THIS FREQUENCY DOES NOT PROPAGATE IN THIS MODE',
           X          ' ***',//)
289                    GO TO (1,2),MODE
290        1 GFP=Y(2)*FKC
291                    WRITE (6,2001) GFP,GF,FOE
292     2001 FORMAT(' ','   GFP=',E9.2,'KHZ   GF=',E9.2,' KHZ   FOE=',E9.2,
           X          ' KHZ',/)
293          RETURN 1
```

```
294        2          FC2=GF*(C.C625*ALPHA(2)+ALPHA(4))/MASS
295                   WRITE (6,2002) GF,FC2,FOE
296     2002 FORMAT (' ','   GF=',E9.2,' KHZ   FC2=',E9.2,' KHZ   FOE=',E9.2,
           X          ' KHZ',/)
297          RETURN 1
298       31 IF (FIRST) GO TO 310
299             WRITE (6,33)
300       33 FORMAT (' ','   *** PSI OUTSIDE RESONANCE CONE ***',/)
301          RETURN 1
302       34 IF (FIRST) GO TO 310
303                   WRITE (6,35)
304       35 FORMAT (' ',' *** IT IS NECESSARY TO DIVIDE THE INTERVAL OF INTE',
           X          'GRATION ***',/)
305          RETURN 1
306       32          MU=SQRT(MU2)
307             IF (1.0C.LT.Y(2).AND.MODE.EQ.2) GO TO 37
308             IF (MODE.EQ.1.OR.MCDE.EQ.2) GO TO 43
309             IF (FKC.LT.FCE.OR.FKC.LT.GF) GO TO 37
310       43          ARG=-AP/AS
311             IF (ARG) 37,38,38
312       37          PSIRES=1.57C7963*SIGN(1.0,PSI)
313             GO TO 39
314       38          PSIRES=ATAN(SQRT(ARG))
315                   APSI=ABS(PSI)
316                   SNPSI=PSI/APSI
317             IF (APSI-1.57C7963) 40,41,41
318       40          PSIRES=SNPSI*PSIRES
319             GO TO 39
320       41          PSIRES=SNPSI*(3.1415962-PSIRES)
321       39          MU1=MU
322                   MU12=MU1*MU1
323                   MU13=MU1*MU12
324                   MU14=MU12*MU12
325                   DENCM1=1.0/(MU12*SPSI)
326                   DENOM2=1.0/(4.0*MU13*A-2.0*MU1*B)
327                   S2PSI=2.C*SPSI*CPSI                                    064
328                   DADPSI=S2PSI*(AS-AP)                                   065
329                   DBDPSI=S2PSI*(ARL-APS)                                 066
330                   DCDPSI=0.0                                             063
331                   DMUDPS=(MU12*DBDPSI-MU14*DADPSI)*DENOM2                060
332                   DGDZ(1)=0.0                                            058
333                   DPSDZ1=C.0                                             058
334                   DPSDZ2=-2.0*AA
335                   DMUDZ(1)=0.C
336                   DMUDZ(2)=DMUDPS*DPSDZ2
337                   DARDF=0.C
338                   CALDF=C.C
339                   CAPDF=0.0
340                   DMUXZ1=C.0
341                   CMUYZ1=C.0
342                   DMUXZ2=C.0
343                   DMUYZ2=C.0
344                   DC 53 I=1,NUM
345                        DARDX=-1.C/(1.0+Y(I))                             049
346                        DALDX=-1.0/(1.0-Y(I))                             050
347                        DAPDX=-1.0                                        051
348                        DADX=0.5*(DARDX+DALDX)*SPSI2+DAPDX*CPSI2          046
349                        DBDX=(AR*DALDX+AL*DARDX)*SPSI2+(0.5*AP*(DARDX+DALDX)
           X                    +AS*DAPDX)*(1.0+CPSI2)                      047
350                        DCDX=APR*DALDX+APL*DARDX+ARL*DAPDX                048
```

```
351                     DMUDX=(-DADX*MU14+DBDX*MU12-DCDX)*DENOM2
352                     DARDY=X(I)/(1.0+Y(I))**2                                044
353                     DALDY=-X(I)/(1.0-Y(I))**2                               055
354                     DAPDY=C.0                                               056
355                     DADY=0.5*(DARDY+DALDY)*SPSI2                            057
356                     DBDY=(AR*DALDY+AL*DARDY)*SPSI2+0.5*AP*(DARDY+DALDY)*    052
      X                       (1.0+CPSI2)
357                     DCDY=APL*DARDY+APR*DALDY                                053
358                     DMUDY=(-MU14*DADY+MU12*DBDY-DCDY)*DENOM2                054
359                     DXDZ1=DLNDR(I)*X(I)                                     045
360                     DXDZ2=DLNDT(I)*X(I)
361                     DYDZ1=DBDZ(1)*Y(I)
362                     DYDZ2=DBDZ(2)*Y(I)
363                     DMUXZ1=DMUXZ1+DMUDX*DXDZ1
364                     DMUXZ2=DMUXZ2+DMUDX*DXDZ2
365                     DMUYZ1=DMUYZ1+DMUDY*DYDZ1
366                     DMUYZ2=DMUYZ2+DMUDY*DYDZ2
367                     DARDF=(2.0+Y(I))*DARDY+DARDF                            092
368                     DALDF=(Y(I)-2.0)*DALDY+DALDF                            093
369                     DAPDF=DAPDF+X(I)
370       53          CONTINUE
371                   DAPDF=2.0*DAPDF                                           094
372                   DMUDZ1=DMUDZ(1)+DMUXZ1+DMUYZ1                             043
373                   DMUDZ2=DMUDZ(2)+DMUXZ2+DMUYZ2                             043
374                   DADF=0.5*(DARDF+DALDF)*SPSI2+DAPDF*CPSI2                  088
375                   DBDF=(AL*DARDF+AR*DALDF)*SPSI2+(0.5*(AR+AL)*DAPDF
      X                     +AP*0.5*(DARDF+DALDF))*(1.0+CPSI2)                089
376                   DCDF=ARL*DAPDF+APL*DARDF+APR*DALDF                        090
377                   DMUDF=(-MU14*DADF+MU12*DBDF-DCDF)*DENOM2                  087
378                   TALPHA=-DMUDPS/MU1
C*********************************************************************C
C             DIFFERENTIAL EQUATIONS.                                       C
C*********************************************************************C
379         DZDT(1,J)=(DDELTA-SDELTA*TALPHA)/MU1                              024
380         DZDT(2,J)=(DDELTA*TALPHA+SDELTA)/(MU1*R)                          025
381         DZDT(3,J)=((DDELTA*DMUDZ2/R-SDELTA*DMUDZ1)/MU1-SDELTA/R)/MU1      026
382         DZDT(4,J)=(1.0+DMUDF/MU1)/3.0E05                                  027
C*********************************************************************C
383         WALPHA( J )=ALPHA(2)
384         WBETA( J )=ALPHA(3)
385         WGAMA( J )=ALPHA(4)
386         WPSIRE( J )=PSIRES
387         WALFA( J )=TALPHA
388         WFCE( J )=FCE
389         WGF( J )=GF
390         WMU(J)=MU
391         WAL( J )=AL
392         WAP( J )=AP
393         WAR( J )=AR
394         WPSI(J)=PSI
395             RETURN
C*********************************************************************C
396         END
```

```
397          SUBROUTINE DENS (R,COLAT,ND,ALPHA,DLNDR,DLNDT)
     C*********************************************************************C
398          DIMENSION ALPHAO(4),ALPHA(4),DLNDR(4),DLNDT(4),ND(4)
            X            ,EXNOR(4),SH(4),QI(4)
399          COMMON RO,MASS,RADGRA,GRARAD,NUM,FKC,MODE,FIRST,IM
400          REAL ND,NR,NEO,MASS
401          LOGICAL FIRST
402             IF (.NOT.FIRST) GO TO 3
403          WRITE (6,90)
404       90 FORMAT (' ',' *** THE ELECTRON AND ION DENSITY MODEL IS',
            X             ' THE DIFFUSIVE EQUILIBRIUM ONE ***',/)
405          READ (5,100) HBASE,NEO,(ALPHAO(I),I=2,4),THERM,NUM,IM
406      100 FORMAT (F7.2,E6.1,3F5.2,F6.1,I2,I2)
407          WRITE (6,200) HBASE,NEO,(ALPHAO(I),I=2,4),THERM
408      200 FORMAT (' ','    DENSITY AND % AT ',F6.1,'KM',//,
            X'    NEO=',F7.1,'    H+=',F6.2,'    HE+=',F6.2,'    O+=',F6.2,
            X'    TEMP=',F7.1,//)
409          DO 300 I=2,4
410              ALPHAO(I)=0.01*ALPHAO(I)
411      300 CONTINUE
412                  RBASE=HBASE+RO
413                  GO=9.80*(RO/RBASE)**2
414                  SH(2)=8.2542*THERM/GO                                  069
415                  SH(3)=0.25*SH(2)                                       069
416                  SH(4)=0.25*SH(3)                                       069
417        3         VZS=RBASE/R
418                  GPH=RBASE*(1.0-VZS)                                    068
419                  EXNOR(2)=EXP(-GPH/SH(2))
420                  EXNOR(3)=EXNOR(2)**4
421                  EXNOR(4)=EXNOR(3)**4
422                  Q=0.0
423                  SUMI=0.0
424              DO 1 I=2,NUM
425                  QI(I)=ALPHAO(I)*EXNOR(I)
426                  Q=Q+QI(I)                                              072
427                  SUMI=SUMI+QI(I)/SH(I)
428        1     CONTINUE
429                  NR=SQRT(Q)
430                  VZS2=VZS*VZS                                           076
431                  ND(1)=NEO*NR                                           070
432                  DLNDR(1)=-SUMI*VZS2/(2.0*Q)                            073
433                  DLNDT(1)=0.0                                           077
434              DO 2 I=2,NUM
435                  ALPHA(I)=QI(I)/Q
436                  ND(I)=ND(1)*ALPHA(I)                                   071
437                  DLNDR(I)=-DLNDR(1)-VZS2/SH(I)                          074
438                  DLNDT(I)=0.0                                           078
439        2     CONTINUE
440          RETURN
     C*********************************************************************C
441          END
```

```
      SUBROUTINE ESC(J,*)
C*********************************************************************C
      DIMENSION TGEND(5)
      COMMON RO,MASS,RADGRA,GRARAD,NUM,FKC,MODE,FIRST,IM
      COMMON /ESCA/ P(8,5)
      COMMON /ESCF/ WALPHA(5),WBETA(5),WGAMA(5),WPSI(5),WPSIRE(5),
     X              WALFA(5),WFOE(5),WMU(5),WAL(5),WAP(5),WAR(5),
     X              NMCDE(5),WGF(5)
      REAL MASS,INV
      LOGICAL FIRST,STOP
      TG=ABS(P(4,J))
      Z1=P(1,J)-RO
      Z2=90.00-P(2,J)*RADGRA
      DELTA=P(3,J)*RADGRA
      ELE=P(1,J)/(RO*SIN(P(2,J))**2)
      PSIG=WPSI(J)*RADGRA
      ALFAG= PSIG+ATAN(WALFA(J))*RADGRA
      PSIRG=WPSIRE(J)*RADGRA
      WD=2.0*WAR(J)*WAL(J)/(WAL(J)+WAR(J))
      IF (TG.GT.TGEND(3).OR.(Z1.LT.TGEND(1).AND.P(2,J).GT.TGEND(2)))
     X      STOP=.TRUE.
      IF (.NOT.FIRST) GO TO (201,202),NOUT
      FIRST=.FALSE.
      STOP=.FALSE.
      READ (5,3) NOUT,TGEND
    3 FORMAT (I2,5F6.2)
                        TGEND(2)=TGEND(2)*GRARAD
      IF (NOUT.EQ.0) NOUT=MODE
      GO TO (101,102),NOUT
  101 WRITE (6,111)
  111 FORMAT ('     TG        ALT    COLAT ELE      GFP      FCO      FC2 ',
     1'      MU',                                    '    BETA      DELTA',
     2'     PSI     PSIR     %H+ ',//)
  201 WA=WGF(J)/MASS
C*********************************************************************C
C     ***FCO AND FC2 ARE CALCULATED SUPPOSING ONLY H+ AND O+***
C*********************************************************************C
      WB=WGF(J)*(WALPHA(J)*0.0625+WGAMA(J))/MASS
      WC=WGF(J)*SQRT(WGAMA(J)+WALPHA(J)*0.0625**2)/MASS
      WE=WALPHA(J)*100.0
      WF=WAR(J)
      WRITE (6,121) P(4,J),Z1,Z2,    ELE,WA,WB,WC,WMU(J),
     X                        ALFAG,DELTA,      PSIG,PSIRG,WE
  121 FORMAT(F8.4,F9.1,F7.2,      F5.2,F8.3,F8.3,F9.3, F8.1,4F8.2
     1,F7.2)
      IF(STOP) GO TO 300
      RETURN
  102 WRITE (6,112)
  112 FORMAT ('     TG        ALT     LAT     INV  ELE     GF      FLHR     ',
     X'FOE        MU ',                                '    BETA      DELTA  ',
     X' PSI     PSIR      %H+',//)
  202 WA=WGF(J)
      SUMQ=(WALPHA(J)+WBETA(J)*0.25+WGAMA(J)*0.0625)/MASS
      WB=SQRT(SUMQ/(1.0/WFOE(J)**2+1.0/WGF(J)**2))
      WC=WFOE(J)
      WF=WAR(J)
      COSINV=SQRT(1.0/ELE)
      SININV=SQRT(1.0-COSINV*COSINV)
      INV=ATAN(SININV/COSINV)*RADGRA
      WE=WALPHA(J)*100.00
```

```
489         WRITE (6,122)      TG,Z1,Z2,INV,ELE,WA,WB,WC,WMU(J),ALFAG,DELTA,
           X                PSIG,PSIRG,WE
490     122 FORMAT (F8.4,F9.1,F7.2,F7.3,F5.2,F8.1,F6.2,F9.2,F8.1,4F8.2,F8.2)
491         IF (STOP) GO TO 300
492         RETURN
493     300 WRITE (6,302) Z1,Z2,DELTA,PSIG,PSIRG
494     302 FORMAT (' ','  HEIGHT=',E14.7,'   LAT=',E14.7,'   DELTA=',E14.7,
           X            '  PSI=',E14.7,'  PSIRES=',E14.7,/)
495         WRITE (6,303)
496     303 FORMAT (' '/,'                    *** END OF PATH. ***')
497         RETURN1
    C*********************************************************************C
498         END

    $DATA
```

APPENDIX B.

An example of input cards is shown in Table 4. The numbers printed at the top correspond to the column numbers on the card.

In card #1 the wave frequency (FKC), the mode of propagation (MODE) and the angle that will give the wave normal direction (OPTION) are specified (see text).

In this case:

FKC = 10.0 kHz (E6.1),

MODE = 2(I2), and

OPTION = TRUE (L5).

The Format is given by the field specification shown between parenthesis.

The initial conditions are punched on card #2. They are the height (HEIGHT), the latitude (LAT), the angle between the vertical and the wave normal (DELTA), and the angle between the earth's magnetic field and the wave normal (PSI), this being specified only if OPTION = FALSE.

In this case:

HEIGHT = 500.00 km (F8.1),

LAT = 45.00° (F8.2),

DELTA = 00.00° (F8.2) and

PSI = blank (F8.2).

Card #3 gives the parameters used in the ADAMS subroutine. They are:

SKIP = FALSE (L5),

ABSB = 10^{-5} (E6.1),

RELB = 10^{-5} (E6.1),

KOUNT = 1 (I3),

N = 4 (I2) and

HM = 500.0 (F6.2).

Table 4. INPUT CARDS.

```
12345678901234567890123456789012345678901234567890123456789012345678901234567890
10.0EC 2 TRUE                                                          CARD# 1
 500.00  45.0C   C0.00                                                 CARD# 2
FALSE1.0E-51.CE-5  1 4 5CC.CC                                          CARD# 3
 870.CC                                                                CARD# 4
 1CC0.C 7.5E31C.CC 0.CC9C.C03000.C 4 3                                 CARD# 5
 25CC.CC 90.CC 2.500                                                   CARD# 6
```

In this case at every step of the integration process the error check is done. The absolute and relative error bound are equal to 10^{-5}. At each step of the integration a result is printed out (KOUNT = 1). The number of equations to be integrated is equal to 4, and the initial increment of the independent variable is 500.00 (the initial increment is the phase time interval multiplied by 3.0×10^5).

Card #4 gives the value of the equivalent electron gyrofrequency in kHz, at the earth's surface and at the geomagnetic equator. For this case an equivalent electron gyrofrequency equal to 870.0 kHz was considered.

GFO = 870.00 (F7.2).

The parameters for the electron density model are given in card #5, which are:

HBASE = 1000.0 km (F7.2)

NEO = $7.5 \times 10^3 el/cm^{-3}$ (E6.1),

ALPHAO(2) = 10.00% (F5.2),

ALPHAO(3) = 00.00% (F5.2),

ALPHAO(4) = 90.00% (F5.2),

THERM = $3000.0^{o}K$ (F6.1),

NUM = 4 (I2), and

IM = 3 (I2).

Where HBASE is the height at which the electron density (NEO) and the ion composition are specified (ALPHAO(2) -%H^+, ALPHAO(3) -%He^+ and ALPHAO(4) -%O^+). When the percentage of one of the ions is equal to zero the variable IM assumes the value that specifies this ion, in this case it is the number 3, since ALPHAO(3) = 00.00.

The last card is the one read in the ESC subroutine:

NOUT = 2(I2),

TGEND(1) = 500.00 km (F6.2),

TGEND(2) = 90.00^{o} (F6.2), and

TGEND(3) = 2.50 sec (F6.2).

NOUT can assume two values, 1 or 2, which correspond to the output required. When NOUT = 2, the output is the one shown in Appendix C. The ray path will stop if the height reached is less than 500.00 (TGEND(1)) and the latitude is greater than 90.00^{o} (TGEND(2)). However in all cases where the group time delay is greater than the 2.5 sec (TGEND(3)) the ray path will stop (statement #458).

APPENDIX C.

A listing of the output is given in Table 5. The data generating this output are shown in Appendix B. In the heading of the output are printed the frequency, the angle of the vertical with the wave normal, the mode of propagation, the initial increment (=HM/SQRT(FKC)) and the number of steps that are given between the results. Also specified in this heading are the electron gyrofrequency and the parameters of the ionization model.

This output was generated specifying NOUT = 2, which is the appropriate output for the electron whistler mode of propagation.

The compilation time (3.28 sec), the execution time (8.88 sec) and the total area used are given at the end of the listing (TOTAL AREA = OBJECT + ARRAY AREA = 22656 BYTES).

Table 5. OUTPUT LISTING.

FREQUENCY= 0.10E 02KHZ DELTA= 0.00 MODE 2

SKIP= F ABSB= 0.1E-04 RELB= 0.1E-04

H= 158.1 KOUNT= 1

*** THE EARTHS MAGNETIC FIELD IS REPRESENTED BY A CENTERED DIPOLE WITH A GFO= 870.00 KHZ ***

*** THE ELECTRON AND ION DENSITY MODEL IS THE DIFFUSIVE EQUILIBRIUM ONE ***

DENSITY AND % AT 1000.0KM

NEO= 7500.0 H+= 10.00 HE+= 0.00 O+= 90.00 TEMP= 3000.0

TG	ALT	LAT	INV	ELE	GF	FLHR	FOE	MU	BETA	DELTA	PSI	PSIR	%H+
0.0000	500.0	45.00	47.086	2.16	1096.6	5.46	1432.65	14.5	-12.39	0.00	-26.57	-89.45	1.02
IN THE FOLLOWING CALCULATION H= 0.15811380E 03													
0.0003	510.9	44.98	47.107	2.16	1091.2	5.43	1411.73	14.4	-12.38	0.05	-26.54	-89.44	1.08
0.0005	522.0	44.95	47.128	2.16	1085.7	5.40	1390.94	14.2	-12.36	0.09	-26.51	-89.44	1.14
0.0008	533.2	44.93	47.150	2.16	1080.1	5.38	1370.30	14.0	-12.35	0.14	-26.48	-89.43	1.20
0.0011	544.5	44.91	47.171	2.16	1074.5	5.35	1349.78	13.8	-12.34	0.19	-26.45	-89.42	1.27
0.0013	556.0	44.88	47.193	2.17	1068.9	5.33	1329.41	13.7	-12.32	0.24	-26.42	-89.42	1.35
0.0016	567.6	44.86	47.214	2.17	1063.3	5.31	1309.17	13.5	-12.31	0.29	-26.39	-89.41	1.43
0.0019	579.4	44.83	47.236	2.17	1057.6	5.28	1289.07	13.3	-12.30	0.35	-26.35	-89.41	1.51
DOUBLE H 0.63245550E 03													
IN THE FOLLOWING CALCULATION H= 0.31622770E 03													
0.0027	615.6	44.76	47.304	2.17	1040.4	5.22	1229.66	12.8	-12.25	0.51	-26.25	-89.38	1.81
0.0032	640.6	44.70	47.349	2.18	1028.8	5.19	1190.77	12.5	-12.22	0.63	-26.18	-89.37	2.04
0.0038	666.2	44.65	47.396	2.18	1017.0	5.16	1152.50	12.1	-12.18	0.75	-26.10	-89.36	2.30
DOUBLE H 0.12649110E 04													
IN THE FOLLOWING CALCULATION H= 0.63245550E 03													
0.0054	747.3	44.47	47.540	2.19	980.9	5.11	1041.46	11.2	-12.07	1.15	-25.84	-89.31	3.36
0.0065	805.2	44.35	47.641	2.20	956.0	5.11	970.81	10.5	-11.98	1.45	-25.64	-89.28	4.38
0.0076	866.6	44.22	47.745	2.21	930.6	5.16	903.09	9.9	-11.89	1.78	-25.42	-89.24	5.73
0.0086	931.6	44.08	47.853	2.22	904.6	5.24	838.54	9.4	-11.78	2.14	-25.17	-89.21	7.56
0.0097	1000.6	43.93	47.965	2.23	878.0	5.37	777.49	8.8	-11.66	2.53	-24.90	-89.17	10.02
0.0108	1073.8	43.76	48.080	2.24	850.9	5.55	720.30	8.3	-11.53	2.96	-24.61	-89.13	13.32
0.0119	1151.5	43.59	48.199	2.25	823.3	5.78	667.43	7.8	-11.40	3.42	-24.29	-89.10	17.67
0.0130	1233.7	43.41	48.321	2.26	795.3	6.04	619.37	7.3	-11.25	3.91	-23.95	-89.07	23.28
0.0141	1320.5	43.21	48.446	2.27	767.1	6.33	576.61	7.0	-11.09	4.42	-23.60	-89.04	30.26
0.0152	1411.7	43.00	48.572	2.28	738.7	6.62	539.56	6.6	-10.94	4.94	-23.26	-89.01	38.52
0.0163	1506.9	42.79	48.700	2.30	710.6	6.89	508.40	6.4	-10.80	5.45	-22.93	-89.00	47.66
0.0175	1605.4	42.56	48.828	2.31	682.9	7.11	482.98	6.2	-10.67	5.93	-22.65	-88.98	57.06
0.0186	1706.5	42.32	48.955	2.32	655.9	7.28	462.84	6.0	-10.56	6.36	-22.41	-88.96	65.97
0.0197	1809.3	42.08	49.081	2.33	629.8	7.39	447.20	5.9	-10.48	6.75	-22.22	-88.94	73.83
0.0208	1913.0	41.84	49.204	2.34	604.8	7.44	435.21	5.9	-10.41	7.09	-22.09	-88.92	80.31
0.0220	2016.9	41.59	49.323	2.35	581.0	7.45	426.00	5.9	-10.37	7.38	-22.01	-88.89	85.40
0.0231	2120.7	41.35	49.440	2.37	558.4	7.42	418.87	5.9	-10.34	7.64	-21.97	-88.85	89.26
0.0242	2223.7	41.11	49.553	2.38	537.1	7.36	413.24	5.9	-10.33	7.86	-21.95	-88.82	92.11
0.0254	2325.5	40.87	49.663	2.39	517.0	7.28	408.68	6.0	-10.32	8.06	-21.96	-88.77	94.20
0.0265	2427.0	40.63	49.770	2.40	498.0	7.18	404.90	6.0	-10.33	8.24	-21.99	-88.73	95.71

0.0277	2527.0	40.39	49.873	2.41	480.1	7.08	401.68	6.1	-10.33	8.40	-22.04	-88.69	96.81
0.0288	2625.7	40.16	49.973	2.42	463.3	6.97	398.87	6.2	-10.35	8.56	-22.09	-88.64	97.61
0.0299	2723.2	39.93	50.070	2.43	447.3	6.86	396.37	6.2	-10.36	8.70	-22.15	-88.60	98.20
0.0311	2819.4	39.70	50.164	2.44	432.3	6.75	394.11	6.3	-10.38	8.84	-22.22	-88.55	98.63
0.0322	2914.3	39.48	50.256	2.45	418.1	6.64	392.04	6.4	-10.40	8.96	-22.29	-88.50	98.95
0.0333	3008.1	39.26	50.345	2.46	404.7	6.53	390.11	6.5	-10.43	9.09	-22.37	-88.45	99.19
0.0344	3100.6	39.04	50.431	2.46	391.9	6.42	388.31	6.6	-10.45	9.20	-22.45	-88.41	99.37
0.0356	3191.9	38.83	50.515	2.47	379.8	6.31	386.61	6.6	-10.47	9.32	-22.53	-88.36	99.50
0.0367	3282.0	38.62	50.597	2.48	368.4	6.20	385.00	6.7	-10.50	9.43	-22.62	-88.31	99.61
0.0378	3371.0	38.41	50.676	2.49	357.5	6.09	383.46	6.8	-10.52	9.53	-22.71	-88.26	99.69
0.0390	3458.8	38.20	50.754	2.50	347.2	5.99	381.99	6.9	-10.55	9.63	-22.80	-88.21	99.75

DOUBLE H 0.25298220E 04

IN THE FOLLOWING CALCULATION H= 0.12649110E 04

0.0424	3716.0	37.60	50.975	2.52	319.0	5.69	377.92	7.1	-10.63	9.92	-23.07	-88.07	99.86
0.0446	3882.3	37.21	51.113	2.54	302.3	5.49	375.44	7.3	-10.68	10.10	-23.26	-87.97	99.91
0.0469	4044.8	36.83	51.245	2.55	287.1	5.31	373.13	7.4	-10.74	10.27	-23.45	-87.87	99.94
0.0492	4203.6	36.46	51.372	2.57	273.1	5.13	370.96	7.6	-10.79	10.44	-23.65	-87.76	99.96
0.0514	4359.0	36.10	51.493	2.58	260.3	4.96	368.91	7.7	-10.85	10.59	-23.84	-87.66	99.97
0.0537	4510.9	35.75	51.609	2.59	248.4	4.80	366.98	7.9	-10.90	10.75	-24.04	-87.56	99.98
0.0560	4659.7	35.40	51.720	2.61	237.5	4.65	365.15	8.1	-10.95	10.89	-24.24	-87.45	99.98
0.0582	4805.4	35.06	51.827	2.62	227.4	4.50	363.42	8.2	-11.00	11.03	-24.44	-87.34	99.99

DOUBLE H 0.50596440E 04

IN THE FOLLOWING CALCULATION H= 0.25298220E 04

0.0651	5225.4	34.08	52.125	2.65	201.1	4.09	358.72	8.7	-11.15	11.43	-25.04	-87.02	99.99
0.0696	5492.2	33.46	52.307	2.67	186.4	3.85	355.93	9.0	-11.24	11.68	-25.44	-86.80	100.00
0.0742	5749.4	32.85	52.476	2.70	173.4	3.63	353.38	9.3	-11.32	11.91	-25.84	-86.57	100.00
0.0788	5997.5	32.27	52.635	2.72	162.0	3.43	351.04	9.6	-11.40	12.14	-26.24	-86.34	100.00
0.0835	6237.3	31.70	52.785	2.73	151.8	3.25	348.88	9.9	-11.48	12.36	-26.63	-86.10	100.00
0.0881	6469.2	31.15	52.926	2.75	142.7	3.08	346.88	10.2	-11.54	12.57	-27.03	-85.87	100.00
0.0928	6693.7	30.62	53.059	2.77	134.6	2.93	345.02	10.4	-11.60	12.77	-27.42	-85.63	100.00
0.0975	6911.2	30.10	53.185	2.78	127.2	2.78	343.28	10.7	-11.66	12.97	-27.82	-85.38	100.00
0.1022	7122.2	29.59	53.304	2.80	120.5	2.65	341.66	11.0	-11.70	13.16	-28.21	-85.13	100.00
0.1069	7326.9	29.09	53.417	2.82	114.5	2.53	340.15	11.3	-11.74	13.35	-28.60	-84.88	100.00
0.1116	7525.7	28.60	53.525	2.83	108.9	2.42	338.72	11.6	-11.78	13.53	-28.98	-84.63	100.00

DOUBLE H 0.10119280E 05

IN THE FOLLOWING CALCULATION H= 0.50596440E 04

0.1261	8089.3	27.21	53.818	2.87	94.9	2.13	334.93	12.5	-11.83	14.07	-30.14	-83.86	100.00
0.1358	8440.0	26.32	53.991	2.89	87.3	1.97	332.73	13.1	-11.83	14.41	-30.90	-83.34	100.00
0.1457	8772.7	25.46	54.150	2.92	80.8	1.83	330.76	13.7	-11.80	14.75	-31.65	-82.81	100.00
0.1558	9088.6	24.62	54.296	2.94	75.1	1.71	328.97	14.3	-11.74	15.08	-32.41	-82.27	100.00
0.1659	9388.9	23.81	54.430	2.96	70.2	1.60	327.34	14.8	-11.65	15.41	-33.15	-81.73	100.00
0.1762	9674.6	23.02	54.553	2.97	65.8	1.51	325.86	15.4	-11.52	15.74	-33.90	-81.18	100.00
0.1867	9946.6	22.25	54.666	2.99	61.9	1.42	324.50	16.1	-11.36	16.06	-34.65	-80.64	100.00
0.1974	10205.6	21.50	54.770	3.01	58.5	1.34	323.26	16.7	-11.17	16.38	-35.39	-80.09	100.00
0.2082	10452.3	20.75	54.867	3.02	55.5	1.28	322.11	17.3	-10.94	16.71	-36.13	-79.55	100.00
0.2192	10687.2	20.02	54.955	3.03	52.7	1.21	321.05	17.9	-10.67	17.03	-36.88	-79.00	100.00
0.2304	10910.9	19.31	55.037	3.05	50.2	1.16	320.08	18.6	-10.36	17.36	-37.62	-78.46	100.00

DOUBLE H 0.20238570E 05

IN THE FOLLOWING CALCULATION H= 0.10119280E 05

0.2654	11518.9	17.20	55.242	3.08	44.2	1.02	317.56	20.6	-9.20	18.36	-39.88	-76.86	100.00
0.2899	11874.7	15.83	55.351	3.09	41.0	0.95	316.17	22.0	-8.21	19.05	-41.41	-75.82	100.00
0.3156	12193.2	14.46	55.439	3.11	38.3	0.89	314.98	23.5	-7.04	19.76	-42.96	-74.83	100.00

0.3426	12475.6	13.11	55.508	3.12	36.1	0.84	313.96	25.0	-5.68	20.49	-44.54	-73.88	100.00
0.3710	12722.4	11.75	55.558	3.13	34.3	0.80	313.10	26.7	-4.15	21.26	-46.15	-73.00	100.00
0.4012	12933.9	10.37	55.590	3.13	32.8	0.76	312.38	28.5	-2.44	22.07	-47.82	-72.19	100.00
0.4332	13109.3	8.98	55.604	3.13	31.5	0.73	311.79	30.5	-0.59	22.93	-49.53	-71.47	100.00
0.4675	13247.5	7.55	55.601	3.13	30.6	0.71	311.34	32.7	1.39	23.85	-51.31	-70.86	100.00
0.5044	13346.3	6.07	55.578	3.13	29.8	0.69	311.02	35.0	3.44	24.83	-53.17	-70.39	100.00
0.5444	13402.4	4.52	55.536	3.12	29.4	0.68	310.84	37.7	5.50	25.89	-55.11	-70.06	100.00
0.5883	13410.9	2.90	55.472	3.11	29.2	0.68	310.81	40.8	7.49	27.05	-57.16	-69.92	100.00
0.6369	13364.8	1.16	55.383	3.10	29.3	0.68	310.96	44.3	9.33	28.34	-59.35	-70.00	100.00
0.6914	13253.0	-0.74	55.266	3.08	29.8	0.69	311.32	48.6	10.91	29.78	-61.69	-70.34	100.00
0.7539	13058.6	-2.84	55.113	3.06	30.8	0.72	311.96	53.7	12.12	31.44	-64.23	-71.01	100.00

IN THE FOLLOWING CALCULATION H= 0.50596440E 04

0.7889	12922.4	-4.00	55.021	3.04	31.6	0.73	312.42	56.8	12.54	32.37	-65.60	-71.49	100.00
0.8271	12753.4	-5.26	54.916	3.03	32.6	0.76	312.99	60.4	12.81	33.38	-67.04	-72.08	100.00
0.8693	12544.3	-6.63	54.795	3.01	33.9	0.79	313.72	64.5	12.91	34.51	-68.58	-72.81	100.00
0.9163	12284.6	-8.15	54.654	2.99	35.7	0.83	314.65	69.5	12.82	35.77	-70.22	-73.68	100.00
0.9697	11958.1	-9.89	54.490	2.96	38.1	0.88	315.86	75.6	12.49	37.21	-72.01	-74.75	100.00

IN THE FOLLOWING CALCULATION H= 0.25298220E 04

0.9995	11762.4	-10.85	54.397	2.95	39.7	0.92	316.60	79.2	12.23	38.01	-72.97	-75.36	100.00
1.0317	11539.0	-11.91	54.294	2.94	41.6	0.96	317.48	83.4	11.88	38.89	-73.97	-76.04	100.00
1.0670	11281.4	-13.07	54.180	2.92	43.9	1.02	318.52	88.3	11.45	39.86	-75.04	-76.79	100.00
1.1061	10980.3	-14.37	54.053	2.90	46.9	1.08	319.78	94.0	10.91	40.94	-76.18	-77.63	100.00
1.1499	10621.9	-15.84	53.909	2.88	50.7	1.17	321.35	101.1	10.26	42.17	-77.41	-78.57	100.00
1.2002	10184.4	-17.57	53.742	2.86	56.0	1.29	323.36	110.1	9.46	43.61	-78.74	-79.64	100.00

IN THE FOLLOWING CALCULATION H= 0.12649110E 04

1.2284	9925.2	-18.57	53.648	2.85	59.4	1.36	324.61	115.6	8.99	44.43	-79.46	-80.24	100.00
1.2593	9630.0	-19.67	53.544	2.83	63.6	1.46	326.09	122.1	8.47	45.33	-80.23	-80.88	100.00
1.2937	9288.2	-20.92	53.429	2.82	68.9	1.57	327.88	129.9	7.88	46.36	-81.05	-81.58	100.00
1.3324	8883.7	-22.37	53.299	2.80	75.9	1.73	330.12	139.6	7.22	47.53	-81.93	-82.35	100.00
1.3771	8390.0	-24.10	53.149	2.78	85.7	1.94	333.04	152.3	6.47	48.92	-82.89	-83.21	100.00

IN THE FOLLOWING CALCULATION H= 0.63245550E 03

1.4025	8096.2	-25.11	53.064	2.77	92.2	2.08	334.88	160.3	6.04	49.73	-83.41	-83.69	100.00
1.4366	7759.0	-26.26	52.970	2.76	100.5	2.25	337.11	170.0	5.58	50.64	-83.97	-84.19	100.00
1.4623	7363.7	-27.58	52.865	2.74	111.3	2.47	339.88	182.0	5.07	51.69	-84.57	-84.75	100.00
1.4989	6886.3	-29.17	52.745	2.73	126.4	2.77	343.48	197.8	4.51	52.93	-85.22	-85.35	100.00
1.5427	6283.9	-31.14	52.604	2.71	149.1	3.20	348.47	219.9	3.87	54.45	-85.94	-86.04	100.00

IN THE FOLLOWING CALCULATION H= 0.31622770E 03

IN THE FOLLOWING CALCULATION H= 0.15811380E 03

1.5554	6104.3	-31.72	52.564	2.71	156.8	3.34	350.06	226.9	3.69	54.90	-86.14	-86.22	100.00
1.5690	5909.4	-32.36	52.522	2.70	165.7	3.50	351.86	234.7	3.50	55.38	-86.34	-86.42	100.00
1.5836	5696.2	-33.05	52.476	2.70	176.2	3.68	353.90	243.7	3.31	55.90	-86.55	-86.62	100.00
1.5996	5460.9	-33.81	52.428	2.69	188.7	3.89	356.25	254.0	3.11	56.48	-86.77	-86.83	100.00
1.6172	5198.3	-34.65	52.376	2.68	204.0	4.14	359.01	266.1	2.89	57.11	-87.01	-87.06	99.99
1.6368	4900.7	-35.61	52.318	2.68	223.2	4.43	362.32	280.9	2.66	57.82	-87.25	-87.30	99.99
1.6594	4557.2	-36.71	52.255	2.67	248.2	4.79	366.41	299.5	2.41	58.64	-87.52	-87.55	99.98
1.6860	4150.1	-38.01	52.184	2.66	282.5	5.25	371.68	323.7	2.14	59.59	-87.80	-87.83	99.95

IN THE FOLLOWING CALCULATION H= 0.79056940E 02

1.7018	3912.7	-38.77	52.144	2.66	305.2	5.52	375.00	338.4	1.99	60.14	-87.96	-87.98	99.91
1.7196	3646.0	-39.63	52.101	2.65	333.6	5.84	378.99	356.5	1.84	60.75	-88.12	-88.14	99.84
1.7404	3341.1	-40.61	52.054	2.64	370.1	6.21	383.97	378.3	1.67	61.45	-88.30	-88.31	99.66
1.7655	2985.3	-41.75	52.002	2.64	419.4	6.64	390.57	406.6	1.49	62.25	-88.49	-88.50	99.13

IN THE FOLLOWING CALCULATION H= 0.39528470E 02

```
1.7804   2781.1 -42.41 51.973 2.64   451.4  6.89   394.99   423.7   1.39   62.71  -88.59  -88.60   98.47
1.7974   2555.4 -43.14 51.942 2.63   490.4  7.14   400.84   444.5   1.28   63.22  -88.70  -88.71   97.07
1.8172   2303.6 -43.96 51.909 2.63   539.1  7.39   409.60   468.7   1.18   63.78  -88.81  -88.82   93.79
IN THE FOLLOWING CALCULATION H= C.19764230E 02

1.8281   2167.3 -44.40 51.892 2.63   568.0  7.48   416.17   481.9   1.12   64.09  -88.86  -88.87   90.66
1.8396   2024.8 -44.87 51.874 2.62   600.3  7.54   425.40   498.8   1.08   64.42  -88.91  -88.92   85.73
1.8516   1876.3 -45.35 51.855 2.62   636.5  7.52   439.08   515.0   1.04   64.77  -88.95  -88.96   78.18
IN THE FOLLOWING CALCULATION H= C.98821180E 01

1.8576   1800.9 -45.60 51.846 2.62   656.0  7.48   448.32   524.6   1.02   64.95  -88.97  -88.97   73.24
1.8635   1725.4 -45.85 51.837 2.62   676.2  7.40   459.63   532.2   1.01   65.13  -88.98  -88.99   67.52
1.8692   1650.7 -46.09 51.827 2.62   697.1  7.29   473.30   541.3   0.99   65.31  -88.99  -89.00   61.17
1.8746   1577.2 -46.34 51.818 2.62   718.3  7.14   489.62   551.6   0.98   65.49  -89.00  -89.01   54.41
1.8796   1505.6 -46.57 51.809 2.62   739.9  6.97   508.79   560.6   0.97   65.66  -89.01  -89.02   47.53
1.8843   1436.5 -46.80 51.801 2.61   761.4  6.78   530.76   567.4   0.96   65.82  -89.03  -89.03   40.86
1.8885   1370.9 -47.01 51.792 2.61   782.7  6.58   555.21   575.6   0.94   65.97  -89.04  -89.05   34.73
1.8922   1308.9 -47.22 51.785 2.61   803.4  6.38   581.87   584.4   0.93   66.11  -89.06  -89.06   29.27
1.8956   1250.3 -47.41 51.778 2.61   823.7  6.19   610.60   592.2   0.91   66.24  -89.08  -89.08   24.53
1.8986   1195.0 -47.60 51.771 2.61   843.4  6.01   641.00   600.6   0.89   66.36  -89.10  -89.10   20.51
1.9014   1143.0 -47.77 51.764 2.61   862.5  5.85   672.85   609.4   0.87   66.47  -89.12  -89.12   17.15
1.9039   1093.8 -47.93 51.759 2.61   881.1  5.71   705.95   615.9   0.84   66.57  -89.14  -89.15   14.35
1.9062   1047.6 -48.09 51.753 2.61   899.0  5.59   739.92   622.6   0.82   66.67  -89.16  -89.17   12.05
1.9082   1004.1 -48.23 51.748 2.61   916.3  5.48   774.58   629.3   0.80   66.76  -89.18  -89.19   10.16
1.9101    963.0 -48.37 51.743 2.61   933.0  5.40   809.82   634.7   0.78   66.84  -89.20  -89.21    8.61
1.9118    924.3 -48.50 51.739 2.61   949.1  5.34   845.39   640.6   0.76   66.91  -89.22  -89.23    7.34
1.9134    887.8 -48.62 51.735 2.61   964.7  5.29   881.26   646.1   0.74   66.99  -89.24  -89.25    6.28
1.9149    853.1 -48.74 51.731 2.61   979.7  5.26   917.33   651.7   0.72   67.05  -89.26  -89.27    5.41
1.9163    820.3 -48.85 51.728 2.61   994.3  5.24   953.56   657.5   0.70   67.12  -89.28  -89.29    4.68
1.9175    789.0 -48.95 51.725 2.61  1008.4  5.23   989.92   662.4   0.68   67.18  -89.30  -89.31    4.07
1.9187    759.3 -49.05 51.722 2.61  1022.0  5.23  1026.30   667.4   0.66   67.24  -89.31  -89.33    3.55
1.9198    730.9 -49.15 51.719 2.61  1035.2  5.24  1062.69   671.5   0.64   67.29  -89.33  -89.34    3.12
1.9209    703.9 -49.24 51.716 2.61  1048.1  5.26  1099.02   676.1   0.63   67.34  -89.34  -89.36    2.75
1.9219    678.1 -49.33 51.714 2.60  1060.5  5.28  1135.28   680.3   0.61   67.39  -89.36  -89.37    2.44
1.9228    653.4 -49.41 51.711 2.60  1072.6  5.31  1171.47   683.9   0.60   67.44  -89.37  -89.39    2.17
1.9237    629.7 -49.49 51.709 2.60  1084.3  5.35  1207.53   688.3   0.58   67.49  -89.38  -89.40    1.93
1.9245    607.0 -49.57 51.707 2.60  1095.7  5.38  1243.51   692.1   0.57   67.53  -89.40  -89.41    1.73
1.9253    585.2 -49.64 51.705 2.60  1106.8  5.42  1279.38   695.6   0.56   67.57  -89.41  -89.43    1.56
1.9261    564.2 -49.71 51.703 2.60  1117.7  5.47  1315.08   699.8   0.55   67.61  -89.42  -89.44    1.40
1.9268    544.0 -49.78 51.701 2.60  1128.2  5.51  1350.69   703.4   0.53   67.65  -89.43  -89.45    1.27
1.9275    524.6 -49.85 51.700 2.60  1138.5  5.56  1386.14   706.9   0.52   67.69  -89.44  -89.46    1.15
DOUBLE H  0.39528470E 02

IN THE FOLLOWING CALCULATION H= C.19764230E 02

1.9294    470.2 -50.04 51.695 2.60  1167.9  5.71  1491.59   716.4   0.49   67.80  -89.47  -89.49    0.88
 HEIGHT= 0.47C2422E 03   LAT=-C.5003580E 02   DELTA= 0.6779836E 02  PSI=-0.8946706E 02  PSIRES=-0.8948836E 02


            *** END OF PATH. ***

COMPILE TIME=     3.28 SEC,EXECUTION TIME=     8.88 SEC,OBJECT CODE=  21288 BYTES.ARRAY AREA=    1368 BYTES.UNUSED=   21344 BYTES
        $STOP

        $STOP
```

APPENDIX D.

The Haselgrove [1954] equations are reduced to the following equations in the case where the wave normal lies in the $r - \theta$ plane and there is no longitudinal gradient.

$$\frac{dr}{dt} = \frac{c}{\mu}\left(\frac{\rho_r}{\mu} - \frac{\partial\mu}{\partial\rho_r}\right), \tag{D.1}$$

$$\frac{d\theta}{dt} = \frac{c}{r\mu}\left(\frac{\rho_\theta}{\mu} - \frac{\partial\mu}{\partial\rho_\theta}\right), \tag{D.2}$$

$$\frac{d\rho_r}{dt} = \frac{c}{\mu}\frac{\partial\mu}{\partial r} + \rho_\theta\frac{d\theta}{dt} \quad \text{and} \tag{D.3}$$

$$\frac{d\rho_\theta}{dt} = \frac{1}{r}\left(\frac{c}{\mu}\frac{\partial\mu}{\partial\theta} - \rho_\theta\frac{dr}{dt}\right), \tag{D.4}$$

where

r and θ - polar coordinates of a point on the ray path,

μ - phase refractive index,

c - velocity of light in a vacuum,

t - phase time of the principal wave,

ρ_r and ρ_θ - polar projection of the vector $\vec{\rho} = \mu\,\vec{k}$,

$\vec{k}$ - unit vector perpendicular to the wave front.

Calling the angle of the wave normal with the vertical vector δ, the following expressions may be written:

$$\rho_r = \mu\cos\delta \tag{D.5}$$

and

$$\rho_\theta = \mu \sin \delta \tag{D.6}$$

In the Haselgrove equations the phase refractive index is a function of r, θ, ρ_r and ρ_θ, since it is supposed that the direction of the magnetic field is unknown. Therefore

$$\frac{\partial\mu}{\partial\rho_j} = \frac{\partial\mu}{\partial\psi}\frac{\partial\psi}{\partial\rho_j} = \frac{\partial\mu}{\partial\psi}\left(\frac{\rho_j \cos\psi - \mu Y_{oj}}{\mu^2 \sin\psi}\right) \qquad (j=r,\theta) \tag{D.7}$$

where Y_{oj} is the direction cosine of the magnetic field.

Calling the angle of the magnetic field with the radial vector γ, Y_{oj} is expressed as

$$Y_{or} = \cos \gamma \tag{D.8}$$

and

$$Y_{o\theta} = \sin \gamma \tag{D.9}$$

Therefore using the expressions above, Eq. (D.1) may be written in the following way:

$$\frac{dr}{dt} = \frac{c}{\mu \sin\psi}\left[\sin\psi \cos\delta - \frac{1}{\mu}\frac{\partial\mu}{\partial\psi}(\cos\delta \cos\psi - \cos\gamma)\right], \tag{D.10}$$

but

$$\tan \alpha = -\frac{1}{\mu}\frac{\partial\mu}{\partial\psi},$$

therefore

$$\frac{dr}{dt} = \frac{c}{\mu \sin\psi}\left[\cos\delta\,(\sin\psi + \tan\alpha \cos\psi) - \tan\alpha \cos\gamma\right] \tag{D.11}$$

or, using the relation (see Figure D-1),

$$\gamma = \delta - \psi \ ,$$

Eq. (D.11) may be written in the following way:

$$\frac{dr}{dt} = \frac{c}{\mu}\left[\cos\delta(\sin\psi + \tan\alpha\cos\psi) - \tan\alpha(\cos\delta\cos\psi + \sin\delta\sin\psi)\right], \qquad (D.12)$$

and, finally

$$\frac{dr}{dt} = \frac{c}{\mu\cos\alpha}\cos\beta \ , \qquad (D.13)$$

where β is the angle of the ray with the radial vector (see Figure D-1).

In the same way it is shown that Eq. (D.2) may be written as

$$\frac{d\theta}{dt} = \frac{c}{r\mu\cos\alpha}\sin\beta \ . \qquad (D.14)$$

It was, therefore, shown that Eq. (15a) and Eq. (15b) are equivalent to Eqs. (D.1) and (D.2).

Now it is necessary to show that the expressions for $d\delta/dt$ may be derived from Eqs. (D.1) to (D.4). The angle δ is given by

$$\delta = \tan^{-1}\left(\frac{\rho_\theta}{\rho_r}\right) \qquad (D.15)$$

Therefore

$$\frac{d\delta}{dt} = \frac{1}{\mu}\left(\cos\delta\frac{d\rho_\theta}{dt} - \sin\delta\frac{d\rho_r}{dt}\right) \qquad (D.16)$$

Substituting Eqs. (D.3) and (D.4) into Eq. (D.16) and after some algebraic

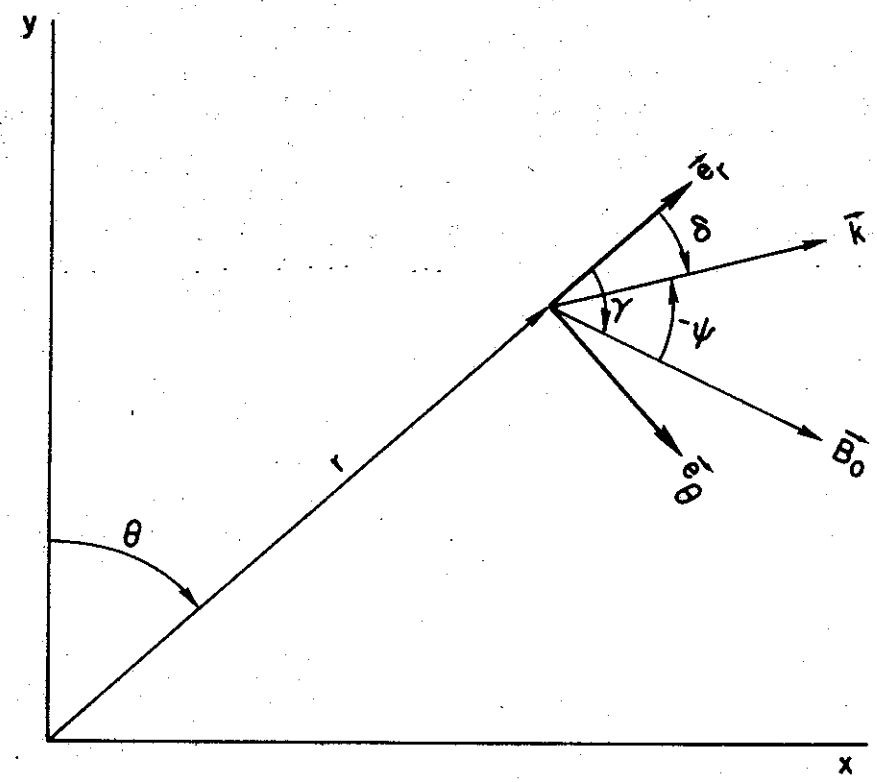

Figure D-1. At a given point on the ray path in polar coordinates, $r - \theta$, the wave normal $\vec{k}$ and the static magnetic field $\vec{B}_o$ are shown. The angles are positive in the clockwise direction.

operations the following expression is obtained

$$\frac{d\delta}{dt} = \frac{c}{\mu^2}\left(\frac{\cos\delta}{r}\frac{\partial\mu}{\partial\theta} - \sin\delta\frac{\partial\mu}{\partial r} - \sin\delta\frac{\cos\delta}{r}\frac{dr}{dt} + \sin\delta\frac{d\theta}{dt}\right) \tag{D.17}$$

Using expressions (D.13) and (D.14) and after some algebraic work Eq. (D.17) reduces to

$$\frac{d\delta}{dt} = \frac{c}{\mu^2}\left(\frac{\cos\delta}{r}\frac{\partial\mu}{\partial\theta} - \sin\delta\frac{\partial\mu}{\partial r}\right) - \frac{c}{\mu r}\sin\delta \tag{D.18}$$

Therefore Eqs. (D.1) to (D.4) are reduced to Eqs. (15a-b), and Eq. (23).

APPENDIX E.

To understand the behavior of the ray path it is helpful to have the differential equation that governs the variation of the angle (ψ) between the wave normal and the geomagnetic field, with phase time. From Eq. (11) and the relation (see Figure E-1)

$$\phi = \gamma + \psi \tag{E.1}$$

the following equation is derived

$$\frac{d\psi}{dt} = \frac{c}{\mu^2}\left[\frac{\partial\mu}{\partial x}\cos\phi - \frac{\partial\mu}{\partial y}\sin\phi\right] - \frac{d\gamma}{dt}, \tag{E.2}$$

where γ is given by

$$\frac{d\gamma}{dt} = \frac{\partial\gamma}{\partial x}\frac{dx}{dt} + \frac{\partial\gamma}{\partial y}\frac{dy}{dt} \tag{E.3}$$

for the case of a static magnetic field.

Combining Eqs. (E.3) and (13a-b) the following result is obtained

$$\frac{d\gamma}{dt} = \frac{c}{\mu\cos\alpha}\left[\sin(\alpha+\phi)\frac{\partial\gamma}{\partial x} + \cos(\alpha+\phi)\frac{\partial\gamma}{\partial y}\right] \tag{E.4}$$

Now using the relation

$$\tan\alpha = -\frac{1}{\mu}\frac{\partial\mu}{\partial\psi} \tag{E.5}$$

in Eq. (E.4) the following equation may be written

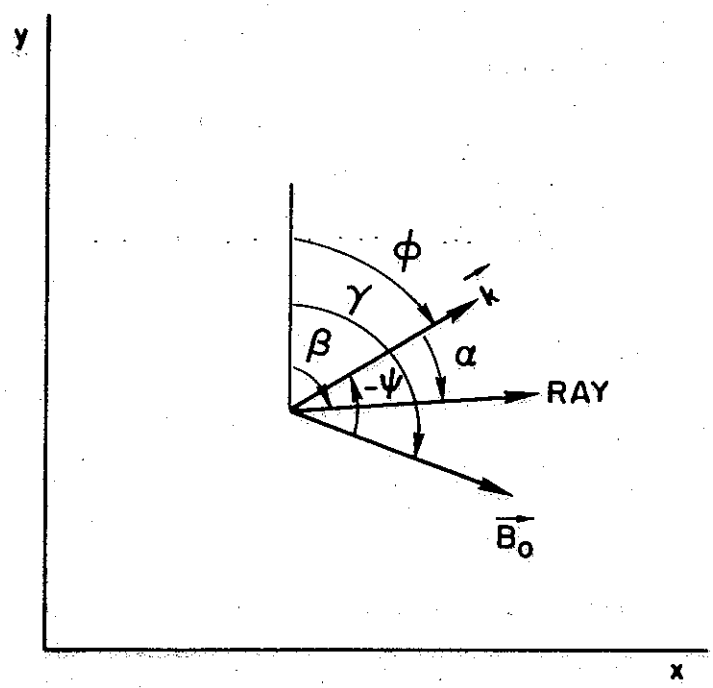

Figure E-1. In a cartesian system of coordinates, x-y, the angles between the wave normal $\vec{k}$, the direction of the energy, RAY, and the static magnetic field $\vec{B}_o$ with the vertical are indicated. Also shown are the angles between these vectors. The angles are positive in the clockwise direction.

$$\frac{d\gamma}{dt} = \frac{c}{\mu^2}\frac{\partial\mu}{\partial\psi}\left[\frac{\partial\gamma}{\partial y}\sin\phi - \frac{\partial\gamma}{\partial x}\cos\phi\right] + \frac{c}{\mu}\left[\frac{\partial\gamma}{\partial x}\sin\phi + \frac{\partial\gamma}{\partial y}\cos\phi\right] \tag{E.6}$$

The phase refractive index is a function of X, Y and ψ, which are functions of x and y, and therefore

$$\frac{\partial\mu}{\partial x} = \sum_i \frac{\partial\mu}{\partial X_i}\frac{\partial X_i}{\partial x} + \sum_i \frac{\partial\mu}{\partial Y_i}\frac{\partial Y_i}{\partial x} + \frac{\partial\mu}{\partial\psi}\frac{\partial\psi}{\partial x} \tag{E.7}$$

and

$$\frac{\partial\mu}{\partial y} = \sum_i \frac{\partial\mu}{\partial X_i}\frac{\partial X_i}{\partial y} + \sum_i \frac{\partial\mu}{\partial Y_i}\frac{\partial Y_i}{\partial y} + \frac{\partial\mu}{\partial\psi}\frac{\partial\psi}{\partial y} \tag{E.8}$$

but

$$\gamma = \phi - \psi \tag{E.9}$$

resulting in

$$\frac{\partial\gamma}{\partial x} = -\frac{\partial\psi}{\partial x} \tag{E.10}$$

and

$$\frac{\partial\gamma}{\partial y} = -\frac{\partial\psi}{\partial y} \tag{E.11}$$

Combining Eqs. (E.2), (E.6), (E.7) and (E.8) results in

$$\frac{d\psi}{dt} = \frac{c}{\mu^2}\left[\sum_i \frac{\partial\mu}{\partial X_i}\frac{\partial X_i}{\partial x}\cos\phi - \sum_i \frac{\partial\mu}{\partial X_i}\frac{\partial X_i}{\partial y}\sin\phi + \right. \tag{E.12}$$

$$\left. + \sum_i \frac{\partial\mu}{\partial Y_i}\frac{\partial Y_i}{\partial x}\cos\phi - \sum_i \frac{\partial\mu}{\partial Y_i}\frac{\partial Y_i}{\partial y}\sin\phi\right] - \frac{c}{\mu}\left[\sin\phi\,\frac{\partial\gamma}{\partial x} + \cos\phi\,\frac{\partial\gamma}{\partial y}\right]$$

Now defining

$$\vec{k} = \sin\phi\;\vec{e}_x + \cos\phi\;\vec{e}_y \tag{E.13}$$

and

$$\vec{k}_{\perp} = \cos\phi \ \vec{e}_x - \sin\phi \ \vec{e}_y \tag{E.14}$$

Equation (E.12) may be written as

$$\frac{d\psi}{dt} = \frac{c}{\mu} \left[\sum_i \frac{\partial \log\mu}{\partial X_i} \nabla X_i \cdot \vec{k}_{\perp} + \sum_i \frac{\partial \log\mu}{\partial Y_i} \nabla Y_i \cdot \vec{k} \right] - \frac{c}{\mu} \nabla\gamma \cdot \vec{k} \tag{E.15}$$

Now two hypotheses are made about the medium, first that the magnetosphere is constituted of electrons only (which is a good hypothesis for wave frequencies above the LHR frequency) and second that the earth's magnetic field is represented by a centered dipole. For this case the following expression may be written for the gradient of the direction of the magnetic field:

$$\nabla\gamma = \frac{3}{r} \frac{\cos^2\theta + 1}{3\cos^2\theta + 1} \vec{e}_{\theta} \tag{E.16}$$

The phase refractive index, applying the quasi-longitudinal (Q.L.) approximation (see Helliwell [1965]), is

$$\mu^2 = \frac{X}{Y\cos\psi - 1} \tag{E.17}$$

which is a good approximation for the case in study. Therefore

$$\frac{\partial \log\mu}{\partial Y} = -\frac{1}{2} \frac{\cos\psi}{Y\cos\psi - 1} \tag{E.18}$$

and

$$\frac{\partial \log\mu}{\partial X} = \frac{1}{2X} \tag{E.19}$$

For the electron density distribution a diffusive equilibrium model is assumed and therefore the following expression may be written for the electron density:

$$n_{De} = n_{eb}\, e^{-z/2H} \tag{E.20}$$

From which results

$$\nabla X = -\frac{X}{2H}\frac{\partial z}{\partial r}\vec{e}_r \tag{E.21}$$

where

$$z = r_b\left(1 - \frac{r_b}{r}\right) \tag{E.22}$$

and

$$\frac{\partial z}{\partial r} = \left(\frac{r_b}{r}\right)^2 \tag{E.23}$$

Since a dipole has been considered, the gradient of Y is given by

$$\nabla Y = -\frac{3}{r}\, Y\, \vec{e}_r + \frac{3}{2r}\, Y\, \frac{\cos\theta\, \sin\theta}{3\cos^2\theta + 1}\, \vec{e}_\theta \tag{E.24}$$

Combining Eqs. (E.15) to (E.24) results in

$$\frac{d\psi}{dt} = \frac{c}{\mu r}\left\{\frac{r_b^2}{4Hr}\sin\delta - \frac{3}{2}\,\frac{Y\cos\psi}{Y\cos\psi - 1}\left(\sin\delta - \frac{\sin\theta\cos\theta}{3\cos^2\theta + 1}\cos\delta\right) - \right. \tag{E.25}$$

$$\left. - 3\,\frac{\cos^2\theta + 1}{3\cos^2\theta + 1}\sin\delta\right\}$$

or

$$\frac{d\psi}{dt} = \frac{c}{\mu r}\left\{f_1\sin\delta - \frac{3}{2}\,\frac{Y\cos\psi}{Y\cos\psi - 1}\,(f_2\sin\delta - f_3\cos\delta) - f_4\sin\delta\right\} \tag{E.26}$$

where f_1 is the term due to the vertical gradient of the electron density; f_2 is the radial component of the gradient of the magnetic field; f_3 is the θ component of the gradient of the magnetic field, and f_4 is the term corresponding to the variation of the magnetic field direction. The terms f_1, f_3 and f_4 are plotted in Figures E-2, E-3 and E-4, respectively.

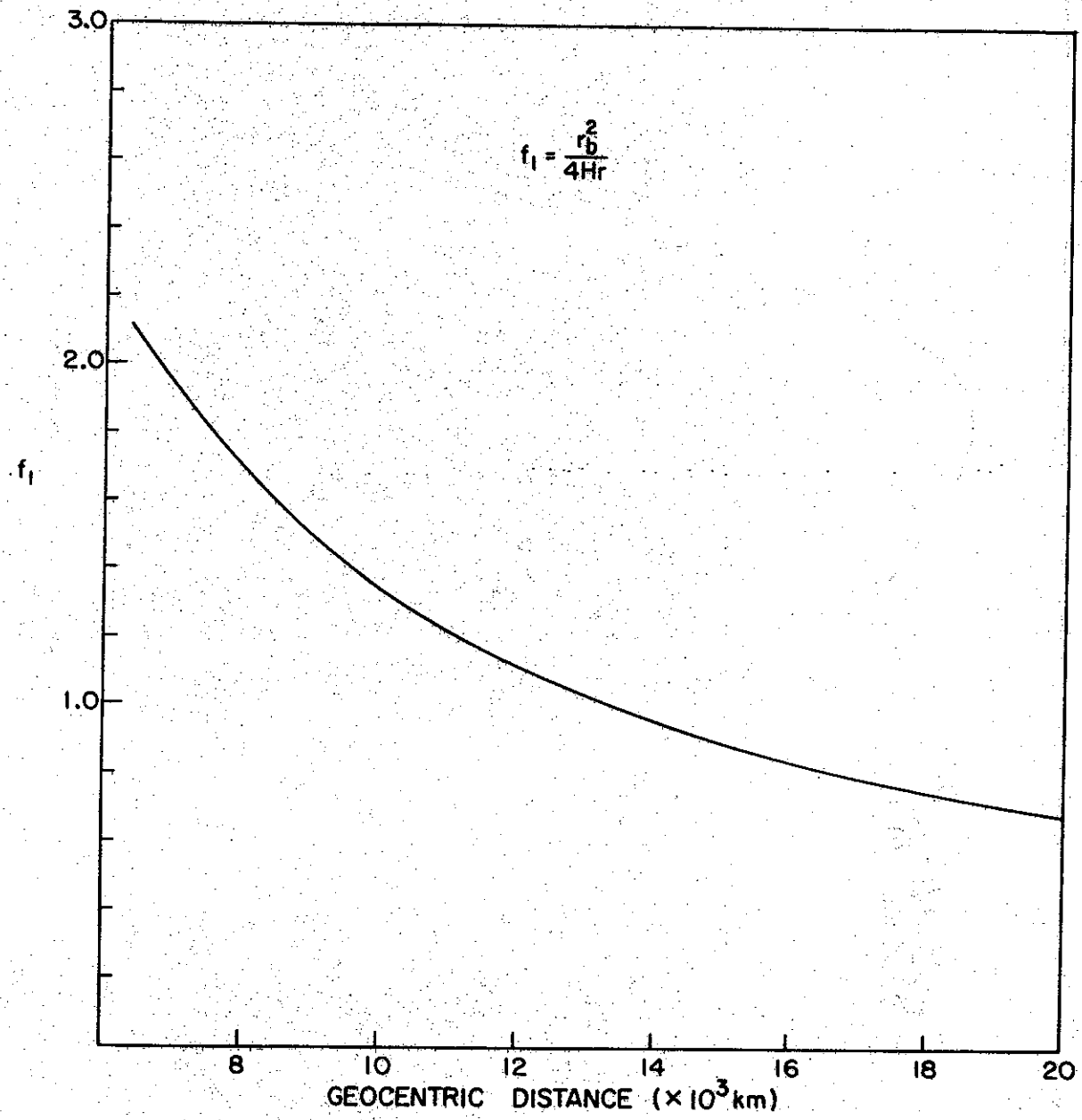

Figure E-2. Plot of function f_1 versus geocentric distance. In this case the height 1000 km and a scale equal to 1000 km were taken for the base level.

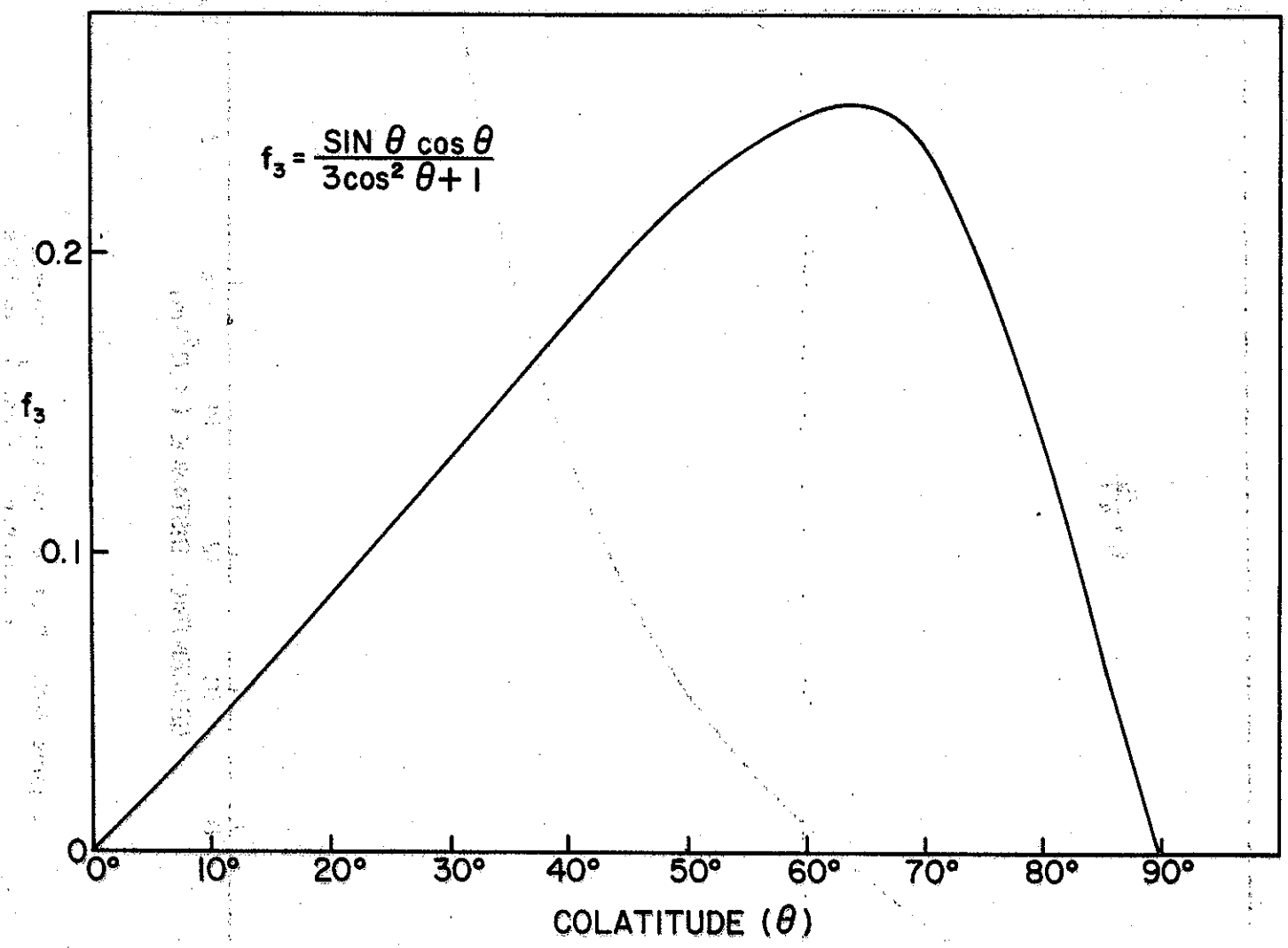

Figure E-3. Plot of the function f_3 versus colatitude.

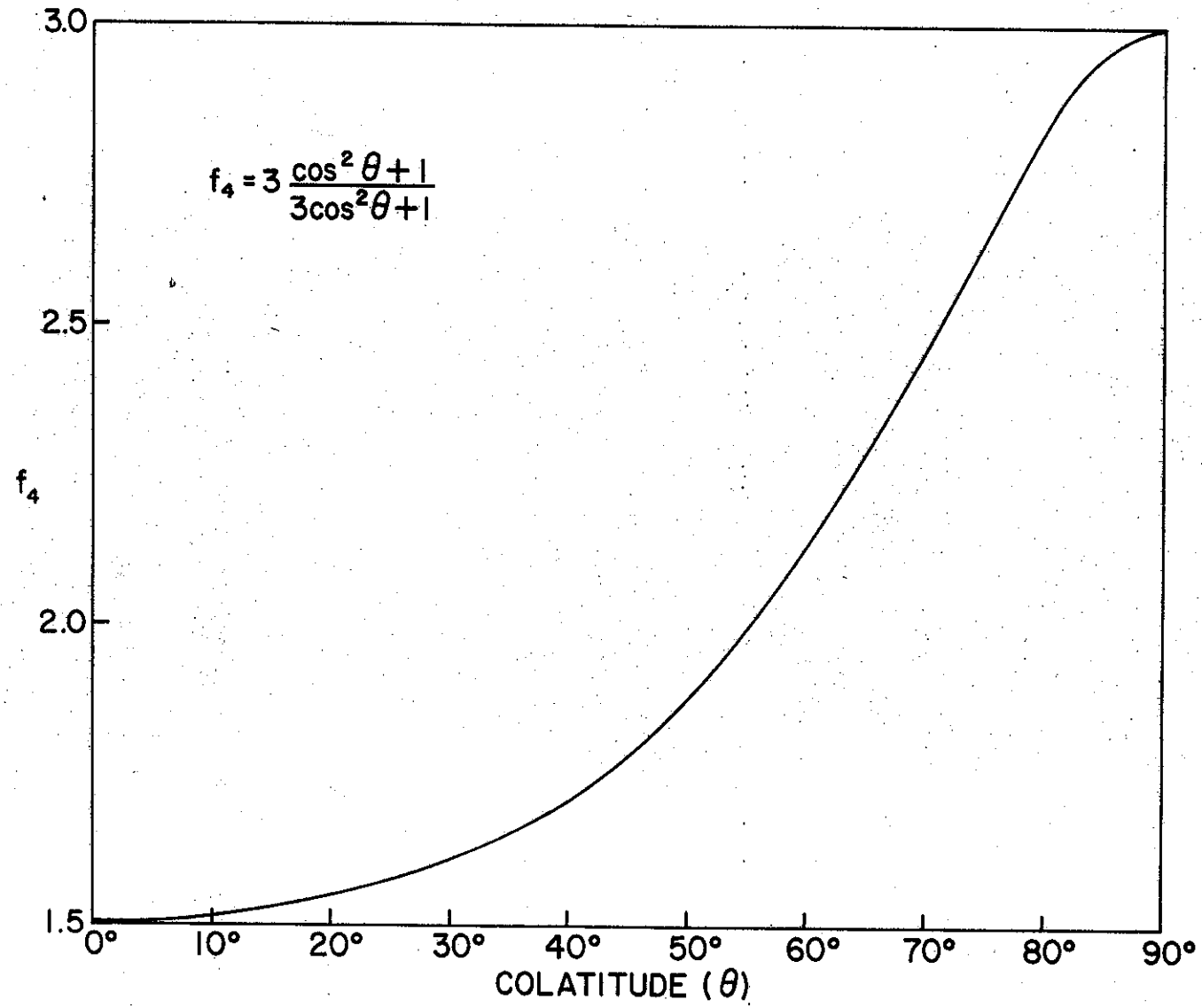

Figure E-4. Plot of the function f_4 versus colatitude.

APPENDIX F.

The objective of this appendix is to show the general form of the differential Snell's law.

A vector $\vec{\rho}$ is defined as

$$\vec{\rho} = \mu \vec{k} \tag{F.1}$$

where μ is the phase refractive index and $\vec{k}$ a unit vector perpendicular to the wave front.

The cartesian components of $\vec{\rho}$ (see Figure F-1) are

$$\rho_x = \mu \sin\phi \tag{F.2}$$

and

$$\rho_y = \mu \cos\phi \tag{F.3}$$

The total time derivatives of ρ_x and ρ_y are

$$\frac{d\rho_x}{dt} = \sin\phi \frac{d\mu}{dt} + \mu \cos\phi \frac{d\phi}{dt} \tag{F.4}$$

and

$$\frac{d\rho_y}{dt} = \cos\phi \frac{d\mu}{dt} - \mu \sin\phi \frac{d\phi}{dt} , \tag{F.5}$$

where, for the case of a stationary medium

$$\left(\frac{\partial\mu}{\partial t} = 0\right)$$

$$\frac{d\mu}{dt} = \frac{\partial\mu}{\partial x}\frac{dx}{dt} + \frac{\partial\mu}{\partial y}\frac{dy}{dt} + \frac{\partial\mu}{\partial\phi}\frac{d\phi}{dt} \tag{F.6}$$

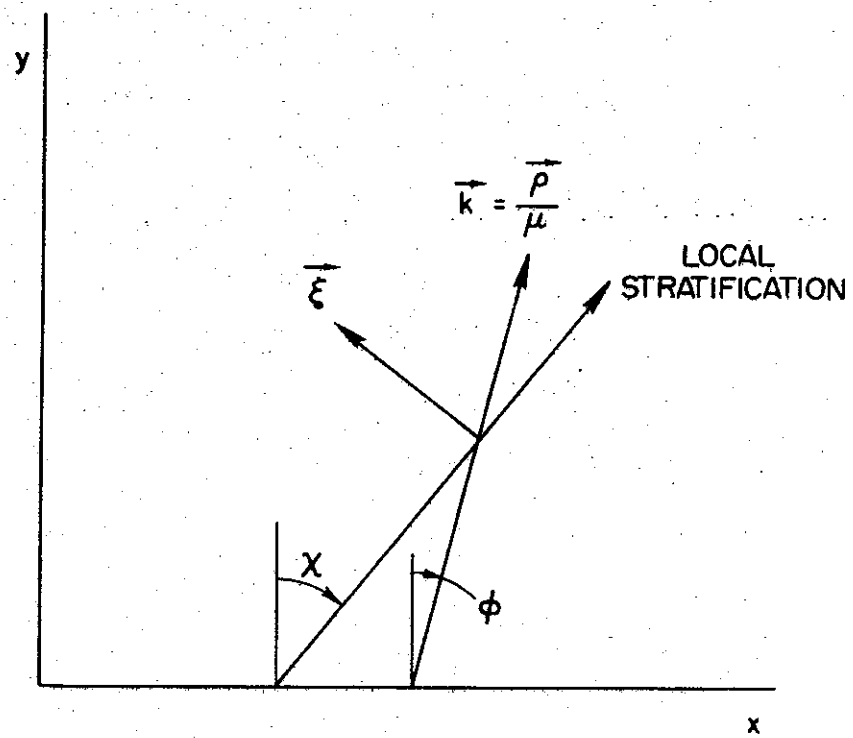

Figure F-1. At a given point in a cartesian system of coordinates, x and y, the direction of the local stratification (χ), the unit vector $\vec{k}$ and the unit vector $\vec{\xi}$ perpendicular to the local stratification are shown.

Combining Eqs. (F.4), (F.5), (F.6) and (13a) results in

$$\frac{d\rho_x}{dt} = \frac{c}{\mu} \frac{\partial\mu}{\partial x}\bigg|_{y,\phi} \tag{F.7}$$

and

$$\frac{d\rho_y}{dt} = \frac{c}{\mu} \frac{\partial\mu}{\partial y}\bigg|_{x,\phi} \tag{F.8}$$

Since

$$\vec{\rho} = \rho_x \vec{e}_x + \rho_y \vec{e}_y \tag{F.9}$$

Equations (F.7) and (F.8) may be written in the following way

$$\frac{d\vec{\rho}}{dt} = \frac{c}{\mu} \tilde{\nabla} \mu \tag{F.10}$$

where $\tilde{\nabla}$ is an operator defined as

$$\tilde{\nabla} \mu = \frac{\partial\mu}{\partial x}\bigg|_{y,\phi} \vec{e}_x + \frac{\partial\mu}{\partial y}\bigg|_{x,\phi} \vec{e}_y \tag{F.11}$$

This operator is not the gradient operator (∇), because μ is not only a function of position, x and y, but also of direction. For an isotropic medium μ is only a function of position and therefore for this case

$$\tilde{\nabla} \mu \equiv \nabla \mu$$

The $\tilde{\nabla} \mu$ is always calculated keeping the direction of the vector $\vec{\rho}$ constant. As an example the expression for $\tilde{\nabla} \mu$ is now found in polar coordinates.

The two dimensional Haselgrove [1954] equations in polar coordinates are

$$\frac{dr}{dt} = \frac{c}{\mu}\left(\rho_r - \mu\frac{\partial\mu}{\partial\rho_r}\right) \tag{F.12}$$

$$\frac{d\theta}{dt} = \frac{c}{\mu r}\left(\rho_\theta - \mu\frac{\partial\mu}{\partial\rho_\theta}\right) \tag{F.13}$$

$$\frac{d\rho_r}{dt} = \frac{c}{\mu}\frac{\partial\mu}{\partial r} + \rho_\theta\frac{d\theta}{dt} \tag{F.14}$$

$$\frac{d\rho_\theta}{dt} = \frac{c}{\mu r}\frac{\partial\mu}{\partial\theta} - \frac{\rho_\theta}{r}\frac{dr}{dt} \tag{F.15}$$

Starting from Eq. (F.10) the Eqs. (F.14) and (F.15) are derived.

In polar coordinates the vector $\vec{\rho}$ is given by

$$\vec{\rho} = \rho_r\,\vec{e}_r + \rho_\theta\,\vec{e}_\theta \tag{F.16}$$

resulting in

$$\frac{d\vec{\rho}}{dt} = \left(\frac{d\rho_r}{dt} - \rho_\theta\frac{d\theta}{dt}\right)\vec{e}_r + \left(\frac{d\rho_\theta}{dt} + \rho_r\frac{d\theta}{dt}\right)\vec{e}_\theta \tag{F.17}$$

Now writing μ as a function of r, θ and δ (see Figure F-2), the action of the operator $\tilde{\nabla}$ upon μ results in

$$\tilde{\nabla}\mu = \left.\frac{\partial\mu}{\partial r}\right|_{\theta,\delta}\vec{e}_r + \frac{1}{r}\left(\left.\frac{\partial\mu}{\partial\theta}\right|_{r,\delta} - \left.\frac{\partial\mu}{\partial\delta}\right|_{r,\theta}\right)\vec{e}_\theta \tag{F.18}$$

From Figure F-2

$$\gamma = \delta - \psi$$

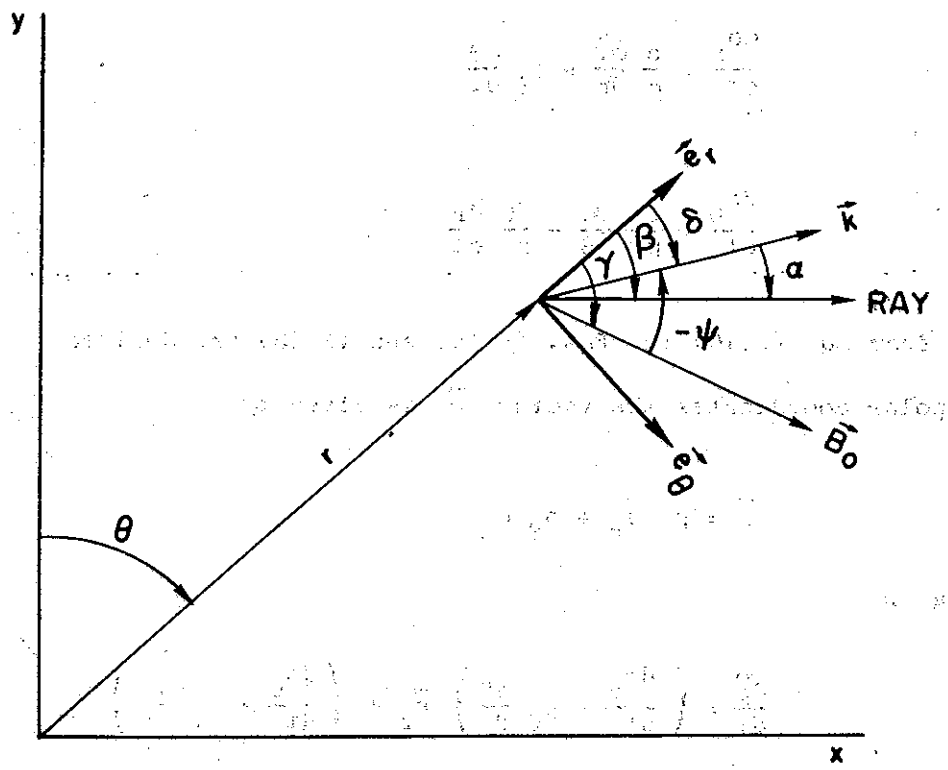

Figure F-2. At a given point in a polar system of coordinates, r and θ, the phase refractive index vector, $\vec{\rho}$, and the static magnetic field $\vec{B}_o$ are shown.

and therefore

$$\left.\frac{\partial\mu}{\partial\delta}\right|_{r,\theta} = \frac{\partial\mu}{\partial\psi} \tag{F.19}$$

Combining Eqs. (F.10), (F.17) and (F.18) the results are

$$\frac{d\rho_r}{dt} = \frac{c}{\mu}\frac{\partial\mu}{\partial r} + \rho_\theta \frac{d\theta}{dt} \tag{F.20}$$

and

$$\frac{d\rho_\theta}{dt} = \frac{c}{\mu r}\left(\frac{\partial\mu}{\partial\theta} - \frac{\partial\mu}{\partial\psi}\right) - \rho_r \frac{d\theta}{dt} \tag{F.21}$$

It is necessary to show that Eqs. (F.20) and (F.14) are equivalent, or to show that

$$\frac{c}{\mu r}\frac{\partial\mu}{\partial\psi} + \rho_r \frac{d\theta}{dt} = \frac{\rho_\theta}{r}\frac{dr}{dt} \tag{F.22}$$

From Eq. (15b)

$$\frac{d\theta}{dt} = \frac{c}{\mu r \cos\alpha}\cos\beta \tag{F.23}$$

and the relation

$$\tan\alpha = -\frac{1}{\mu}\frac{\partial\mu}{\partial\psi}, \tag{F.24}$$

the left-hand member of Eq. (F.22) may be written as

$$\frac{c}{\mu r}\frac{\partial\mu}{\partial\psi} + \rho_r \frac{d\theta}{dt} = \frac{c}{r\cos\alpha}\sin\delta\,\sin\beta \tag{F.25}$$

Using

$$\rho_\theta = \mu \sin\delta \tag{F.26}$$

and (see Eq. (15a))

$$\frac{dr}{dt} = \frac{c}{\mu \cos\alpha} \sin\beta \tag{F.27}$$

results in

$$\frac{\rho_\theta}{r} \frac{dr}{dt} = \frac{c}{r\mu \cos\alpha} \sin\delta \sin\beta \tag{F.28}$$

which shows that Eqs. (F.15) and (F.21) are equivalent.

Now defining a vector $\vec{\xi}$ such that

$$\vec{\xi} = \frac{\tilde{\nabla}\mu}{|\tilde{\nabla}\mu|} \tag{F.29}$$

and taking its vector product with Eq. (F.10) the following equation is obtained

$$\vec{\xi} \times \frac{d\vec{\rho}}{dt} = 0 \tag{F.30}$$

or

$$\frac{d(\vec{\xi} \times \vec{\rho})}{dt} - \frac{d\vec{\xi}}{dt} \times \vec{\rho} = 0 \tag{F.31}$$

Equation (F.30) or (F.31) are the differential Snell's law for any medium.

In the next paragraph the differential Snell's law for a two dimensional geometry is derived from Eq. (F.31). The <u>local stratificiation</u> is defined as being the vector $\vec{\xi}_\perp$ such that

$$\vec{\xi}_\perp \cdot \vec{\xi} = 0 \tag{F.32}$$

or

$$\vec{\xi}_{\perp} \cdot \tilde{\nabla}\mu = 0 \tag{F.33}$$

The local stratification for a given direction of $\vec{\rho}$ is found by looking for the locus of points that have the same phase refractive index holding the direction of the vector $\vec{\rho}$ constant.

For the case of Figure F-1, the stratification is given by

$$\left.\frac{\partial\mu}{\partial x}\right|_{y,\phi} \cos\chi + \left.\frac{\partial\mu}{\partial y}\right|_{x,\phi} \sin\chi = 0 \tag{F.34}$$

where χ is the direction of the local stratification. The vector $\vec{\xi}$ is given by

$$\vec{\xi} = -\sin\chi\, \vec{e}_x + \cos\chi\, \vec{e}_y \,, \tag{F.35}$$

resulting in

$$\vec{\xi} \times \vec{\rho} = -\mu \cos(\phi-\chi)\, \vec{e}_z \,, \tag{F.36}$$

and

$$\frac{d\vec{\xi}}{dt} \times \vec{\rho} = -\mu \sin(\phi-\chi) \frac{d\chi}{dt} \vec{e}_z \tag{F.37}$$

The combination of Eqs. (F.31), (F.36) and (F.37) results in

$$\frac{d[\mu \cos(\phi-\chi)]}{dt} - \mu \sin(\phi-\chi) \frac{d\chi}{dt} = 0 \tag{F.38}$$

or

$$\cos(\phi-\chi) \frac{d\mu}{dt} - \mu \sin(\phi-\chi) \frac{d\phi}{dt} = 0 \tag{F.39}$$

Equation (F.39) represents the differential Snell's law for the geometry shown in Figure F-1.

In the case where a parallel stratification is supposed, χ is constant, and also $\vec{\xi}$, which results in Eq. (F.31) being simplified to

$$\frac{d(\vec{\xi}\times\vec{\rho})}{dt} = 0 \tag{F.40}$$

or using Eq. (F.36)

$$\frac{d[\mu \cos(\phi-\chi)]}{dt} = 0 \tag{F.41}$$

This is the form of the differential Snell's law valid only for parallel stratification, that is, when

$$\frac{d\chi}{dt} = 0 \tag{F.42}$$

Equation (F.41) is the starting point for the development given in paragraph 3 of the Haselgrove paper [1954]. Therefore indirectly a medium was supposed with a parallel stratification in that paragraph. However what is <u>very interesting</u> is that starting from Eq. (F.41), which is only valid for parallel stratification, Eq. (F.39) is obtained, as is shown below.

For parallel stratification

$$\frac{d[\mu \cos(\phi-\chi)]}{dt} = 0 \tag{F.43}$$

and

$$\frac{d\chi}{dt} = 0 \tag{F.44}$$

The combination of Eq. (F.43) and Eq. (F.44) results in

$$\cos(\phi-\chi)\,\frac{d\mu}{dt} - \mu\,\sin(\phi-\chi)\,\frac{d\phi}{dt} = 0 \qquad \text{(F.45)}$$

which is the same as Eq. (F.39).

REFERENCES

Angerami, J. J. and J. O. Thomas, Studies of planetary atmospheres, 1, the distribution of electrons and ions in the earth's ionosphere, J. Geophys. Res., 69, 4537, 1964.

Barrington, R. E. and J. S. Belrose, Preliminary results from Canada's Alouette satellite, Nature, 198, 651, 1963.

Brace, L. H., B. M. Reddy, and H. G. Mayr, Global behavior of the ionosphere at 1000-kilometer altitude, J. Geophys. Res., 72, 265, 1967.

Brice, N. M. and R. L. Smith, Lower hybrid resonance emissions, J. Geophys. Res., 70, 71, 1965.

Budden, K. G., Radio Waves in the Ionosphere, Cambridge University Press, Cambridge, England, 1961.

Cain, J. C., S. Hendricks, W. E. Daniels, and D. C. Jensen, Computation of the main geomagnetic field from spherical harmonic expansion, NASA/GSFC Note NSSDC 68-11, Greenbelt, Maryland, May 1968.

Carpenter, D. L., K. Stone and S. Lasch, A case of artificial triggering of VLF magnetospheric noise during the drift of a whistler duct across magnetic shells, J. Geophys. Res., 74, 1848, 1969.

Gurnett, D. A., S. D. Shawhan, N. Brice and R. L. Smith, Ion cyclotron whistlers, J. Geophys. Res., 70, 1665, 1965.

Haselgrove, J., Ray theory and a new method for ray tracing, Rept. of Physical Society Conference on Physics of the Ionosphere, 355, Cambridge University, Cambridge, England, 1954.

Haselgrove, J., Oblique ray paths in the ionosphere, Proc. of Phys. Soc., 70B, 653, 1957.

Helliwell, R. A., Whistlers and Related Ionospheric Phenomena, Stanford University Press, Stanford, California, 1965.

Hildebrand, F. B., Introduction to Numerical Analysis, (Chapter 6), McGraw-Hill Book Co., New York, 1956.

Hines, C. O., Heavy-ion effects in audio-frequency radio propagation, J. Atmos. & Terr. Phys., 11, 36, 1957.

Hines, C. O., W. C. Hoffman and H. Weil, Transverse whistler propagation, University of Michigan Radio Propagation Lab., University of Mich., Ann Arbor, Michigan, 1959.

Kimura, I., Effects of ions on whistler-mode ray tracing, Radio Science, 1, 269, 1966.

Library Program No. 11(7090), Computation Center Facility, Stanford University, Stanford, California, July, 1965.

Maeda, K., and I. Kimura, A theoretical investigation on the propagation path of whistler atmospherics, Rept. Ion. Res., Japan, 10, 105, 1956.

Muzzio, J. L. R., Ion cutoff whistlers, J. Geophys. Res., 73, 7526, 1968.

Scarabucci, R. R., J. J. Angerami, and R. A. Helliwell, OGO-4 amplitude measurements of VLF signals--the pro-longitudinal whistler mode of propagation, (in preparation), 1969.

Shawhan, S. D., VLF ray tracing in a model ionosphere, Dept. of Physics and Astronomy, University of Iowa, Iowa City, Iowa, 1966.

Smith, R. L., The use of nose whistlers in the study of the outer ionosphere, Tech. Rept. No. 6, Radioscience Lab., Stanford Electronics Labs., Stanford University, Stanford, California, July, 1960.

Smith, R. L. and J. J. Angerami, Magnetospheric properties deducedfrom OGO-1 observations of ducted and nonducted whistlers, J. Geophys. Res., 73, 1, 1968.

Smith, R. L., I. Kimura, J. Vigneron, and J. Katsufrakis, Lower hybrid resonance noise and a new ionospheric duct, J. Geophys. Res., 71, 1925, 1966.

Stix, T. H., The Theory of Plasma Waves, McGraw Hill Book Co., New York, 1962.

Storey, L. R. O. and J. C. Cerisier, Une interpretation des bandes de bruit au voisinage de la frequence hybride basse observees au moyen de satellites artificiels, C.R. Acad. Sc. Paris, 266, 525, 1968.

Thorne, R. M., Unducted whistler evidence for a secondary peak in the electron energy spectrum near 10 kev, J. Geophys. Res., 76, 4895, 1968.

Walter, F., A three-dimensional ray-tracing computer program, (in prep.) 1969.

Yabroff, I. W., Computation of whistler ray paths, J. Res. NBS, 65D, 485, 1961.